

ABSTRACT

Title of Thesis: A COMPUTATIONAL STUDY OF THE CLAP AND FLING AERODYNAMIC MECHANISM

Grigorios Panagakos
Master of Science, 2009

Directed By: Professor Elias Balaras
Department of Bioengineering

Clap and fling is a particular wing kinematic pattern utilized by some insects and birds to produce enhanced aerodynamic forces. It consists of two very distinct phases: i) the leading edges of the two wings are brought together near the upper limit of the upstroke and subsequently the wings are rotated around their leading edges, "clapping" like a closing book; ii) at the onset of the downstroke, and while they are still close, the two wings rotate around their trailing edges "flinging" apart. Prior theoretical and experimental work suggested that clap-and-fling is responsible for production of unusually high lift coefficients. However, due to limitations of the theoretical models and experimental techniques, detailed quantitative results are yet to be reported. The primary objective of the present work is to provide a concrete description of the underlying physics by means of high-fidelity simulations based on the Navier-Stokes equations for incompressible flow. In particular, the effects of the kinematics and the Reynolds number are discussed in detail in the thesis. Thesis'

results verify the lift enhancement trends observed in experiments and identify the particular flow patterns correlated with such increases.

A COMPUTATIONAL STUDY OF
THE CLAP AND FLING AERODYNAMIC MECHANISM

By

Grigorios Panagakos

Thesis submitted to the Faculty of the Graduate School of the
University of Maryland, College Park, in partial fulfillment
of the requirements for the degree of
Master of Science
2009

Advisory Committee:
Professor Elias Balaras, Chair
Professor Balakumar Balachandran
Professor Kenneth Kiger

© Copyright by
Grigorios Panagakos
2009

Dedication

to my professors, Mr. Nikolaos Pangalos for his impeccable and modest character which set my lifetime model for a scientist-human, and Mrs Eleonora Kontogianni, for revealing the true inner potential of a whole generation, of which I was blessed to be part of.

To my sister Evangelia, my oasis in this world.

Acknowledgements

In the beginning, I would like to express my sincere gratitude to professor Elias Balaras for making possible for me to realize my dream and conduct research in a University of as high reputation and standards as University of Maryland and made me part of his research team whose work is known for its originality and state of the art standing. He gave me the opportunity to set a new course in my life. Without his help, patience and support my stay would not be feasible. His guidance and the trust he has shown in me were invaluable parts of our academic cooperation.

I would like to thank also the members of my committee Professor Balakumar Balachnadran and Professor Kenneth Kiger together, in the first place for reading my thesis and providing their feedback.

More specifically, I would like to thank Professor Balakumar Balachnadran whose course on Dynamics was very helpful for the main part of the thesis. I would also like to thank in his name the Department of Mechanical Engineering for its acceptance and support, and for creating an inspiring and motivating academic environment which helped me advance and set high goals. It was really an honor but also a pleasure working among and with the faculty members, the staff and students of the Department.

Many thanks to Professor Kenneth Kiger, who besides being my instructor on 'Viscous Flow', a course proved to be very interesting and helpful for the analysis of the thesis' results he also provided many advices about my future steps and his understanding throughout my last semester.

I would also like to thank all faculty members whose graduate courses I took through my master's but I have to highlight some of them whose unconditional and touching support will always have a special place in my heart, as they manage to combine their undisputed scientific achievements with honest and vivid care about their students. Namely, Professor Emeritus John Jr. Anderson of the Aerospace Engineering department, professor Ricardo Nochetto of the Applied Mathematics department and Professor James Duncan of the Mechanical Engineering department for helping me either getting in touch with scientific personnel in Europe in order to increase my options and make the best choice regarding the continuation of my academic adventure or providing me with reference letters. In the same context, only without having the luck to attend one of his courses I would like to thank Professor James Wallace.

An important factor of every professional accomplishment, especially in the research disciplines, is the level of cooperation that can be developed between the members of the team working together. My colleagues, with their team spirit and moral and technical support made sure that this cooperation would have a positive outcome. More specifically, I would like to address many special thanks to PhD candidate Marcos Vanella whose invaluable assistance extended in many levels while he was walking me through the scientific activity of our group and constantly standing by my side through all the hardships as I was gradually integrating and was becoming more and more independent. He also introduced me into some of his prior research work which also served as a starting point for the methodology of my thesis.

In this point I want to thank my other team colleague, Ph.D student Khaled Abdelaziz, for his excellent collaboration these two years having many useful discussions while taking together the majority of our graduate courses and for his artistic contribution to the thesis.

I could not also neglect paying tribute to the professors whose teaching assistant I used to be the past four semesters i.e. Professor James Duncan, Lecturer Chandrasekhar Thamire, Professor Kenneth Kiger and Professor Elias Balaras, as well as the students I had the opportunity to teach. I hope that I was able to give back something, through this activity, in return to what this school has given to me.

I owe my deepest appreciation and many warm thanks to Mr. Spyros Soulis and his wonderful family as well as to Mrs Aikaterini Sideri for being spiritually by my side and urge me with true love and care to always aim high and to seek my path in life through faith, creativity and immediate contribution to human society.

Finally, I would like to express my gratitude to my family giving me over the years the values that define me as person and the courage to fight for them. Their belief in me and their moral support helped me to alleviate many of the difficulties I faced these last two years and to conclude this stage of my studies.

Table of Contents

Dedication.....	ii
Acknowledgements.....	iii
Table of Contents.....	vi
List of Tables.....	vii
List of Figures.....	viii
Chapter 1: Introduction.....	1
1.1 Clap and Fling in Nature.....	1
1.2 Prior Research.....	4
1.3 Objectives of the Present Study.....	9
Chapter 2: Methodologies.....	11
2.1 Mathematical Model.....	11
2.2 Numerical Method.....	13
2.3 Parametric Space and Setup of the Computations.....	17
2.4 Clap and Fling Kinematics.....	19
Chapter 3: Results and analysis.....	30
3.1 Force distribution.....	30
3.2 Qualitative Description of Flow Field.....	43
Chapter 4 Summary-Conclusions.....	48
Appendix A.....	51
Appendix B.....	61
Forces.....	61
Flow field.....	64
Bibliography.....	80

List of Tables

Table 2.1 Cases investigated by numerical experiments.....	18
Table 3.1 Integrals for $C_L = f(t)$ for different time intervals within a period with trapezoidal rule.....	36
Table 3.2 Average lift coefficient for different phases indicating the differences between one and two wings setups.	37

List of Figures

Figure 1.1 Two dimensional representation of clap and fling stages. A. The wings approach with constant angle of attack. B. Rotation about the leading edge, denoted by a black circle. C. Clap D. Fling E. Rotation about the trailing edges. F. The wings translate apart from each other.	2
Figure 1.2 <i>Encarsia Formosa</i> . Morphology and wing's planform, taken by "Quick Estimates of Flight Fitness in Hovering Animals, Including Novel Mechanisms for Lift Production", by Torkel Weis-Fogh 1973.	3
Figure 2.1 Insect model depicting the reference frames used to describe the motion of the wings.	13
Figure 2.2 Flow around a pair of wings performing clap and fling. Iso-surfaces of the 2 nd invariant of the velocity gradient tensor identifying the vortical structures in the wake are shown at one instant during the flapping cycle. The isosurfaces are colored by the streamwise vorticity magnitude. The topology of the AMR grid is also shown.	15
Figure 2.3a Separation angle Θ on the stroke plane for 2° . The 30° angle with respect to the vertical is angle Ψ_m	17
Figure 2.3b Separation angle Θ on the stroke plane for 10° . The 30° angle with respect to the vertical is angle Ψ_m	18
Figure 2.4 Modified drosophila wing and geometrical simplification of wing for implementation of clap and fling and avoiding wing crossing	20
Figure 2.5 Wings and x, y, z axes of computational domain.	21
Figure 2.6 Realization of clap and fling	22
Figure 2.7 Beating angle with time. Time of clap initiation t_c and end of fling t_f are indicated. $k = 0.15$	23
Figure 2.8 Angle of attack (non filtered and filtered) varying with time. Time of clap initiation t_c and end of fling t_f are indicated. The filtering is exactly the same used for beating angle as described above.	25
Figure 2.9 Geometry of kinematic sequence for clap and fling. The 9 instances show correspond from left to right in each row to: 1. right after the start of the motion. 2. 0.25T 3. 0.5T 4. right before the start of clap 5-6 within clap 7-9 within fling. On each	

graph on the lower right the instant at which the frame corresponds is indicated. T=2.1384.....	29
Figure 3.1 Lift coefficient for case I.....	31
Figure 3.2 Lift coefficient for case II.....	32
Figure 3.3 Lift coefficient for case III	33
Figure 3.4 Lift coefficient with Reynolds number and separation angle as parameters for setup I.....	33
Figure 3.5 Lift coefficient with Reynolds number and separation angle as parameters for setup II.....	35
Figure 3.6 Axial force coefficient for case I.....	38
Figure 3.7 Axial force coefficient with Reynolds number and separation angle as parameters for setup I.....	39
Figure 3.8 Axial force coefficient with Reynolds number and separation angle as parameters for setup II.....	40
Figure 3.9 Lateral force coefficient for case I.....	41
Figure 3.10 Lateral force coefficient with Reynolds number and separation angle as parameters for setup I.....	42
Figure 3.11 Pressure contours for case I setup I at different instances within the first period for a slice vertical to the stroke plane at 65% of wing's length. Blue to red for lower to higher values from -0.5 to 0.5 and 61 contour levels. The 9 instances shown correspond from left to right in each row to: 1. right after the start of the motion. 2. 0.25T 3. right before the start of clap 4-5 within clap 6-9 within fling. On each graph on the lower right the instant at which the frame corresponds is indicated. T=2.1384	45
Figure 3.12. ω_x 2-color contours for case I setup I at different instances within the first period for two vertical to the stroke plane slices at 30% and 65% of wing's length. Blue to red for lower to higher values from -12 to 12 and 55 contour levels. The 9 instances shown correspond from left to right in each row to: 1. right after the start of the motion. 2. 0.25T 3. right before the start of clap 4-5 within clap 6-9 within fling. On each graph on the lower right the instant at which the frame corresponds is indicated. T=2.1384	46
Figure 3.13. Q=5 iso-surface colored by vorticity in x for case I setup I at different instances within the first period. Blue to red for lower to higher values from -12 to 12 and 55 contour levels. The 9 instances shown correspond from left to right in each row to: 1. right after the start of the motion. 2. 0.25T 3. right before the start of clap 4-	

5 within clap 6-9 within fling. On each graph on the lower right the instant at which the frame corresponds is indicated. $T=2.1384$	47
Figure A.1 Axial force coefficient for case II	61
Figure A.2 Axial coefficient for case III.....	62
Figure A.3 Lateral force coefficient case II.....	62
Figure A.4. Lateral force coefficient for case III	63
Figure A.5. Lateral force coefficient with Reynolds number and separation angle as parameters for setup II.	63
Figure A.6. Pressure contours for case I setup I at different instances within the first period for a slice vertical to the stroke plane at 65% of wing's length. Blue to red for lower to higher values from -0.5 to 0.5 and 61 contour levels. Three dimensional velocity vectors are also plotted. The 9 instances shown correspond from left to right in each row to: 1. right after the start of the motion. 2. $0.25T$ 3. right before the start of clap 4-5 within clap 6-9 within fling. On each graph on the lower right the instant at which the frame corresponds is indicated. $T=2.1384$	64
Figure A.7. Pressure contours for case I setup II at different instances within the first period for a slice vertical to the stroke plane at 65% of wing's length. Blue to red for lower to higher values from -0.5 to 0.5 and 61 contour levels. Three dimensional velocity vectors are also plotted. The 9 instances shown correspond from left to right in each row to: 1. right after the start of the motion. 2. $0.25T$ 3. Right before the start of clap 4-5 within clap 6-9 within fling. On each graph on the lower right the instant at which the frame corresponds is indicated. $T=2.1384$	65
Figure A.9. Pressure contours for case II setup II at different instances within the first period for a slice vertical to the stroke plane at 65% of wing's length. Blue to red for lower to higher values from -0.5 to 0.5 and 61 contour levels. Three dimensional velocity vectors are also plotted. The 9 instances shown correspond from left to right in each row to: 1. right after the start of the motion. 2. $0.25T$ 3. right before the start of clap 4-5 within clap 6-9 within fling. On each graph on the lower right the instant at which the frame corresponds is indicated. $T=2.1384$	67
Figure A.10. Pressure contours for case III setup I at different instances within the first period for a slice vertical to the stroke plane at 65% of wing's length. Blue to red for lower to higher values from -0.5 to 0.5 and 61 contour levels. Three dimensional velocity vectors are also plotted. The 9 instances shown correspond from left to right in each row to: 1. right after the start of the motion. 2. $0.25T$ 3. right before the start of clap 4-5 within clap 6-9 within fling. On each graph on the lower right the instant at which the frame corresponds is indicated. $T=2.1384$	68
Figure A.11. Pressure contours for case III setup II at different instances within the first period for a slice vertical to the stroke plane at 65% of wing's length. Blue to red	

for lower to higher values from 0.5 to 0.5 and 61 contour levels. Three dimensional velocity vectors are also plotted. The 9 instances shown correspond from left to right in each row to: 1. right after the start of the motion. 2. 0.25T 3. right before the start of clap 4-5 within clap 6-9 within fling. On each graph on the lower right the instant at which the frame corresponds is indicated. T=2.1384 69

Figure A.13. Q=5 iso-surfase colored by vorticity in x for case I setup II at different instances within the first period. Blue to red for lower to higher values from 12 to 12 and 55 contour levels. The 9 instances shown correspond from left to right in each row to: 1. right after the start of the motion. 2. 0.25T 3. right before the start of clap 4-5 within clap 6-9 within fling. On each graph on the lower right the instant at which the frame corresponds is indicated. T=2.1384 70

Figure A.14. Q=5 iso-surfase colored by vorticity in x for case II setup I at different instances within the first period. Blue to red for lower to higher values from 12 to 12 and 55 contour levels. The 9 instances shown correspond from left to right in each row to: 1. right after the start of the motion. 2. 0.25T 3. right before the start of clap 4-5 within clap 6-9 within fling. On each graph on the lower right the instant at which the frame corresponds is indicated. T=2.1384 71

Figure A.15. Q=5 isosurfase colored by vorticity in x for case II setup II at different instances within the first period. Blue to red for lower to higher values from 12 to 12 and 55 contour levels. The 9 instances shown correspond from left to right in each row to: 1. right after the start of the motion. 2. 0.25T 3. right before the start of clap 4-5 within clap 6-9 within fling. On each graph on the lower right the instant at which the frame corresponds is indicated. T=2.1384 72

Figure A.16. Q=5 iso-surfase colored by vorticity in x for case III setup I at different instances within the first period. Blue to red for lower to higher values from 12 to 12 and 55 contour levels. The 9 instances shown correspond from left to right in each row to: 1. right after the start of the motion. 2. 0.25T 3. right before the start of clap 4-5 within clap 6-9 within fling. On each graph on the lower right the instant at which the frame corresponds is indicated. T=2.1384 73

Figure A.17. Q=5 iso-surfase colored by vorticity in x for case III setup II at different instances within the first period. Blue to red for lower to higher values from 12 to 12 and 55 contour levels. The 9 instances shown correspond from left to right in each row to: 1. right after the start of the motion. 2. 0.25T 3. right before the start of clap 4-5 within clap 6-9 within fling. On each graph on the lower right the instant at which the frame corresponds is indicated. T=2.1384 74

Figure A.18. ω_x contours for case I setup II at different instances within the first period for two vertical to the stroke plane slices at 30% and 65% of wing's length. Blue to red for lower to higher values from -12 to 12 and 55 contour levels. The 9 instances shown correspond from left to right in each row to: 1. right after the start of the motion. 2. 0.25T 3. right before the start of clap 4-5 within clap 6-9 within fling.

On each graph on the lower right the instant at which the frame corresponds is indicated. T=2.1384 75

Figure A.19. ω_x contours for case II setup I at different instances within the first period for two vertical to the stroke plane slices at 30% and 65% of wing's length. Blue to red for lower to higher values from -12 to 12 and 55 contour levels. The 9 instances shown correspond from left to right in each row to: 1. right after the start of the motion. 2. 0.25T 3. right before the start of clap 4-5 within clap 6-9 within fling. On each graph on the lower right the instant at which the frame corresponds is indicated. T=2.1384 76

Figure A.20. ω_x contours for case II setup Ii at different instances within the first period for two vertical to the stroke plane slices at 30% and 65% of wing's length. Blue to red for lower to higher values from -12 to 12 and 55 contour levels. The 9 instances shown correspond from left to right in each row to: 1. right after the start of the motion. 2. 0.25T 3. right before the start of clap 4-5 within clap 6-9 within fling. On each graph on the lower right the instant at which the frame corresponds is indicated. T=2.1384 77

Figure A.21. ω_x contours for case III setup I at different instances within the first period for two vertical to the stroke plane slices at 30% and 65% of wing's length. Blue to red for lower to higher values from -12 to 12 and 55 contour levels. The 9 instances shown correspond from left to right in each row to: 1. right after the start of the motion. 2. 0.25T 3. right before the start of clap 4-5 within clap 6-9 within fling. On each graph on the lower right the instant at which the frame corresponds is indicated. T=2.1384 78

Figure A.22. ω_x contours for case III setup II at different instances within the first period for two vertical to the stroke plane slices at 30% and 65% of wing's length. Blue to red for lower to higher values from -12 to 12 and 55 contour levels. The 9 instances shown correspond from left to right in each row to: 1. right after the start of the motion. 2. 0.25T 3. right before the start of clap 4-5 within clap 6-9 within fling. On each graph on the lower right the instant at which the frame corresponds is indicated. T=2.1384 79

Chapter 1: Introduction

1.1 Clap and Fling in Nature

In the early 1970's, Torkel Weis-Fogh in his classical paper entitled "Quick Estimates of Flight Fitness in Hovering Animals, Including Novel Mechanisms for Lift Production" [83], suggested a new aerodynamic mechanism called "Clap and Fling", to explain the enhanced aerodynamic forces produced by some insects. He came to this conclusion by observing *Encarsia Formosa* adults -a tiny chalcid wasp, which is an economically important parasite used in the greenhouse aphids- in free flight. A simplification in two dimensions of the kinematic pattern characteristic of "Clap and Fling", which occurs at dorsal stroke reversal, is shown in Figure 1.1. During the clap, the insect brings the leading edges of the two wings together (Fig. 1A) and then rotates them until the 'V-shaped' gap vanishes and the wings become parallel (Fig. 1B-C). During the fling, the wings' rotation axis switches from the leading to the trailing edge creating the 'V-shaped' gap shown in Fig. 1D. When a maximum angle is reached the wings start to move apart (Figs. 1E-F) designating the onset of the downstroke. Weis-Fogh [83] used the kinematic data from his observations (i.e., motion's frequency, amplitude, angle of attack) together with detailed measurements of the sizes and shapes of the wings (see Figure 1.2) to calculate the minimum lift coefficient, which must be ascribed to the wings so that the insect can sustain its weight.

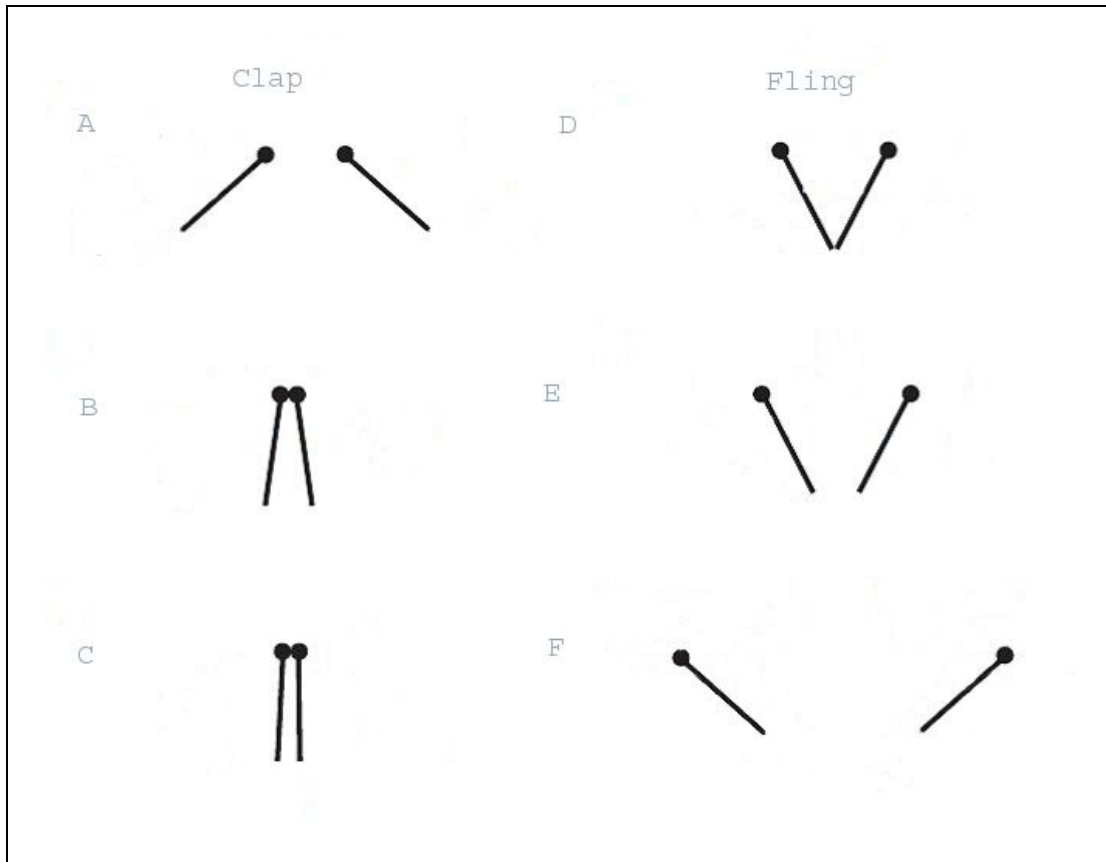


Figure 1.1 Two dimensional representation of clap and fling stages. A. The wings approach with constant angle of attack. B. Rotation about the leading edge, denoted by a black circle. C. Clap D. Fling E. Rotation about the trailing edges. F. The wings translate apart from each other.

For the case of the *Encarsia Formosa*, for example, his calculations revealed an unusually high lift coefficient of value 3.2. Despite the drastic assumptions in the computation of C_L , he argued that the clap and fling was responsible for this enhancement. Ellington [20] recalculated C_L from the above kinematics by incorporating a more accurate theoretical model, and found it to be significantly lower ($C_L = 1.6$) but still fairly high.

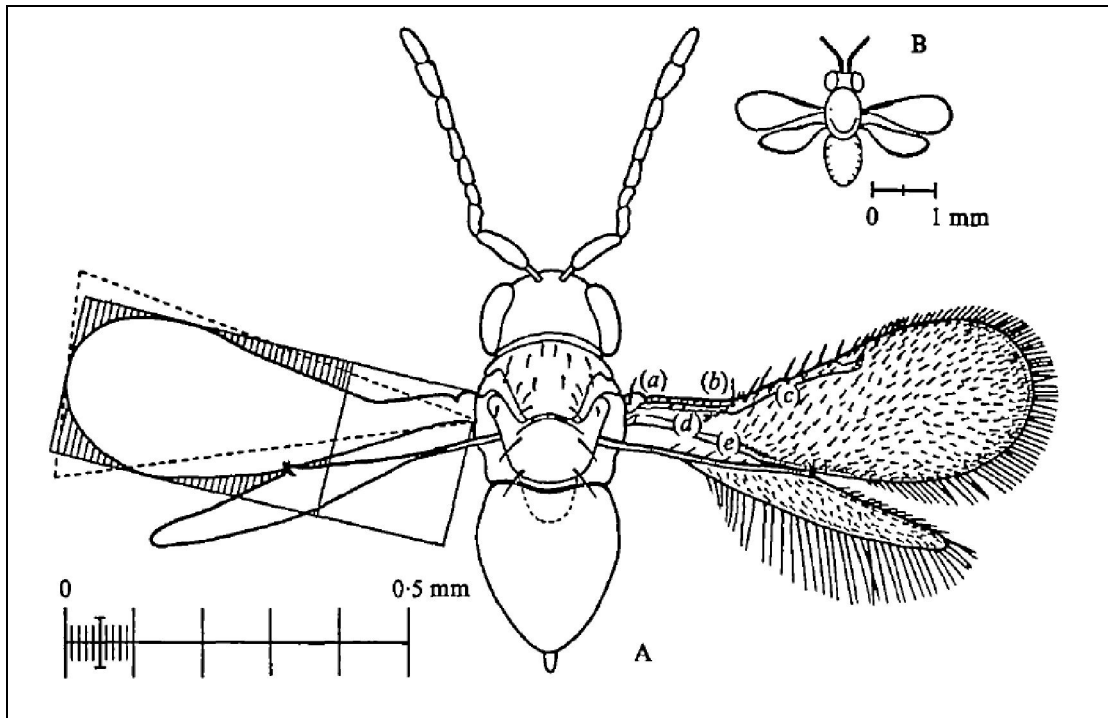


Figure 1.2 *Encarsia Formosa*. Morphology and wing's planform, taken by "Quick Estimates of Flight Fitness in Hovering Animals, Including Novel Mechanisms for Lift Production", by Torkel Weis-Fogh 1973.

Later papers reported kinematic patterns that are identical or similar to the ones discussed by Weis-Fogh [83]. In one of the proposed variations, the so called "clap and peel", the elasticity of the wings plays an important role, It has been observed in tethered flying *Drosophila* [35], various species of butterflies [13], [25], [27], [8], [10], bush cricket, mantis [7], [8] [9] and locusts [12]. Ellington [25], [27] and later Ennos [31] reported the "near clap-and-fling" pattern, where the two wings do not clap completely but come close to each other. It was observed in the white butterfly *Pieris barssicae*, the bluebottle *Calliphora vicina*, and the flour moth

Ephista, where the wings approach at the dorsal stroke reversal without physically touching during the clap.

How extensively clap and fling or variations is utilized by various insects to enhance lift is not well understood. In general, observations show that small insects appear to use it more often [25], [27], [31], [84], which led to the hypothesis that clap and fling might be vital for adequate lift production in small insects operating at low Reynolds numbers. A noteworthy exception is the fruit fly, *Drosophila melanogaster*, which rarely employs clap-and-fling during free flight [31], [34] but frequently utilizes this mechanism under tethered conditions [77], [35], [90], [39]. Clap and fling by larger insects has not been observed as frequently. They may use it, however, under extreme load conditions [47], or power demanding manoeuvres [12]. Ellington's observations of larger insects [25], [27] revealed clap and fling like kinematics for the Large Cabbage White Butterfly *Pieris brassicae* (found as well by Weish-Fogh), the plum moth *Emmelina* and the flour moth *Ephestia*. He also suggested that the lacewing *Chrysopa carnea* uses clap and fling, not only for lift augmentation, but also for steering and flight control. As an unsteady aerodynamic mechanism, clap and fling has attracted a lot of attention. Many books written on animals' flight refer to it extensively, as a promising yet not quite explored flying pattern [18], [61], [76].

1.2 Prior Research

Experimental, theoretical, and computational approaches have been utilized over the years to better understand how the clap and fling kinematics used by various insects

may lead to gains in aerodynamic performance. Lighthill [45] was amongst the first to study clap and fling theoretically. He assumed inviscid, two-dimensional flow [37], where the wings are represented by rigid plates of zero thickness. He pointed out that when the fling phase starts, circulations of same magnitude but opposite sign around the two wings are generated so there is no violation of Kelvin's circulation theorem - the two circulations have add up to zero around the system of the two wings- while the proximity of the trailing edges significantly attenuates effects from starting vortices. In effect, the clap and fling was proposed as a possible "cure" to the Wagner effect (i.e. the gradual development of the necessary circulation around an impulsively started airfoil due to the starting vortex in its wake, [80]). In particular, he found the circulation to vary from infinity at the onset of fling to a minimum value of $\Gamma = 0.69\omega c^2$ at $\theta=120^\circ$, where θ is the opening angle between the plates, ω is the angular velocity, and c the chord length. As a result, when the plates begin to move away from each other with velocity U , a lift force corresponding to $\rho U \Gamma$ per unit span immediately develops. In the case of the classical problem of an impulsively started single plate trailing edge vorticity needs to be continuously generated for and for the lift force to increase gradually to its asymptotic value. In the above scenario the viscous effects, which are important given the low Reynolds number in this flow, has been neglected. Lighthill [44], [45] provided a qualitative description of their effects. He emphasized that the weight of the insect would be balanced by the impulse of a chain of downward moving vortex rings which at large distances below the insect would be merged by the action of viscous effects into a laminar jet like motion.

The theoretical work was continued by Ellington [20] who used Lighthill's estimates for the circulation and concluded that the circulation of clap and fling is way above the circulation predicted by steady aerodynamics (i.e. simple translational motion with a lift coefficient that satisfies the Kutta condition). He proposed a model to estimate the transient circulation building up around the wing inspired by the work of Wagner [82] and Walker [79]. Edwards-Cheng [19] extended Lighthill's [45] inviscid analysis by incorporating a vortex shedding model with separation from the salient corners of the wings during fling. They also reported that circulation increases with a large stroke plane amplitude. A similar approach was proposed by Wu *et al.* [88] with identical findings.

Given the limitations of theoretical models, which were all based on inviscid flow theory, several experimental studies were also conducted in the laboratory in simplified configurations. Bennett [5] conducted two-dimensional experiments on clap and fling by using a rectangular plate with 4% thickness and rounded leading edge as wing. He simulated the existence of the other wing by using a mirror plane (wall). The Reynolds number of his measurements was roughly 83000 and the angular velocity ω was in the range of 31-69 r/s . His main observations were that the lift (of which indicative is the induced velocity) in clap and fling appeared to increase 15% during the fling compared to a one wing case.

Maxworthy [48] conducted two and three-dimensional flow visualization studies with trapezoidal wing platforms. The Reynolds number, $Re = \dot{\omega} c_o^2 / \nu$, where $\dot{\omega}$ is the angle rate of change, c_o is the maximum chord length and ν is the kinematic viscosity of the ambient fluid, varied between 13.000 and 32. He found the following: (i) the

circulation was measured to be significantly larger than the one calculated theoretically by Lighthill [45]; (ii) the flow is highly three-dimensional; and (iii) clap appears to exhibit higher contribution to the generation of lift than fling. All the above results were also supported by later work by Spedding *et al.* [64]. Sunada *et al.* [69] conducted experimental as well as computational work on the near clap and fling mechanism. Their wing platforms included rectangular and triangular plates of very small thickness (0.05c). The main finding of their work was that the interaction between the two plates was substantial only when the maximum angle between the two wings was held small.

In 2005 Lehmann *et al.* [43] explored the fluid dynamics of clap-and-fling in great detail by using a dynamically scaled two-winged flapper based on the *Drosophila* wing (see also [59], [17]) for Reynolds numbers in the range 50-200. They measured the forces during the entire stroke simultaneously with the resulting flow. The limitation of the distance between the hinges resulted in a clap and fling pattern in which the two wings do not stop their rotation while approaching each other when they are parallel, but they continue until their tips meet. In general, their results were very sensitive to the wing kinematics and suggested a maximum overall lift enhancement of 17% compared to a single wing case. Their results demonstrated some very interesting differences with previous studies: i) clap contributes less to the lift force compared to fling, which is contradictory to Maxworthy's [35] finding; and ii) it was observed that lift increases at the onset of the upstroke, something that was not expected. Possibly hence, clap-and-fling wing beat can alter wake structure throughout the entire stroke cycle.

Given the limitations of experiments, computational studies can provide useful insights into the physics of such complex problems. Sun *et al.* [68] performed two-dimensional simulations of clap and fling by using an elliptic planform of 4% thickness and leading edge radius of 0.08%. They found that as the smallest distance between the wings increases the lift and torque enhancement are severely diminished, resulting in almost no interference effects when the distance is about one chord length. An interesting conclusion of this paper was that going from a distance of $0.1c$ to $0.2c$ between the hinges of the ‘insect’ the lift enhancement is still considerable but the torque coefficient is attenuated, implying that an optimized setting should make sure that the wings are close enough, but not so close to have detrimental torque requirements.

Miller *et al.* [51] performed two-dimensional computations with immersed boundary method for an idealized clap and fling and a ‘fling’ half stroke, following the experimental setting of Dickinson *et al.* [14]. They calculated lift coefficients as functions of time per wing performing a parametric study for Reynolds number between 8 and 128. Their results in general show that the clap and fling is more pronounced for low Reynolds number since lift enhancement which is apparent for both the rotational and translational phases of the insect’s motion, increases with decreasing Reynolds number. Drag coefficients produced during fling are also substantially higher for the two winged case than the one wing case. They also reported substantially increased lift during the translational part of the motion.

1.3 Objectives of the Present Study

From the above literature survey, it is clear that several outstanding questions regarding the clap and fling mechanism remain. There are also sceptics who suggest that the clap and fling mechanism is simply an attempt by an insect or bird to maximize the stroke amplitude, which can significantly enhance lift generation. Several studies suggest that peak lift production in both birds [11] and insects [43] is constrained by the roughly 180° anatomical limit of stroke amplitude. Animals appear to increase lift by gradually expanding stroke angle until the wings either touch or reach some other morphological limit with the body. Thus, an insect exhibiting a clap may only be attempting to maximize stroke amplitude. Another point of ambiguity has also been the Wagner effect, which is not so prominent in small insects. Some of the questions the thesis author will attempt to address in this study are the following:

- Why do insects use clap and fling? Is it a cost-efficient mechanism resulting to a stable enhancement of lift or it is only useful under extreme load conditions?
- Is clap and fling simply an attempt to maximize the stroke amplitude?
- How important are the kinematics?
- What is the effect of the Reynolds number?
- What is the relation between the aerodynamic forces and the flow patterns that develop during clap and fling?

In particular we will use a high-fidelity Navier-Stokes solver for viscous incompressible flow to simulate the unsteady, three-dimensional flow generated by a moving pair of wings at various Reynolds numbers. We will also examine different kinematics patterns by varying two main sets of parameters: (i) parameters quantifying the level of proximity of the wings during clap, such as the separation angle and the distance between the hinges of the wings and (ii) parameters quantifying the time dependence of the motion such as the flapping frequency and amplitude, angle of attack and so on. The detailed parametric space we have selected will be discussed in the next chapter.

In the following chapter we will describe the methodology used to counter our problem. The mathematical model employed will be given in detail. Then we will summarize the numerical methods incorporated into our code which performs the simulations.

Chapter 2: Methodologies

2.1 *Mathematical Model*

Most of the experimental work conducted today points to the fact that the clap and fling mechanism is most effective in a fairly low Reynolds number regime, i.e. $10 < \text{Re} < 10^3$. As a result, the flow can be considered to be incompressible and is governed by the Navier-Stokes equations,

$$\frac{\partial u_j}{\partial x_j} = 0 \quad (2.1)$$

$$\frac{\partial u_i}{\partial t} + \frac{\partial u_i u_j}{\partial x_j} = -\frac{\partial p}{\partial x_i} + \frac{1}{\text{Re}} \frac{\partial^2 u_i}{\partial u_i \partial u_j} + f_i \quad (2.2)$$

where x_i, x_j ($i, j = 1, 2, 3$) are the Cartesian coordinates, u_i, u_j are the velocity components in the corresponding directions, and f_i are the body forces [54]. The equations are written in dimensionless form. The velocity components and distances have been scaled by a reference velocity U and a reference length l respectively. The pressure is normalized by ρU^2 , with ρ being the density of the fluid, and Re is the Reynolds number defined as

$$\text{Re} = \frac{Ul}{\nu} \quad (2.3)$$

The Navier Stokes equations need to be solved in a coupled manner with the equations governing the dynamics of the wings. Although the latter are membrane like, deformable structures in the present work will be assumed to behave as rigid plates with zero thickness. In particular, we will consider two rigid wings termed as RW (right wing) and LW (left wing), hinged at points R and L respectively on the virtual insects' thorax (see Figure 1). From now on, and unless otherwise stated, we may also refer to the two wings also as Rigid Body 3 for the right wing (RB3) and Rigid Body 4 for the left wing (RB4), while non-existent bodies in the present case the head-thorax and abdomen are called with RB1 and RB2, respectively [73].

In all computations reported in this study we will be prescribing the motion of the wings, thus also prescribing the local velocities and accelerations of any point on the wings. To facilitate the 'translation' of the kinematics to boundary conditions for the Navier-Stokes solver we will utilize an Euler angle sequences [3]. Euler angle sequences are named after the order of rotation about successive axis starting from a coordinate system whose axis are 1, 2 and 3. The 3-1-3 sequence, for example, has been frequently used to locate the orbit of a body in space, the 3-2-3 for the description of rotating bodies, and 3-2-1 in aerodynamics. The particular angle sequence most suitable is problem dependent. The calculation of angular velocities, which is a critical part in our case, is always susceptible to the inherent limitations of Eulerian angle sequences [3]. Every sequence presents a singularity for the value of annihilation of the angle of the second rotation. Here, we selected the 3-2-1 sequence, where the singularity for the second angle lies at $\pm 90^\circ$, which never appears in our kinematics.

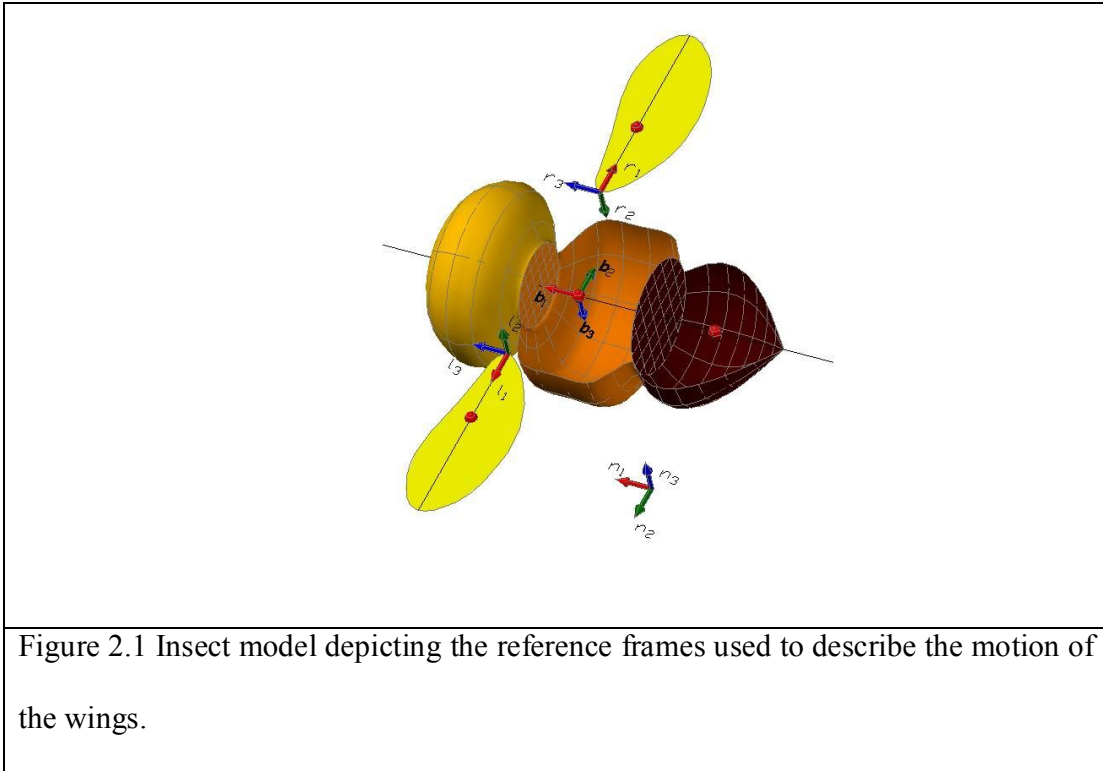


Figure 2.1 Insect model depicting the reference frames used to describe the motion of the wings.

To fully describe the overall kinematic mechanism, we will derive the transformation matrices for each member of the kinematical chain shown in Figure 2.1 in terms of the relevant Eulerian angles. The derivation of the necessary angular and translational velocities and accelerations of each body participating in our system is presented in detail in Appendix A.

2.2 *Numerical Method*

A high-fidelity Navier-Stokes solver for viscous incompressible flows will be utilized for the unsteady three-dimensional flows under consideration. The main challenge that needs to be addressed in such computations is the proper treatment of dynamically moving boundaries undergoing large displacements. To address this challenge, we will use a highly accurate, cost/efficient strategy, where the dynamics of the flow are computed on a fixed Eulerian grid, while a Lagrangian description is

used for the structure(s). The requirement for the Eulerian grid to conform to the body is relaxed and boundary conditions are imposed using an embedded-boundary approach. Adaptive mesh refinement (AMR) is also utilized to cluster grid points in areas of high velocity gradients.

In particular, in the current AMR strategy a single-block solver is employed on a hierarchy of subgrids with varying spatial resolution. Each of these subgrid blocks has a structured Cartesian topology, and is part of a tree data-structure that covers the entire computational domain. An example is shown Fig. 2.2 for the flow around a hovering wing pair. The grid has been refined near the wings to capture high velocity gradients and is relaxed in the wake. The subgrid block topology is shown at a plane approximately parallel to the stroke plane. Each block has a fixed resolution of 16^3 grid points and the refinement on each level is achieved by bisection of a coarser block in all the coordinate directions. The solution is only computed at the finest subgrid block in each point in space (leaf blocks). The grid hierarchy, restriction and prolongation operators, and guard-cell filling between neighboring blocks are managed by using the PARAMESH toolkit (MacNeice *et al.*[46]).

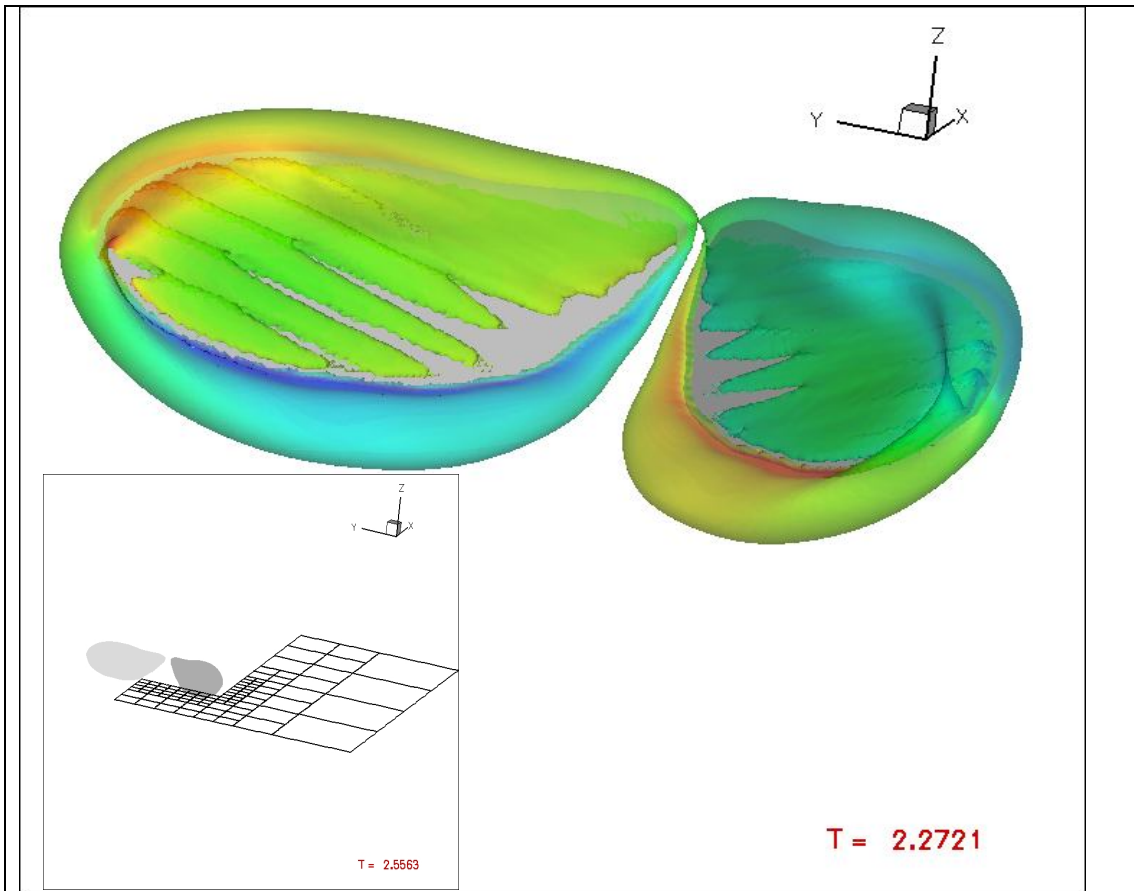


Figure 2.2 Flow around a pair of wings performing clap and fling. Iso-surfaces of the 2nd invariant of the velocity gradient tensor identifying the vortical structures in the wake are shown at one instant during the flapping cycle. The isosurfaces are colored by the streamwise vorticity magnitude. The topology of the AMR grid is also shown.

In each sub-block a staggered, second-order accurate, central finite difference solver is used. The time advancement is done by using an explicit, Adams-Bashforth, fractional-step approach [33], [36].

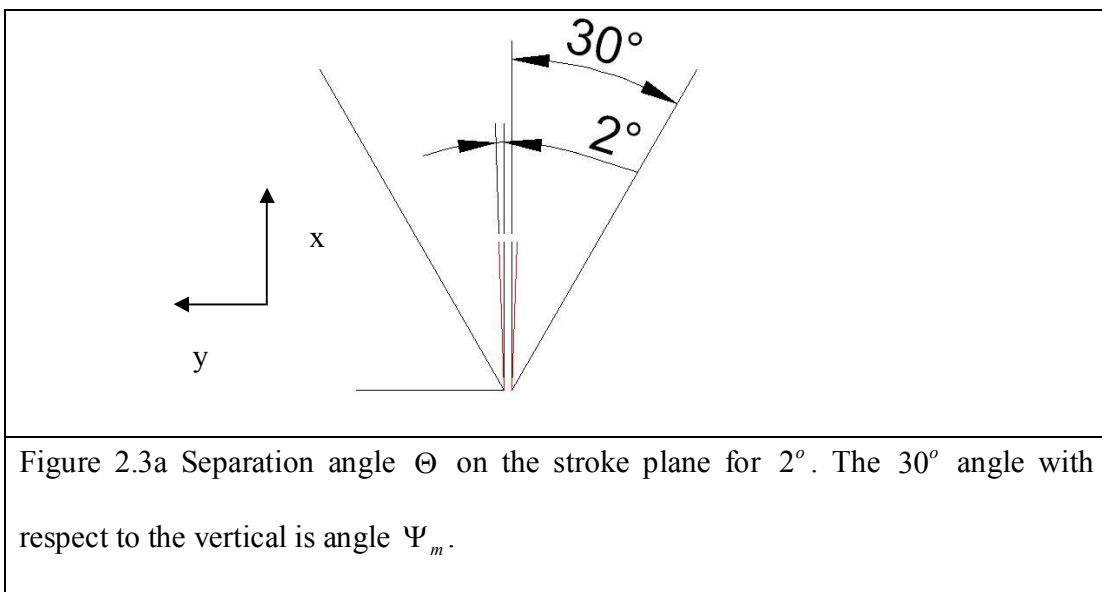
In the AMR solver, boundary conditions are required at both the physical boundaries of the domain and the interior block boundaries, and they are enforced with a layer of ghost cells surrounding each subgrid block. These ghost cells on the interior block

boundaries are filled by using the solution data from neighbouring subgrid blocks. Quadratic interpolation is required in the ghost-cell filling operation to maintain a second order spatial accuracy of the method. Also, the mass fluxes between different blocks sharing an interface are matched such that inter-block continuity is preserved. The overall solver is second order accurate both in space and time. Details can be found in the work by Vanella *et al.* [75].

Due to the structured Cartesian topology of each of the sub-blocks, any body immersed into this grid will almost never be aligned with the gridlines. As a result imposing boundary conditions is not trivial. To address this issue we use a scheme, which is robust and efficient when dealing with fluid-structure interactions amongst multiple bodies. It utilizes a “direct forcing” function, which is, however, computed on the Lagrangian markers rather than the Eulerian points as it is done classical direct forcing schemes (see for example [2],[89], [32], [70]). We then use transfer operators, which are constructed by using moving least squares (MLS) shape functions with compact support. A series of tests which have been conducted, show that the above scheme maintains the second-order spatial accuracy of the overall numerical method and it is very well suited for problems with moving-deforming-colliding bodies. It renders a low level of noise on the forces acting on moving bodies and it can handle problems where immersed bodies come in to contact. It also reduces dramatically the complexities encountered when dealing with membrane like structures such as insect wings. Details can be found in the work of Vanella and Balaras [74].

2.3 Parametric Space and Setup of the Computations

As we already discussed the gains from clap and fling appear to be maximized at low Reynolds numbers. Based on results already in the literature we will consider two values of the Reynolds number, $Re=Ul/v=64$ and 250, where l is the length of the wing and U is the maximum velocity on the chord positioned at $0.65R$ [81]. Narrowing down the parametric space on the side of the kinematics is a much more difficult task, given that in most studies in the literature the detailed kinematics have not been recorded. In the present study we will focus on the effects of the level of proximity between the two wings during clap, and we will use the case of a single wing moving with the same kinematics as the extreme case where no interaction occurs. To vary the level of proximity between the two wings we fixed the distance between the two hinges at 5% of the length of the wing, and varied the separation angle between the wings, Θ (see Figure 2.3).



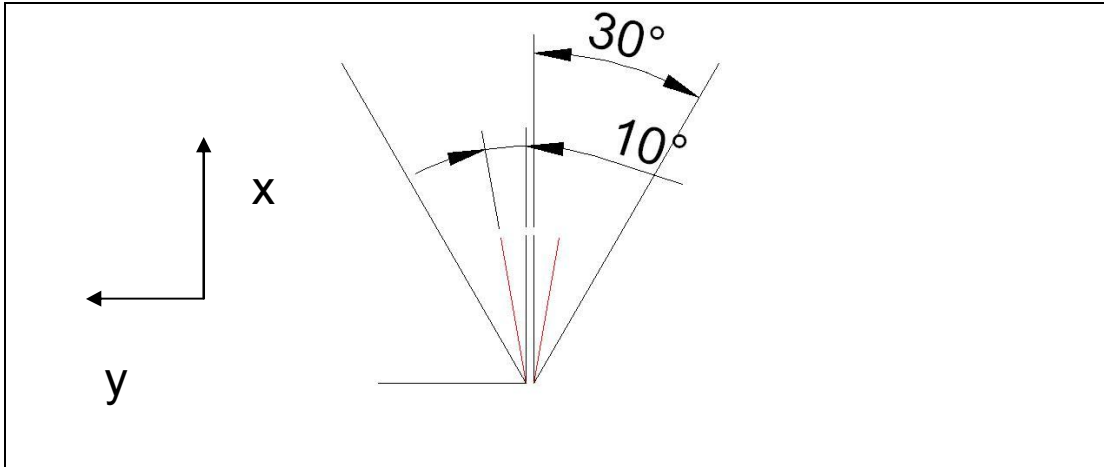


Figure 2.3b Separation angle Θ on the stroke plane for 10° . The 30° angle with respect to the vertical is angle Ψ_m .

In table 2.1 a summary of the different cases is considered. For each of these cases, a computation with a single wing at the same Re and kinematics has also been conducted for comparison.

	Case I	Case II	Case III
Reynolds number	64	64	250
Separation angle	$\Theta = 2^\circ$	$\Theta = 10^\circ$	$\Theta = 2^\circ$

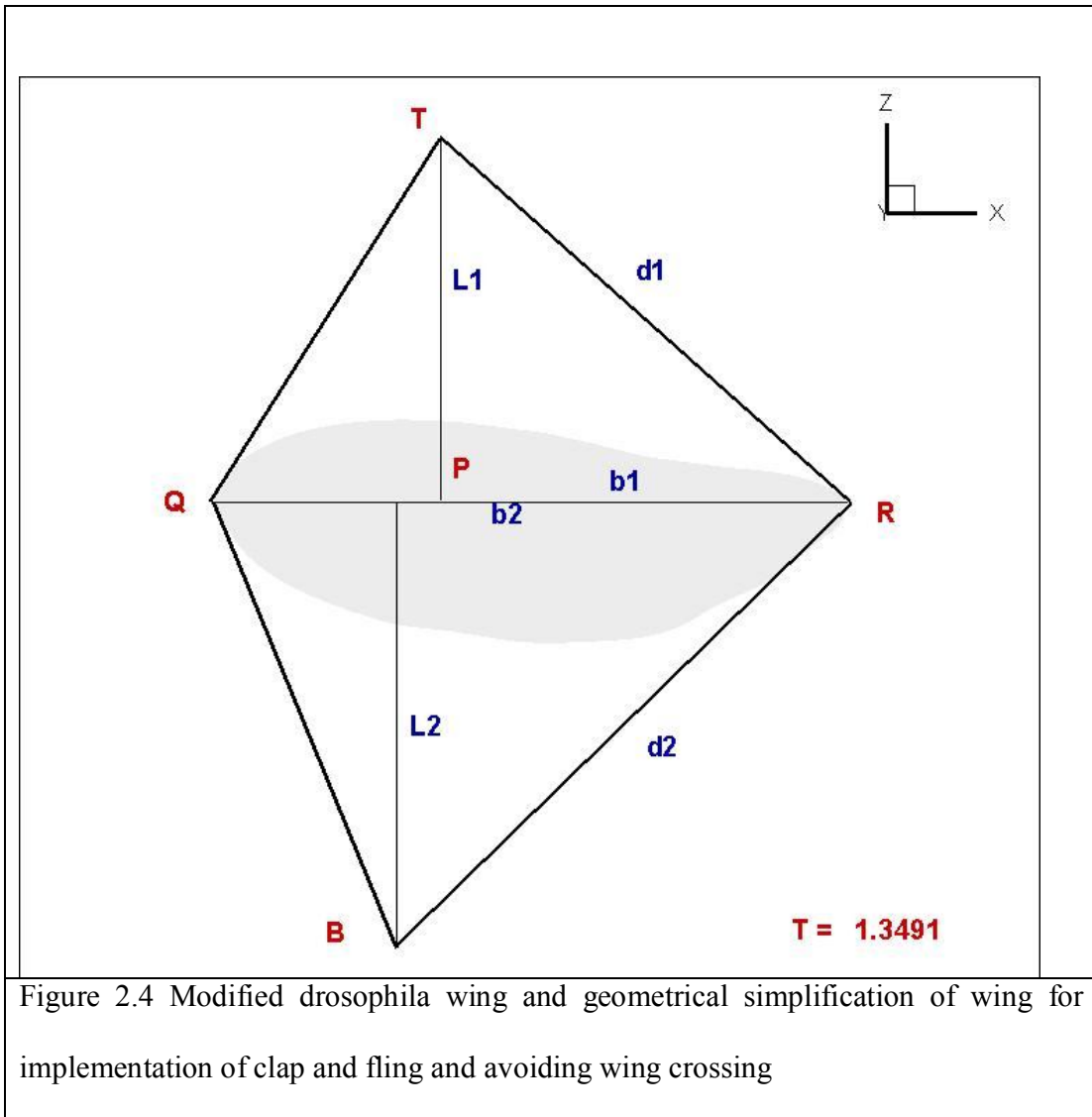
Table 2.1 Cases investigated by numerical experiments.

For all calculations, the computational domain is a box with dimensions $4 \times 6 \times 6$ along the x, y and z axes respectively using 2 blocks/length in each direction. The runs were made using 4 levels of refinement in our AMR code. The cell size at level zero was $h_o = 0.125$ and at level 4, $h_4 = \frac{h_o}{2^4} = 0.078125$ (non-dimensional). We

used constant CFL criterion instead of a constant time step. The boundary conditions used were Dirichlet in the z direction, and periodic in x and y. The wings are hinged at points $(0, 0.025, 0)$ and $(0, -0.025, 0)$, giving a distance of 5% of the length of the model wing used. This means that we were able to have 6 points of our grid between the two hinges.

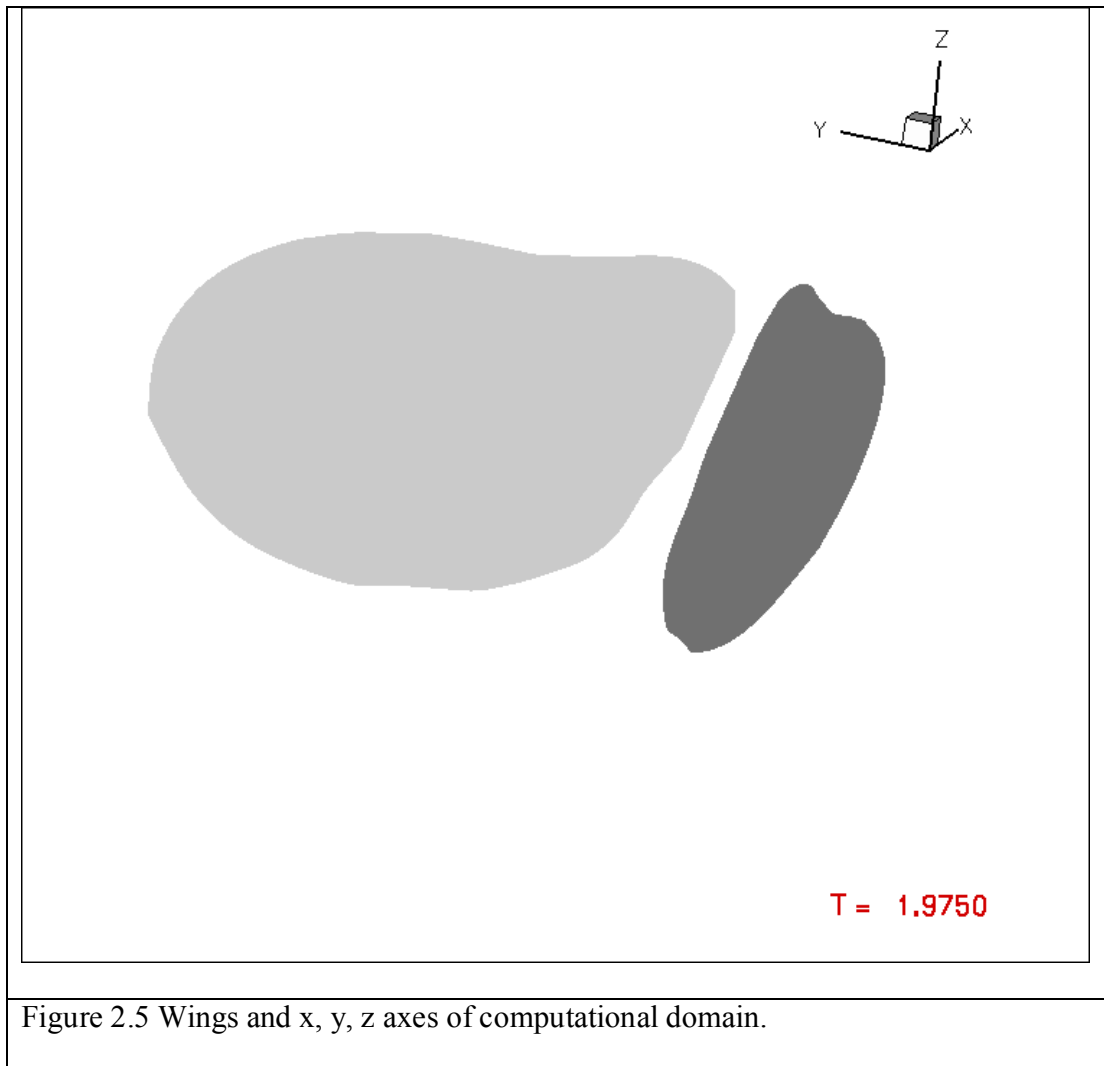
2.4 Clap and Fling Kinematics

As has been already discussed, there are no detailed kinematics available in the literature for insects performing clap and fling. For simplicity, we used symmetric and harmonic functions. The out of the stroke plane angle is also assumed to be zero, a limitation imposed by the singularity of the Euler angles' sequence (see below). The wing platform that is used is the wing of *Drosophila Malanogaster* used by Dickinson in a series of papers [81], [6], [60], [43]. This wing is shown in Figure 2.4, along with a slight modification performed in order to avoid the unphysical condition of wings' crossing each other. The idea for the avoidance of crossing is as follows: if one draws a tangent lines from the hinge of the wing to some point on the upper and another point on the lower circumference such that all other points of the wing are within the region of these two lines, and then make sure that these lines, properly constructed for both wings, are the limits of the wings' contact, this ensures that no point of the one wing will make it into the domain of the other.



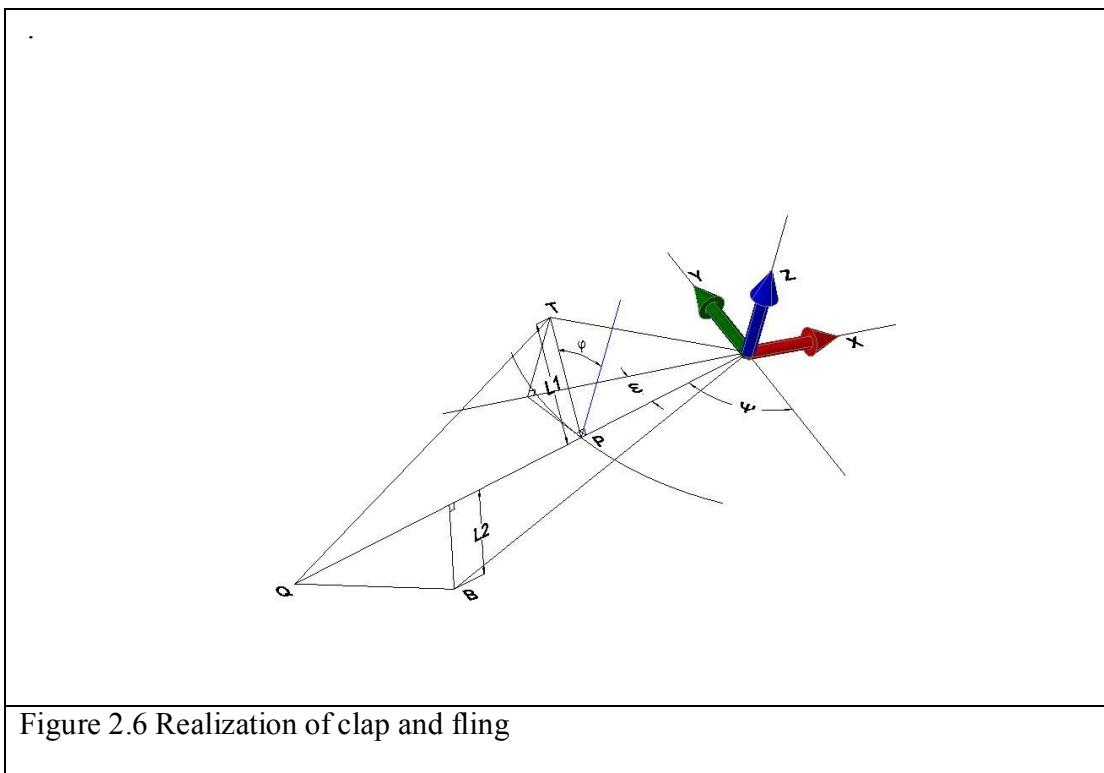
In Figure 2.1, the insect model and the reference frames used to describe the motion of the wings are shown. To simulate hovering and have the insect's body almost vertical, and the stroke plane angle almost horizontal, we performed a 90° rotation about axis \hat{b}_2 . It is noted here, that although we have performed a 90° rotation around \hat{b}_2 we do not face a problem from the Eulerian angles singularity, because we do not compute any angular velocities for RB1. Now the insect is in an upright position.

In this position, we ascribe axes x , y and z , associated with the computational domain, as shown in Figure 2.5.



In the above, x , is along the longitudinal axis of the wing and y is along the perpendicular to the wings when they face each other at their closest distance. z follows the direction imposed by the right hand rule. In this way, the plane of symmetry, i.e. the x - z plane, is a representation of the dorsal-ventral plane and the stroke plane is in the x - y plane.

The simplified wing geometry defined in Figure 2.4 hinged in R, rotates with line RP lying on the stroke plane and the angle described by this line on the x-y plane is angle Ψ (see Figure 2.6). This angle is associated with an angle around axis 3 of the R coordinate system. The out of plane angle is taken to be zero. Finally, the angle of attack Φ is associated directly to the angle around axis 1 of the R coordinate system, ϕ . The amplitude of Ψ is $\Psi_A=30^\circ$ with respect to two symmetrical axes at a 30° angle each with respect to the x negative half-axis, producing in this way symmetrical beating of the two wings, are being the mirror image of the other. Two different periodic functions could be used as beating angle functions, namely one harmonic and one triangular shaped function as shown in Figure 2.7.



More specifically, the functions given in Figure 2.7 are described by equations (2.4) and (2.5).

$$\Psi(t) = \Psi_m + \Psi_A \sin(\omega t) \quad (2.4)$$

$$\Psi(t) = \begin{cases} \Psi_m + \frac{t}{0.25T}(1+k)\Psi_A, & t < 0.25T \\ \Psi_m - \frac{t-0.5T}{0.25T}(1+k)\Psi_A, & 0.25T < t < 0.75T \\ \Psi_m + \frac{t-T}{0.25T}(1+k)\Psi_A, & 0.75T < t < T \end{cases} \quad (2.5)$$

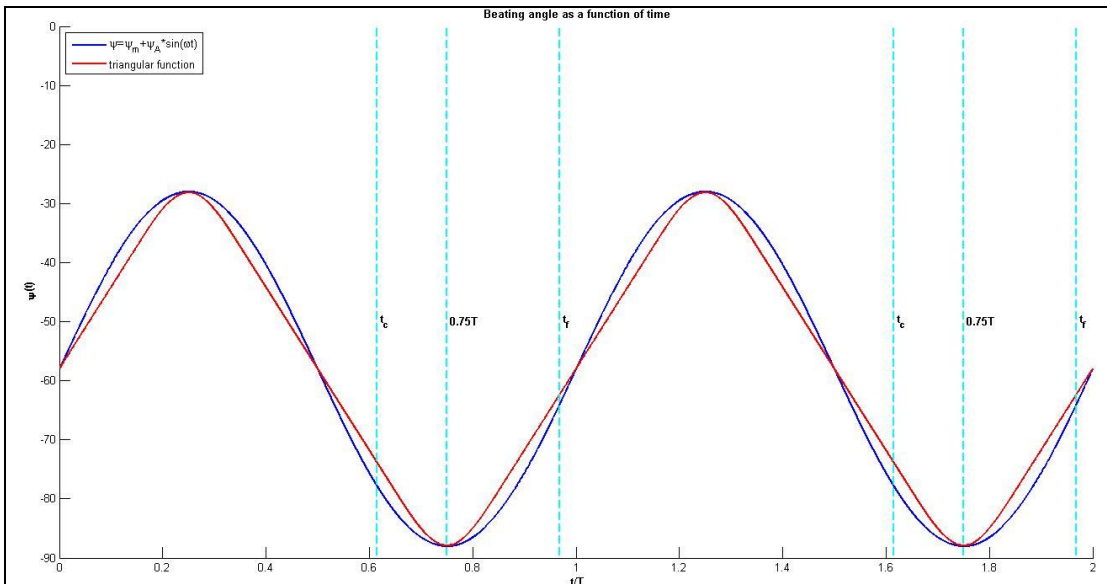


Figure 2.7 Beating angle with time. Time of clap initiation t_c and end of fling t_f are indicated. $k = 0.15$

In (2.5), k is a constant allowing us to illustrate different functions.

As long as the angle of attack is concerned, the variation of which is related to the rotation of the clap and fling motion, the kinematical pattern used is composed

of five distinct time intervals during each period as defined mathematically in equation (2.6) and shown in Figure 2.8. At the start of the period and for wings assumed to travel initially apart from each other, we employed a simple harmonic cosine function until the half of the period. For $0.5T < t < t_c$ we fixed the value of the angle of attack constant to its value at the end of the previous harmonic phase, Φ_o . At some point t_c in time, depending only on the geometry of the wing as explained later on, between the half and three fourths of the period, the clap motion starts. This is continued until the three fourths of the period, time at which the fling phase is initiated. The end of fling notated as t_f takes place only a while, before the end of the first period and the onset of the new one and it is characterized by constant angle of attack $\Phi = -\Phi_o$. Obviously we have considered the period of the variation of the two angles in any case to be the same.

$$\Phi(t) = \begin{cases} -\Phi_o \cos \omega t, & t < 0.5T \\ \Phi_o, & 0.5T < t < t_c \\ a \sin\left(-\frac{b_1}{l_1} \cot \Psi\right), & t_c < t < 0.75T \\ a \sin\left(\frac{b_2}{l_2} \cot \Psi\right), & 0.75T < t < t_f \\ -\Phi_o, & t_f < t < T \end{cases} \quad (2.6)$$

Returning to Figure 2.6, we will now describe the clap and fling realization for $t_c < t < t_f$ by relating the wing geometry and the timing of rotation. During the clap phase, as the wings approach each other with a constant angle of attack they ‘‘meet’’ the vertical plane of symmetry both with lines d_1 on this plane and a common point T (Top) corresponding to distances l_1 and b_1 . T is gradually rising bringing the wings

more and more to an upright opposition simultaneously causing them to rotate.

Calling α_1 the angle between b_1 and d_1 ,

$$\alpha_1 = a \tan\left(\frac{l_1}{b_1}\right) \quad (2.7)$$

and

$$c_1 = l_1 \sin(\Phi) = -b_1 \tan\left(\Psi + \frac{\pi}{2}\right) \Rightarrow l_1 \sin(\Phi) = -b_1 \cot(\Psi) \quad (2.8)$$

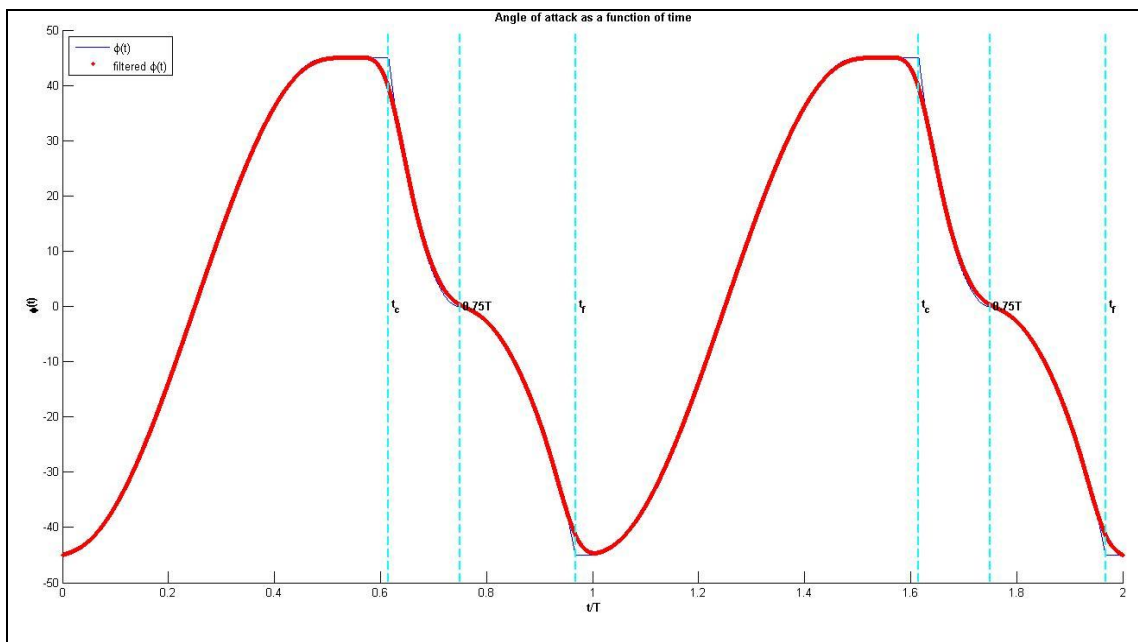


Figure 2.8 Angle of attack (non filtered and filtered) varying with time. Time of clap initiation t_c and end of fling t_f are indicated. The filtering is exactly the same used for beating angle as described above.

We find the geometric relation between angle of attack and beating angle for the clap phase as:

$$\Phi(\Psi(t)) = a \sin\left(-\frac{b_1}{l_1} \cot(\Psi(t))\right) \quad (2.9)$$

Equivalently,

$$\Psi(\Phi) = a \cot\left(-\frac{l_1}{b_1} \sin(\Phi)\right) \quad (2.10)$$

Denoting by Ψ_{oc} the beating angle that corresponds to Φ_o at clap's initiation from the last equation we get:

$$\Psi_{oc} = a \cot\left(-\frac{l_1}{b_1} \sin(\Phi_o)\right) \quad (2.11)$$

As already indicated crucial is the calculation of the time at which clap begins. This is accomplished by solving equation (2.4) for time when Ψ is equal to Ψ_{oc} . Doing so we acquire: $t_c = \frac{1}{\omega} a \sin\left(\frac{\Psi_{oc} - \Psi_m}{\Psi_A}\right)$. Finally, in absolute time scale in the period this

happens after half the period, hence

$$t_c = \frac{T}{2} + \frac{1}{\omega} \left| a \sin\left(\frac{\Psi_{oc} - \Psi_m}{\Psi_A}\right) \right| \quad (2.12)$$

At the end of clap, fling starts following the same exact principle, letting to point B (Bottom) on the plane of symmetry on lines d_2 to move downward with a simultaneous rotation of the two wings, only this time the geometric quantities involved are b_2 , d_2 , a_2 and c_2 respectively to clap, resulting in the following equations:

$$\alpha_2 = a \tan\left(\frac{l_2}{b_2}\right) \quad (2.13)$$

and

$$c_2 = l_2 \sin(\Phi) = -b_2 \tan\left(\Psi + \frac{\pi}{2}\right) \Rightarrow l_2 \sin(\Phi) = -b_2 \cot(\Psi) \quad (2.14)$$

We find the geometric relation between angle of attack and beating angle for the fling phase as:

$$\Phi(\Psi(t)) = a \sin\left(-\frac{b_2}{l_2} \cot(\Psi(t))\right) \quad (2.15)$$

Equivalently,

$$\Psi(\Phi) = a \cot\left(-\frac{l_2}{b_2} \sin(\Phi)\right) \quad (2.16)$$

Denoting by Ψ_{of} the beating angle that corresponds to $-\Phi_o$ at the end of fling from the last equation we get:

$$\Psi_{of} = a \cot\left(\frac{l_2}{b_2} \sin(\Phi_o)\right) \quad (2.17)$$

Also in a similar way to calculating t_c we calculate t_f , the time that coincides with the end of fling phase. This is accomplished by solving equation (2.24) for time when

Ψ is equal to Ψ_{of} . Doing so we acquire: $t_f = \frac{1}{\omega} a \sin\left(\frac{\Psi_{of} - \Psi_m}{\Psi_A}\right)$.

Finally, in absolute time scale in the period this takes place before the end of the period, hence:

$$t_f = T - \frac{1}{\omega} \left| a \sin\left(\frac{\Psi_{of} - \Psi_m}{\Psi_A}\right) \right| \quad (2.18)$$

For the given wing geometrical parameters $\alpha_1, \alpha_2, b_1, b_2, c_1, c_2, (d_1, d_2)$ are fixed. This means that we can alter the duration of fling and clap phases by changing Ψ_m, Ψ_A and Φ_o . For all our numerical simulations we keep fixed Φ_o and Ψ_m and Ψ_A . We note that Ψ_A is related to the motion's frequency through the Reynolds number by the definition of maximum velocity as shown by equation (2.19),

$$U_{\max} = x \cdot \dot{\Psi}_{\max} = 0.65l \cdot \omega \Psi_A \Rightarrow \omega = \frac{1}{0.65 \Psi_A} \quad (2.19)$$

As seen from Figures 2.7 and 2.8, with the prescribed kinematics used, for $\Psi_m = -150^\circ, \Psi_A = 30^\circ$ and $\Phi_o = 45^\circ$ the total clap and fling time extends to 35.22% of the whole wing motion period and breaks down in 13.45% for the clap and 21.77% for the fling phase. The above procedure was coded into a MATLAB program producing two files containing positions, velocities and accelerations for angle of attack and stroke angle, providing the necessary input for the computations. In Figure 2.9, successive frames from the resulting wing motion are shown.

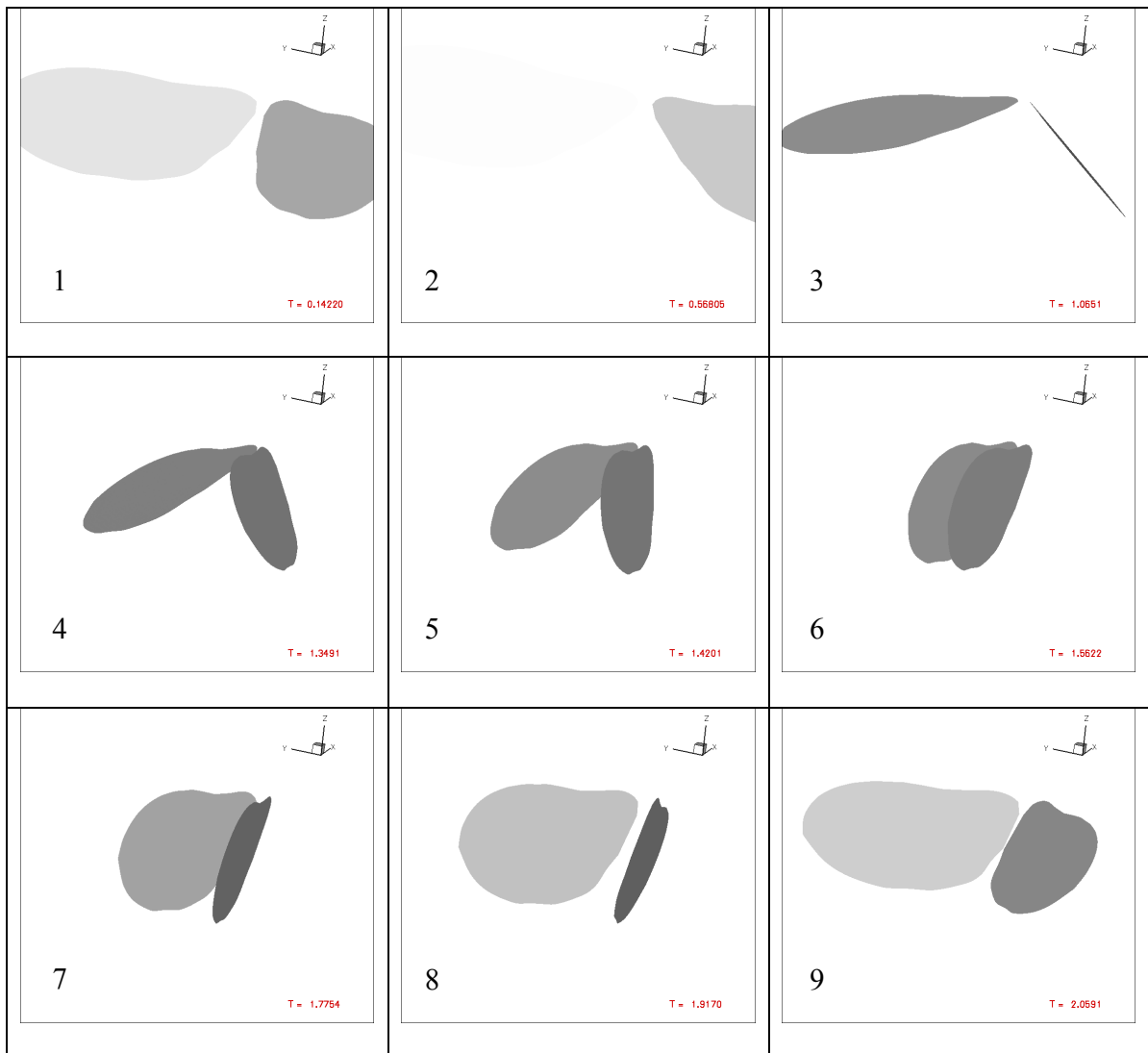


Figure 2.9 Geometry of kinematic sequence for clap and fling. The 9 instances show correspond from left to right in each row to: 1. right after the start of the motion. 2. $0.25T$ 3. $0.5T$ 4. right before the start of clap 5-6 within clap 7-9 within fling. On each graph on the lower right, the instant to which the frame corresponds to is indicated. $T=2.1384$

Chapter 3: Results and analysis

In this chapter we are going to investigate the effects of the chosen parameters on the forces acting on the wings throughout a clap and fling. Furthermore, we will investigate the relation of these forces with the resulting flow patterns.

3.1 Force distribution

In Figure 3.1, the lift coefficient is shown for case I for the first period T of the motion. The times of clap's phase start and fling's phase end are denoted as t_c and t_f , respectively, while the time at which change from the clap to the fling phase takes place, is $0.75T$. At the onset of the motion the lift coefficient starts around the value of one and then as the wings move apart it decreases reaching a local negative minimum at the instant at which the wings reach their far end separation ($t=0.25T$). The reverse of the motion is followed by a gradual increase of lift which then remains almost constant as the wings move back to their original position but with opposite moving direction, at $t=0.5T$. At that time the wings come further closer with constant angle of attack. This time interval is characterized by a substantial increase of lift starting around $0.58T$. Continuously approaching, the wings enter the clap phase at $t=0.61T$ and very soon after that the lift force reaches a value of 2.8744 for the two-wing model and 2.4023 for a single wing. These are also the peak values for the entire period. Clap continues until the 75% of the period with an abrupt loss of lift which acquires for a short time takes on negative values as the rotating wings become practically vertical in their closest position. Fling is very rich in terms of changes in

lift generation and loss. It exhibits initially another rise in lift production only very moderate this time with peak values of 0.0337 for the two wings and 0.0105 for the single one, while its later stages are characterized by a lift drop and yet another enhancement interval just prior to the completion of the period. Increasing the separation angle from $\Theta = 2^\circ$ to $\Theta = 10^\circ$ as it is expected, attenuates the interaction effect of the two wings resulting in a drop in the lift force produced as indicated in Figure 3.2.

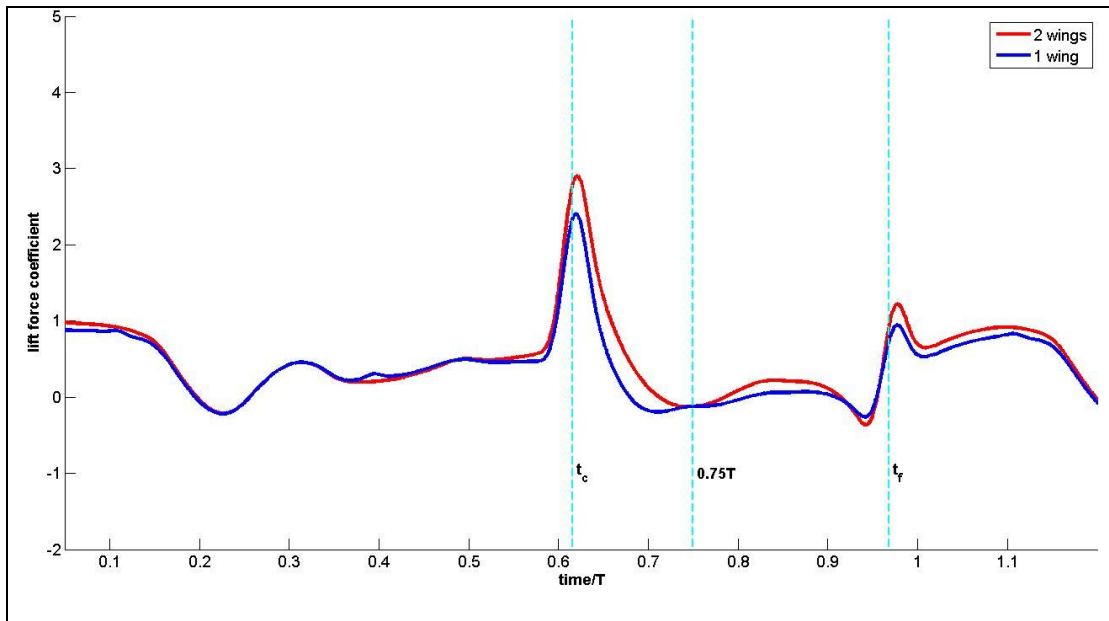
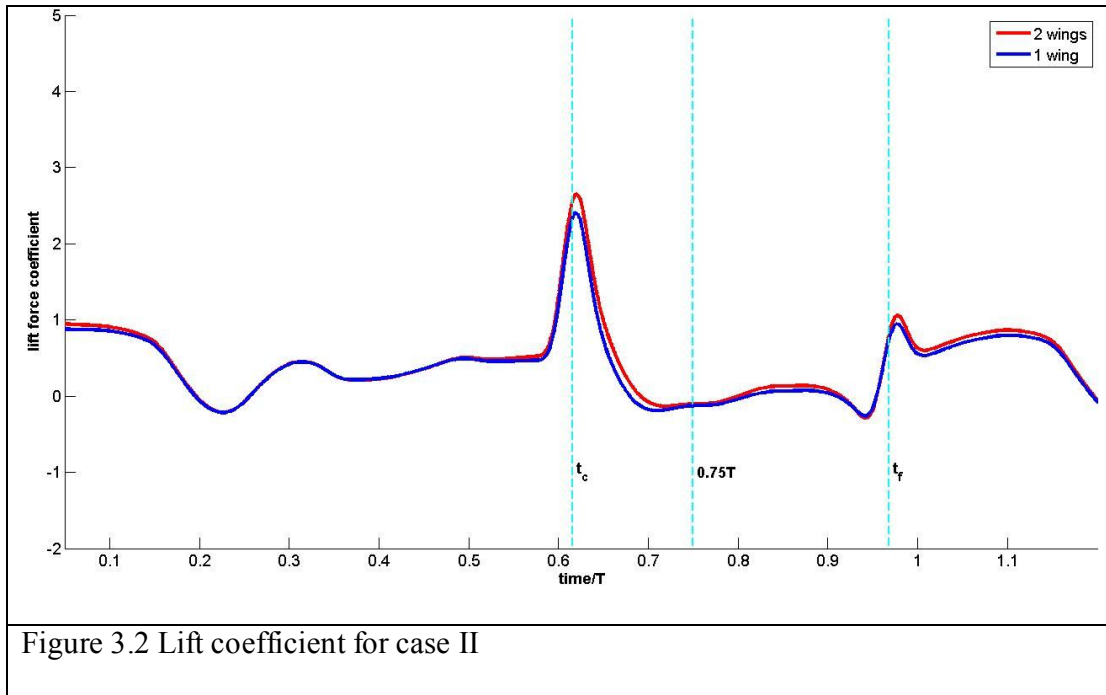


Figure 3.1 Lift coefficient for case I

Thus, a peak value of 2.6489 is achieved for two wings and 2.4021 for one wing during clap, while during fling the corresponding peak values are 0.0208 and 0.0112. The general trends however of the variation of the lift force over time for both one and two wings are along the same lines as for case I.



In Figure 3.3 the effect of the Reynolds number for $\Theta = 2^\circ$ is shown. It is apparent that an even larger attenuation of the lift force is being experienced for both one and two wing cases. The peak values during clap are 1.9858 and 1.6887 respectively. However, during fling the peak values are 0.0336 and 0.0172, i.e. higher than the case II values for the same time interval.

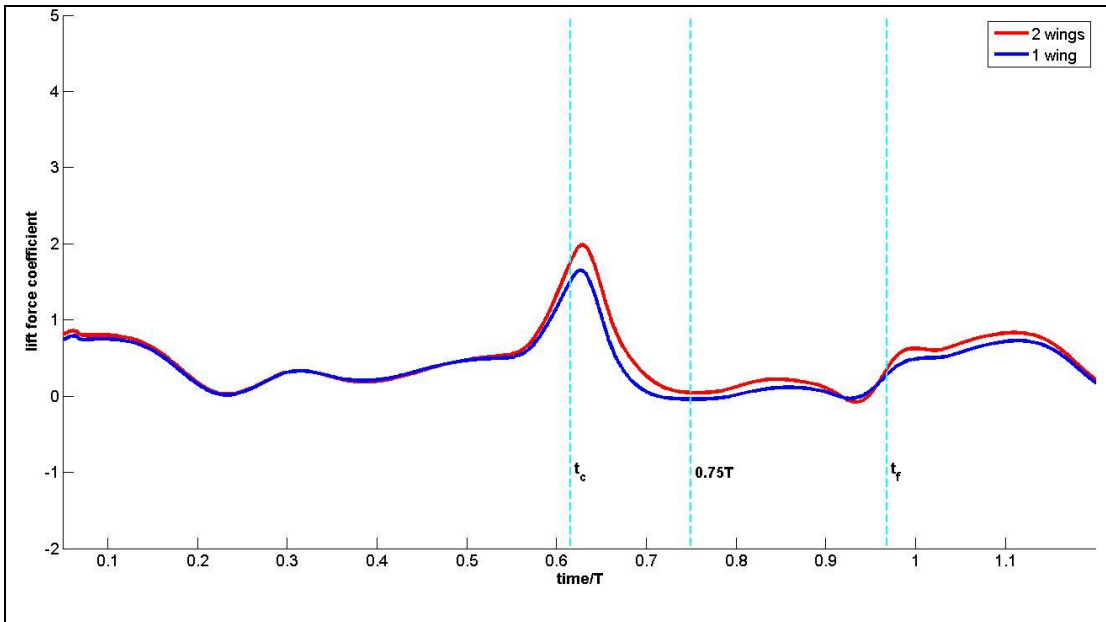


Figure 3.3 Lift coefficient for case III

To summarize, in all cases the lift produced during clap, (initiated around $0.6T$ and ending at $0.75T$) is enhanced.

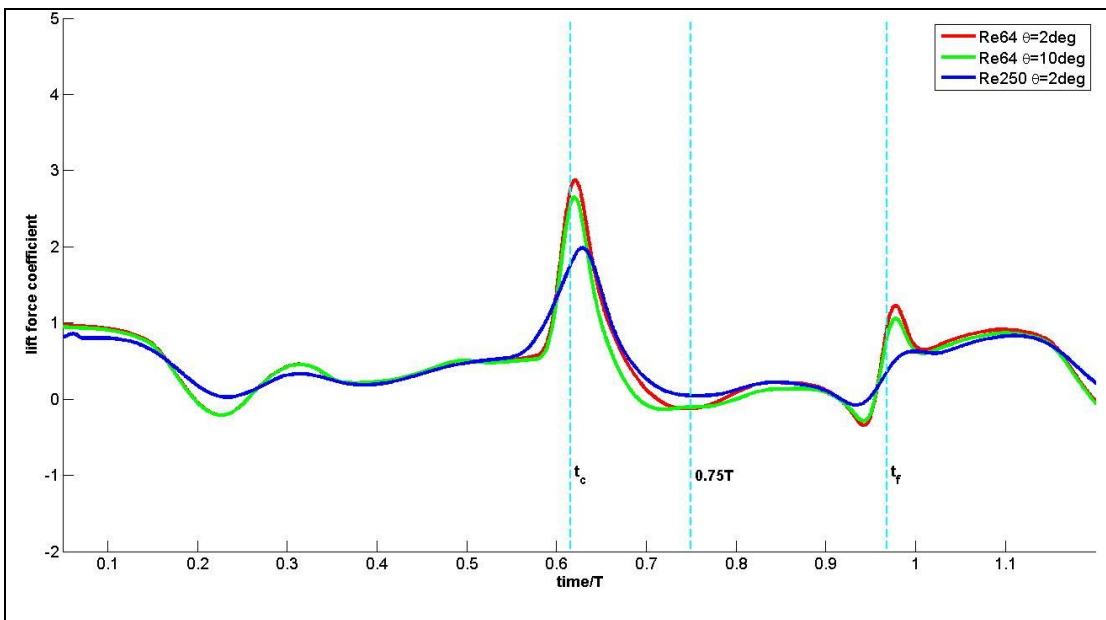


Figure 3.4 Lift coefficient with Reynolds number and separation angle as parameters for setup I

The percentage increase of the peak is 19.65%, 8.70% and 17.59% for cases I II and III when compared to the corresponding one wing case.

In Figure 3.4 the three two-wing cases are directly compared. It is clear that for two wings, while for the variation in Θ C_L does not differ significantly, the increase of Reynolds number drastically attenuates the interference effect of the two wings in terms of the highest values achieved. However as will be shown, the overall lift produced is more enhanced for case III than for case II. The higher Reynolds number case also exhibits less abrupt changes throughout the whole period. It is worth mentioning that in three specific time intervals, i.e. at $0.25T$, at $0.75T$ (just right before and after the transition from clap to fling) and at about $0.93T$, C_L values for the $Re=250$ exceed those of the other two cases. In the case of single wing setups for the same parametric space (see Figure 3.5), the traces of the two $Re=64$ cases are practically indistinguishable while their difference from $Re=250$ is along the same lines for two wings.

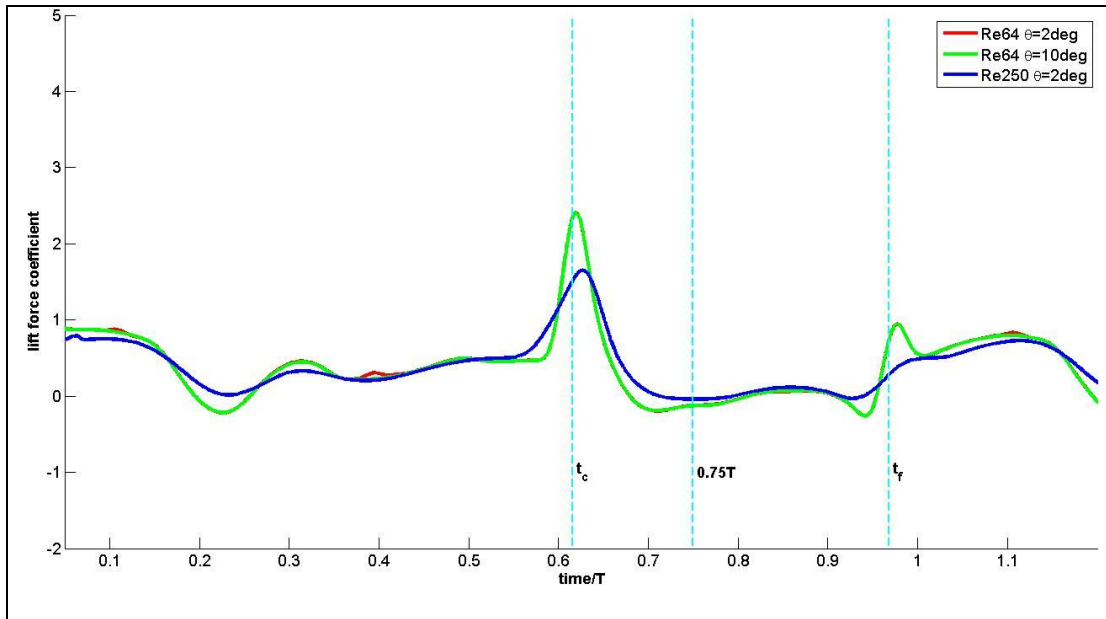


Figure 3.5 Lift coefficient with Reynolds number and separation angle as parameters for setup II

To estimate more in depth the effect of clap and fling for our parametric space, we calculate the integral of lift coefficients over different phases, corresponding to impulse, using one of the available numerical methods, as for example the trapezoidal rule. By doing so we can then identify the contribution of each part to the total lift production. According to these results, the 22%, 18% and 24% of the lift is produced during clap for setup I and the three different cases. During fling the corresponding percentages are 3.2%, 1.5% and 2.3%. It is thus further established that lift both during clap and fling is less affected by the change in the Reynolds number, than change in the separation angle.

		Re 64, $\Theta = 2^\circ$	Re 64, $\Theta = 10^\circ$	Re 250, $\Theta = 2^\circ$
Integral over one period	2 wings	0.1538	0.1380	0.1394
	1 wing	0.1229	0.1218	0.1173
	Exact diff.	0.0309	0.0162	0.0221
	% diff.	25.18	13.28	18.84
Integral over clap	2 wings	0.0338	0.0252	0.0337
	1 wing	0.0184	0.0185	0.0228
Integral over fling	2 wings	0.0050	0.0020	0.0079
	1 wing	-0.0006	-0.0006	0.0034
Integral clap-fling	2 wings	0.0388	0.0272	0.0416
	1 wing	0.0178	0.0179	0.0262

Table 3.1 Integrals for $C_L = f(t)$ for different time intervals within a period with trapezoidal rule.

By integrating the curve over one period we can determine the mean lift \bar{C}_L coefficient. In addition, calculating the integral of lift coefficient, during clap only, fling only and clap and fling altogether and averaging over the corresponding time interval we can make find the relative contribution of its one to the total lift production. These results are summarized in Tables 4 and 5, where \bar{C}_L over the whole period is enhanced a 25% for case I, 13% for case II and 19% for case III.

		Re 64, $\Theta = 2^\circ$	Re 64, $\Theta = 10^\circ$	Re 250, $\Theta = 2^\circ$
\bar{C}_L over one period	2 wings	0.0719	0.0645	0.0652
	1 wing	0.0575	0.0570	0.0548
	Exact diff.	0.0145	0.0076	0.0103
	% diff.	25.18	13.2842	18.84
\bar{C}_L over clap	2 wings	0.1175	0.0876	0.1172
	1 wing	0.0640	0.0643	0.0793
\bar{C}_L over fling	2 wings	0.0108	0.0042	0.0169
	1 wing	-0.0013	-0.0012	0.0072
\bar{C}_L over fling	2 wings	0.0515	0.0361	0.0552
	1 wing	0.0236	0.0238	0.0347
Table 3.2 Average lift coefficient for different phases indicating the differences between one and two wings setups.				

Moving along our investigation of the forces, we turn our attention to the force in the longitudinal (axial) direction. The graph of the time evolution of this force for the first period is shown in Figure 3.6 for both one and two wing configurations. It is apparent that there are 3 local maximums for setup I, one after the reversal in beating angle direction at $0.25T$, at the onset of clap and another one during fling at about $0.93T$. The lowest values of C_x are acquired at $t=0.15T$ on the way of the wings to their maximum distance and then prior to the onset of clap. Another significant drop is also observed around $t=0.81T$. For setup II another pair of

minimum and maximum is observed at $t=0.7T$ and at $t=0.75T$ respectively. The lowest values acquired for both setups are around -2 while the highest around 3.3 but the curves remain negative for more than 50% of the period. The difference between setups I and II for this case regarding the integral of the x force component, and hence the difference in the mean force in the x adirection, is still positive but bigger for the one wing case. The percentage difference in absolute number is 21.5% .

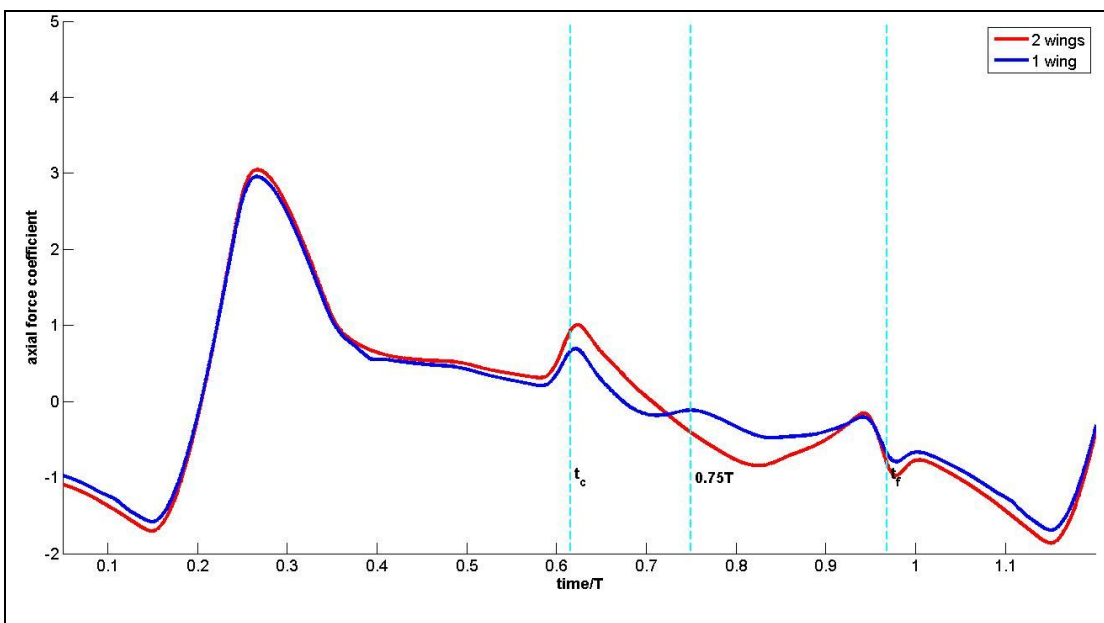


Figure 3.6 Axial force coefficient for case I

In Figure 3.7 the comparison for two wings setup is being made for our parametric space. The trend shown there is that the second case of our runs prior to the clap appears to provide overall more enhancement in C_x and the two $Re=64$ cases the same over the $Re=250$ one, but only after $0.25T$. During clap, after local maximum being realized, a precipitous drop starts, which continues through fling, reaching a minimum around $0.81T$. In this loss of C_x the case with higher angular separation

exhibits the lowest (highest negative) values compared to the other two cases. As in the case of lift, the curve of the Re=250 is smoother. The mean value of C_x denoted by \bar{C}_x is for case I 0.0119, for case II 0.01 and for case III 0.0117 implying that as in the case of lift, case II had a more serious effect on the force in the x direction than case III.

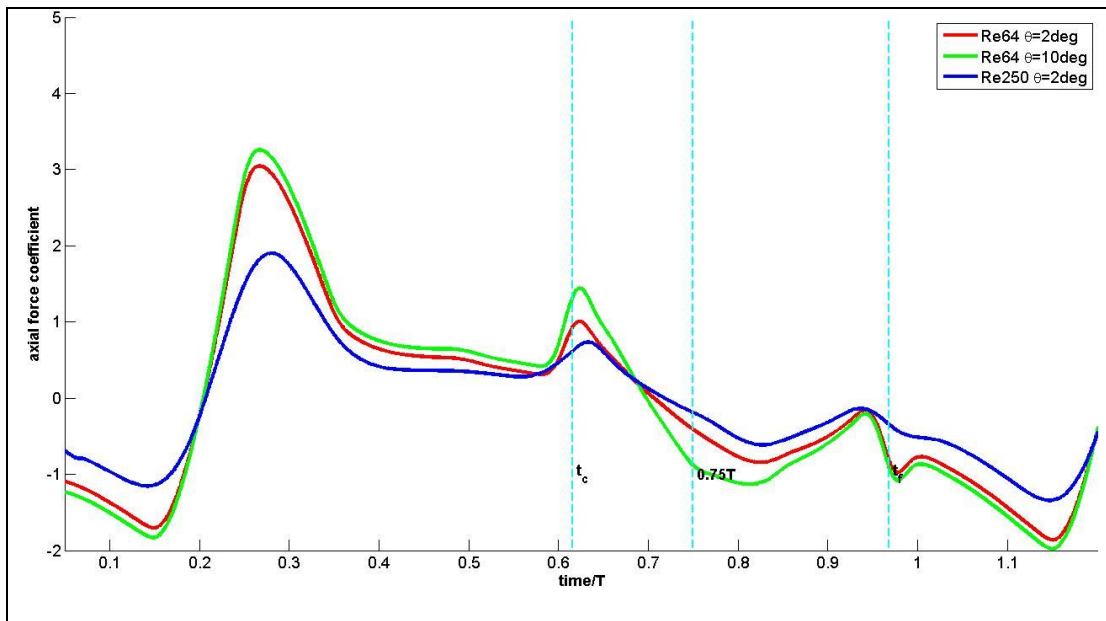
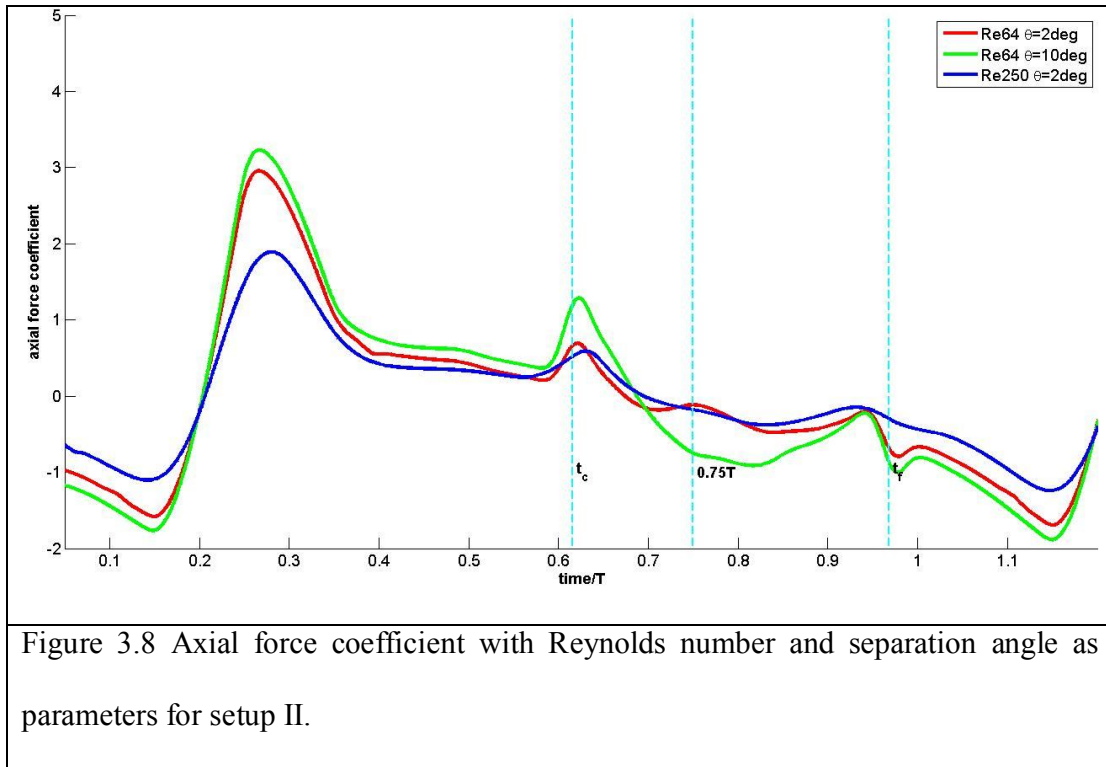


Figure 3.7 Axial force coefficient with Reynolds number and separation angle as parameters for setup I.

Interestingly, for the one wing setup although the same as above trends are in general demonstrated, at $t=0.75T$ the first case of our runs demonstrates a maximum climbing higher even from the Re=250 case as seen in Figure 3.8.



The change in force coefficient of the y component of the forces on the wings is shown on Figure 3.9 for the base case comparing one to two wings setups. The general idea in this Figure is that the force initially stays constant up to $t=0.16T$ and then rapidly declines reaching a minimum at $t=0.25T$ to be followed by another time interval of almost constant value until just prior to the onset of clap. Entering the clap phase is characterized by a fast drop down to -3.572 for the one wing and to -4.355 for the two wings setup. There follows a spectacular increase for setup I up to 7.67 . Setup II exhibits a still impressive yet not as high as a setup I increase up to 4.133 and a little sooner. This main characteristic is going through to the fling phase, followed by yet another precipitous loss of force and a local minimum around $t=0.94T$ with the two curves being almost on top of each other. A $C_y = 0.5$ for setup I and a $C_y = 1.13$ for setup II are accomplished. Finally, fling appears to be giving a substantial push to

the y force, whose coefficient rises up to 1.285 and to 1.6 for one and two wings respectively.

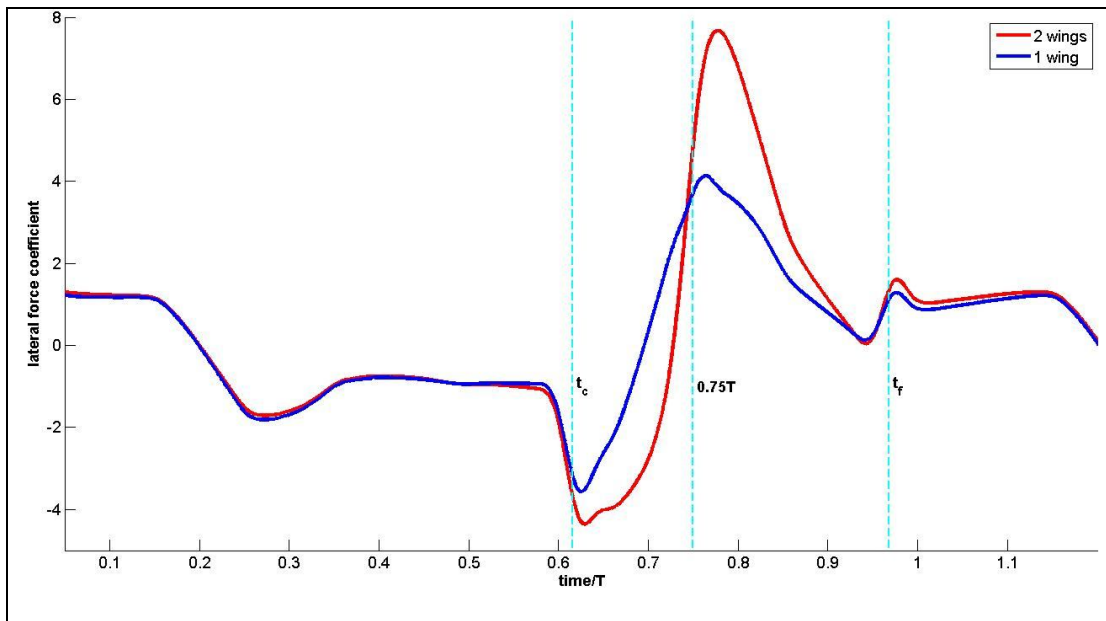


Figure 3.9 Lateral force coefficient for case I

One of the interesting features of the y force component's figure to be pointed out is that from $t=0.57T$ to $t=0.7T$ the (negative) y force of setup I is bigger in absolute sense than the force produced by setup II, but from $t=0.7T$ to $t=0.74T$ the trend is reversed. The average lateral force coefficient denoted by \bar{C}_y is calculated with the methodology previously described for x and z forces' coefficient to be 0.0344 for setup I and 0.0214 for setup II, i.e a 61.2% difference. The corresponding percentages for cases II and III are 34.1% and 121% between setups I and II. This once more verifies that a general force loss is being imposed on our system when switching from the case I to case II, but also that is not the case for the higher Reynolds number.

Comparing in Figure 3.10 the lateral force coefficients for setup I and all 3 cases under study, it is clear that for about the whole cycle the force produced by the case I is in absolute sense higher than these of the other two cases. The other two cases antagonize each other with different time regimes of dominance for each and exhibit more or less the same trends with the exception of the substantial force's increase at the end of fling. This fact results in a higher mean lateral force coefficient for case II, 0.0319 in comparison to 0.0235 for case III.

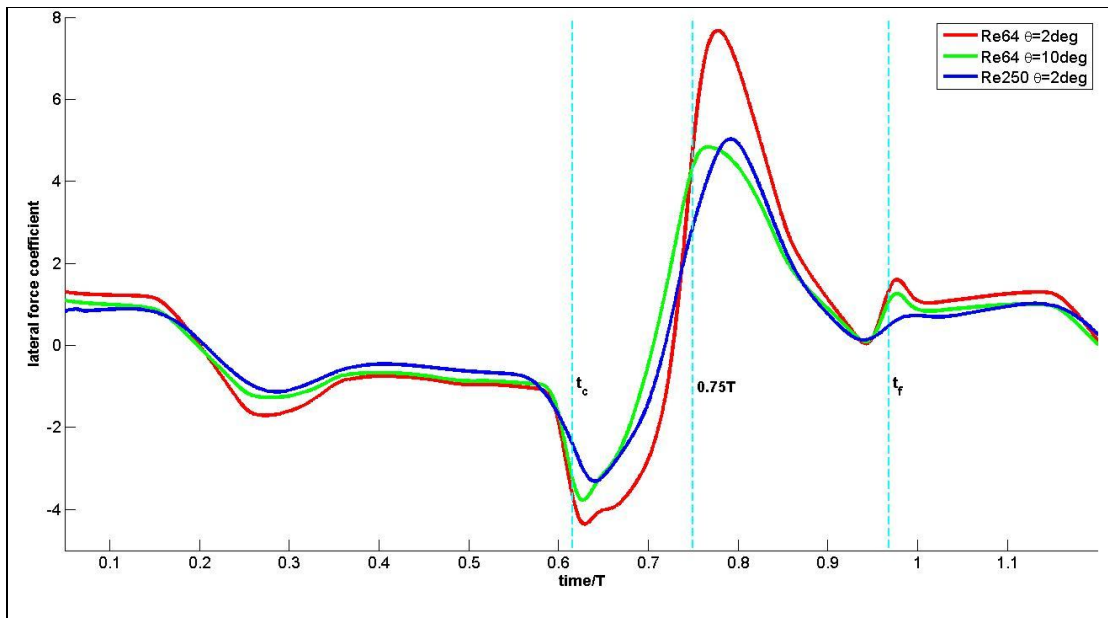


Figure 3.10 Lateral force coefficient with Reynolds number and separation angle as parameters for setup I.

3.2 Qualitative Description of Flow Field

In this section we investigate the instantaneous dynamics of the flow and their relation to the forces described above. In Figure 3.11 pressure contours for case I at different instances within the first period for a slice vertical to the stroke plane at 65% of wing's length are shown. As the two wings are moving away from each other low pressure develops in the area between the wings and high on the outside. As the wings then begin to approach each other, pressure at the area between them becomes significantly higher than the one of the fluid surrounding the wings reaching a maximum at the end of clap. This behavior corresponds to the rise in lift and lateral force previously shown. The difference in the trends of the two force's components is that at the onset of clap the projection of surface of the wing in the z axis is high but decreasing while the effective surface on the y axis constantly increases during clap. This explains why lift force acquires its overall the period maximum sort after the initiation of clap while the lateral force keeps well getting higher values. By inspection of the pressure contour figures corresponding to the fling (9-12) we see that at the start of fling the pressure field is once more reversed, i.e. the pressure of the surrounding fluid becomes positive and the one of the "interior" negative. This explains the drop of the lateral force right after we enter the fling phase. The production of new, stronger than before, leading edge vortex couple is dominating the initial phase of fling.

In Figure 3.12 x vorticity for case I is shown. The contours shown are 2-color contours at different instances within the first period for two vertical to the stroke plane slices at 30% and 65% of wing's length. In frames 3-7 covering the approaching of the wings time interval, vorticity is being generated on both the leading and the trailing edge resulting in the formation of two new pairs of vortices. By inspection of this figure and with the movie made for the flow by successive frames as the ones in Figure 3.12, we conclude that vortex separation and subsequent shedding into the wake, is a characteristic of the flow at the end of clap and the start of fling. As supportive to this statement comes Figure 3.13 of Q iso-surface, frames 8-10. In this figure it is indicated that by the end of clap the leading and trailing edge vortex on each wing appear to be linked with one another and separate from the wing.

As far as the results for the rest cases and setups are concerned, the relevant figures of the flow field are at Appendix B. Summarizing the trends shown there we can say that the attenuation of the interference effect is obvious in terms of pressure and ω_x . In the higher Reynolds number case the separation of the leading edge vortex appear to be more prominent than the other two cases, while in cases I and II, diffusion of vorticity is happening more quickly.

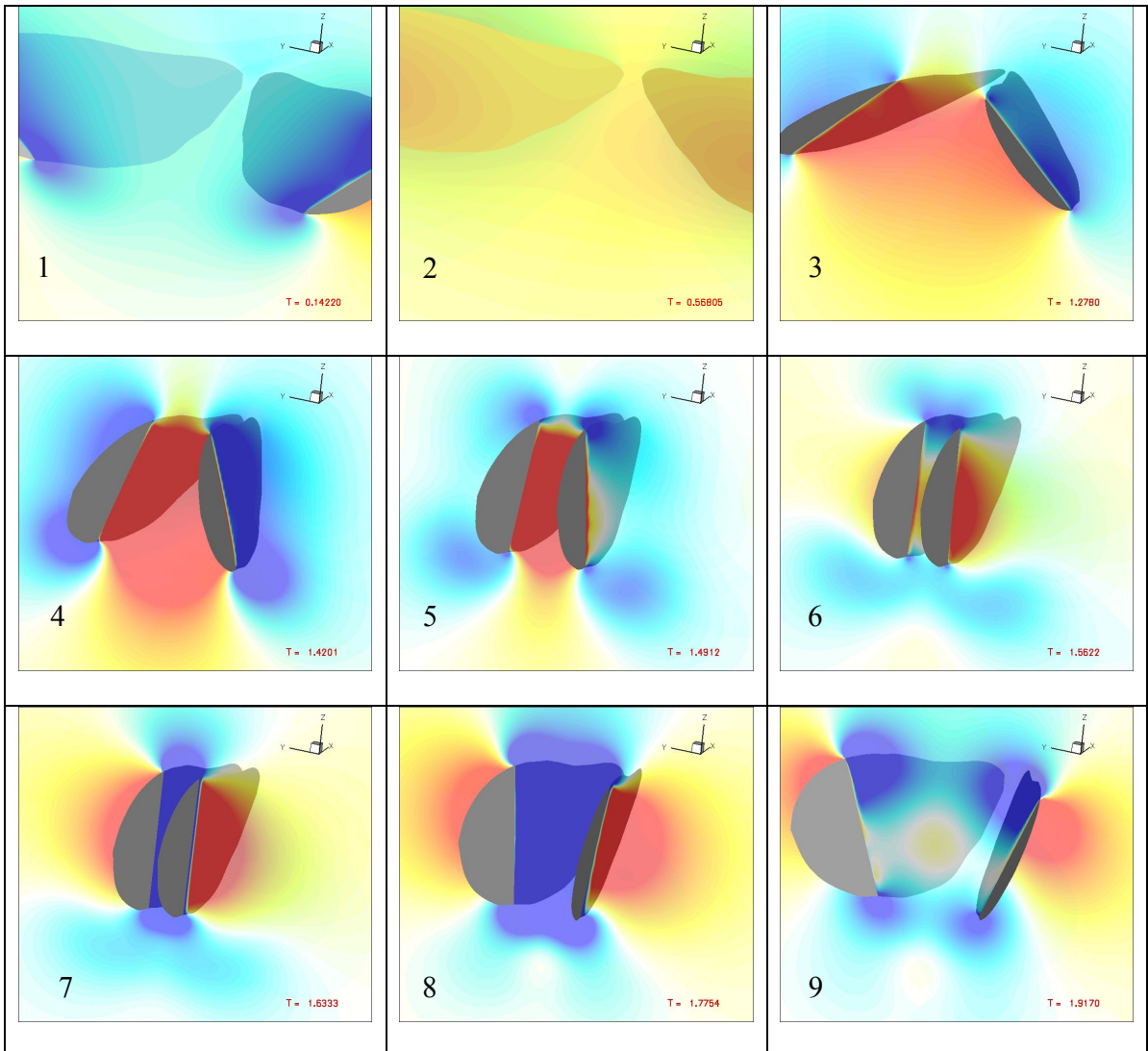


Figure 3.11 Pressure contours for case I setup I at different instances within the first period for a slice vertical to the stroke plane at 65% of wing's length. Blue to red for lower to higher values from -0.5 to 0.5 and 61 contour levels. The 9 instances shown correspond from left to right in each row to: 1. right after the start of the motion. 2. $0.25T$ 3. right before the start of clap 4-5 within clap 6-9 within fling. On each graph on the lower right the instant at which the frame corresponds is indicated. $T=2.1384$

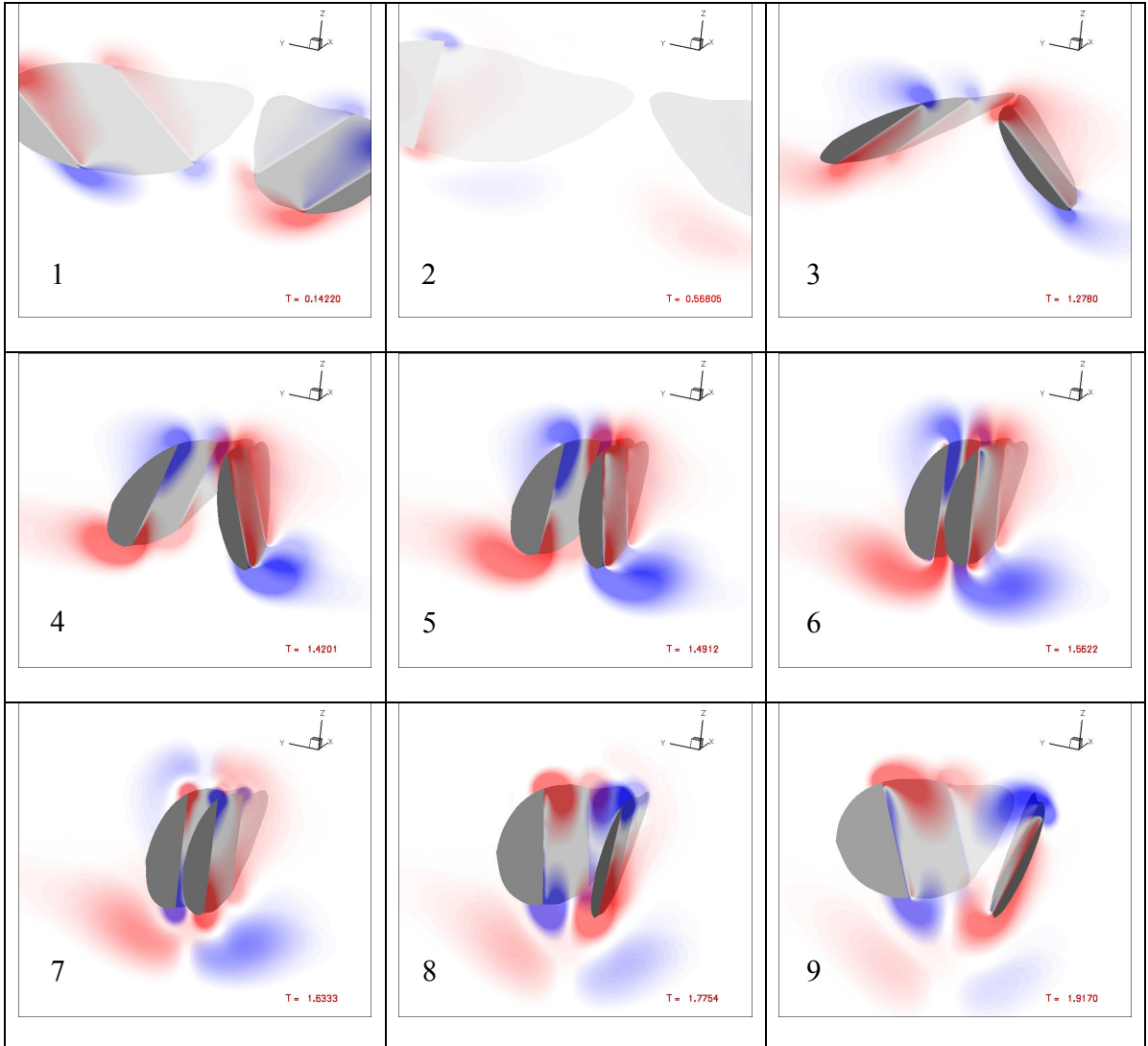


Figure 3.12. ω_x 2-color contours for case I setup I at different instances within the first period for two vertical to the stroke plane slices at 30% and 65% of wing's length. Blue to red for lower to higher values from -12 to 12 and 55 contour levels. The 9 instances shown correspond from left to right in each row to: 1. right after the start of the motion. 2. $0.25T$ 3. right before the start of clap 4-5 within clap 6-9 within fling. On each graph on the lower right the instant at which the frame corresponds is indicated. $T=2.1384$

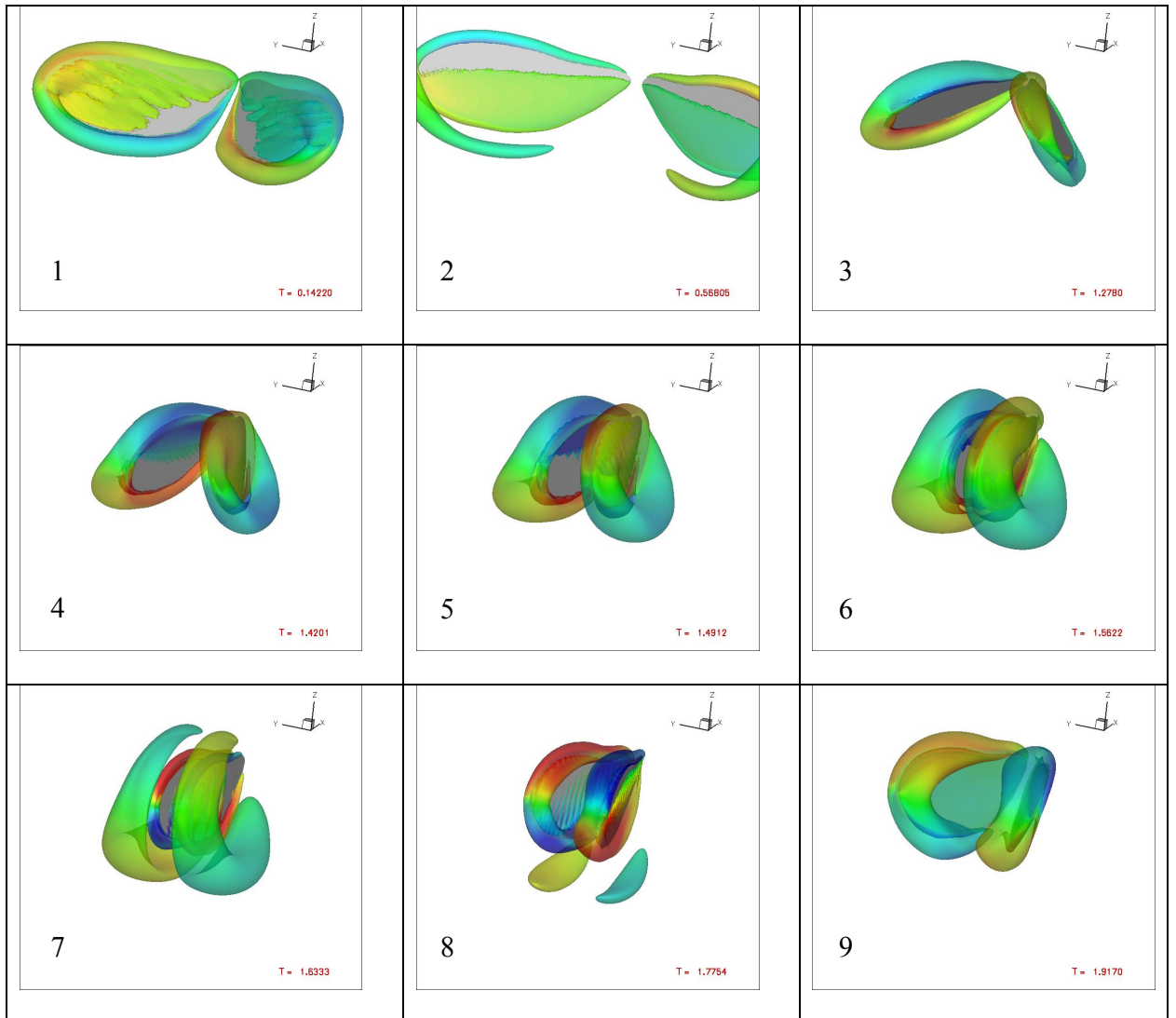


Figure 3.13. $Q=5$ iso-surfaces colored by vorticity in x for case I setup I at different instances within the first period. Blue to red for lower to higher values from -12 to 12 and 55 contour levels. The 9 instances shown correspond from left to right in each row to: 1. right after the start of the motion. 2. $0.25T$ 3. right before the start of clap 4-5 within clap 6-9 within fling. On each graph on the lower right the instant at which the frame corresponds is indicated. $T=2.1384$

Chapter 4 Summary-Conclusions

In the present study we developed prescribed kinematics that mimic the wing motion of insects that perform clap and fling. We then performed a series of computations using a high-fidelity viscous Navier-Stokes solver, to investigate how the aerodynamic forces are generated and if clap and fling results in significant enhancements compared to single wing. The effects of the separation angle between the two wings prior to clap and the Reynolds number have been investigated in detail.

The main findings included lift enhancement over a period for clap and fling by 25% for case I ($Re=64$, $\alpha=2^\circ$), 13.28% for case II ($Re=64$, $\alpha=10^\circ$), and 18.84 for case III ($Re=250$, $\alpha=2^\circ$). The ‘clap’ part of the flapping cycle represents 20% of the total lift, while fling represents 1-3% for all the above cases. Hence, for the set of kinematics considered in the present work, clap appears to be far more important than fling. This result is in agreement with observations by Maxworthy [48] but contradicts the results of Lehmann *et al.* [43]. In the latter work, however, the wings were not stopping when reaching the vertical position but continued to rotate until the wings’ tips met. The kinematic in the former case are more similar to the ones we used. It must be noted though, that no previous work done so far incorporated an active change in the angle of attack as ours.

The effect of separation angle on the production of x and z forces, appears to be more detrimental comparing to the effect of Reynolds number. It is thus further

established that lift both during clap and fling is less affected by the change in the Reynolds number, than change in the separation angle. These features substantiate the fact that clap and fling is mainly affected, as suspected, by the interaction of the two wings. The effect of Reynolds number is more pronounced than the separation angle for the lateral force but the symmetrical forces on the system of the two wings eliminate each other.

The study of the flow field reveals that the pressure distribution throughout the cycle can be associated with the time evolution of the forces recorded. Furthermore the main characteristic of the field is the separation and shedding of leading edge vortex as we transition from clap to fling.

Future work based on the above results could:

- i) investigate if the gains in lift are sustained after several flapping cycles and how much they depend on initial conditions. In the present work we considered only one set of initial conditions;
- ii) explore what happens at much lower Reynolds numbers (i.e. $Re \sim 2$) which are representative small insects performing clap and fling in nature
- iii) extend the kinematical parametric regime to examine the effects of:
 - a. the distance between the hinges
 - b. frequency of the motion
 - c. timing and duration of clap and fling phases by altering the geometric quantities that affect them, i.e. the amplitude Ψ_A of the

motion (which is related to the frequency through (2.19)), the axes of wingbeat symmetry defined by Ψ_m , and the constant angle of attack at the onset of clap Φ_o .

The above study should also be accompanied by a detailed examination of the instantaneous dynamics of the flow and how these are related to the generation of aerodynamics forces.

Appendix A

After the notation used in Figure 2.1 we present the detailed transformation sequences of chapter 2 [3].

Rigid Body 1

The fixed inertial frame used is termed as N $(\hat{n}_1, \hat{n}_2, \hat{n}_3)$. Going from the inertial frame to frame E following the thorax motion, we assume an 180° rotation about \hat{n}_1 such that the resulting coordinate system $(\hat{e}_1, \hat{e}_2, \hat{e}_3)$ is oriented with \hat{e}_1 parallel to the longitudinal axis of the insect, \hat{e}_2 in the lateral direction pointing towards the right wing and \hat{e}_3 perpendicular to the plane of \hat{e}_1 and \hat{e}_2 with its positives from the dorsal to the ventral. By employing the standard practice of aerodynamics for describing the motion of RB1 we perform a 3-2-1 Eulerian angles sequence. First the 3 rotation is resulting in coordinate system \hat{e}' with an angle ψ , then the 2 in \hat{e}'' with an angle θ and the 1 in $\hat{e}''' \equiv \hat{b}$ with an angle φ . This finally results in reference frame B $(\hat{b}_1, \hat{b}_2, \hat{b}_3)$ local on RB1. The convention followed to describe the transformation matrices is given by two capital letters denoting first the original and then the final frame. Thus the transformation matrix from the inertial frame to E is denoted by T_{NE} . Here follow the transformation matrices of the so-far mentioned rotations:

$$\begin{Bmatrix} \hat{e}_1 \\ \hat{e}_2 \\ \hat{e}_3 \end{Bmatrix} = \begin{bmatrix} 1 & 0 & 0 \\ 0 & -1 & 0 \\ 0 & 0 & -1 \end{bmatrix} \cdot \begin{Bmatrix} \hat{n}_1 \\ \hat{n}_2 \\ \hat{n}_3 \end{Bmatrix}, \text{ Hence } T_{NE} = \begin{bmatrix} 1 & 0 & 0 \\ 0 & -1 & 0 \\ 0 & 0 & -1 \end{bmatrix}.$$

Likewise,

$$T_{EE'} = \begin{bmatrix} \cos \psi & \sin \psi & 0 \\ -\sin \psi & \cos \psi & 0 \\ 0 & 0 & 1 \end{bmatrix}, T_{E'E''} = \begin{bmatrix} \cos \theta & 0 & \sin \theta \\ 0 & 1 & 0 \\ -\sin \theta & 0 & \cos \theta \end{bmatrix}, T_{E''B} = \begin{bmatrix} 1 & 0 & 0 \\ 0 & \cos \phi & \sin \phi \\ 0 & -\sin \phi & \cos \phi \end{bmatrix}.$$

The transformation matrix T_{NB} describing the relation between unit vectors of frames

B and N : $\{\hat{b}\} = T_{E''B} \cdot T_{E'E''} \cdot T_{EE'} \cdot T_{NE} \cdot \{\hat{n}\}$ is obviously given as:

$T_{NB} = T_{E''B} \cdot T_{E'E''} \cdot T_{EE'} \cdot T_{NE}$. After performing the matrices' multiplications we get,

$$T_{NB} = \begin{bmatrix} c\theta c\psi & -c\theta s\psi & s\theta \\ s\phi s\theta c\psi - c\phi s\psi & -s\phi s\theta s\psi - c\phi c\psi & -s\phi c\theta \\ c\phi s\theta c\psi + s\phi s\psi & -c\phi s\theta s\psi + s\phi c\psi & -c\phi c\theta \end{bmatrix} \quad (A.1).$$

As in the last equation form here after we will use for more compact forms of our formulas $c(\)$ instead of $\cos(\)$ and $s(\)$ instead of $\sin(\)$.

Then the velocities and accelerations can be computed. The angular velocity of the thorax as known by dynamics is the vector sum of the angular velocities of each intermediate rotation. Thus:

$${}^N\omega^B = \dot{\psi}\hat{e}_3 + \dot{\theta}\hat{e}'_2 + \dot{\phi}\hat{e}''_1, \text{ where } (\dot{\ }) \equiv \frac{\partial}{\partial t}.$$

Again the convention is that in the index in the upper left corner accounts for the starting frame while the one at the right corner for the concluding one. We need to express this angular velocity in the B frame, i.e we need to get ${}^N\omega_B^B$ where the lower right index is understood to describe the frame with respect to which we are currently expressing the particular vector. Making advantage of the afore-mentioned rotation matrices we get:

$$\left\{{}^N\omega_B^B\right\}^T = \left\{\hat{b}\right\}^T \cdot \begin{bmatrix} -s\theta & 0 & 1 \\ s\phi c\theta & c\phi & 0 \\ c\phi c\theta & -s\phi & 0 \end{bmatrix} \cdot \begin{Bmatrix} \dot{\psi} \\ \dot{\theta} \\ \dot{\phi} \end{Bmatrix} \quad (A.2)$$

In the above expression the presence of the unit vector of B is redundant since we have already declared that the angular velocity is expressed in this reference frame. However we keep it to more lively demonstrate the following differentiations.

$$\text{We set } {}^N M_B^B(\psi(t), \theta(t), \phi(t)) = \begin{bmatrix} -s\theta & 0 & 1 \\ s\phi c\theta & c\phi & 0 \\ c\phi c\theta & -s\phi & 0 \end{bmatrix} \text{ and } {}^N \Omega_B^B = \begin{Bmatrix} \dot{\psi} \\ \dot{\theta} \\ \dot{\phi} \end{Bmatrix}$$

The angular acceleration is given by: ${}^N\alpha_B^B = \frac{d}{dt} {}^N\omega_B^B$. By application of the

definition we get:

$${}^N\alpha_B^B = \frac{d}{dt} {}^N\omega_B^B = \left\{\hat{b}\right\}^T \left(\frac{d}{dt} {}^N M_B^B {}^N\Omega_B^B + \frac{d}{dt} {}^N\Omega_B^B {}^N M_B^B \right) + \left(\frac{d}{dt} \left\{\hat{b}\right\} \right)^T {}^N M_B^B {}^N\Omega_B^B \Rightarrow$$

$${}^N\alpha_B^B = \left\{\hat{b}\right\}^T \left({}^N\dot{M}_B^B {}^N\Omega_B^B + {}^N\dot{\Omega}_B^B {}^N M_B^B \right) + \left(\frac{d}{dt} \left\{\hat{b}\right\} + {}^N\omega_B^B \times \left\{\hat{b}\right\} \right)^T {}^N M_B^B {}^N\Omega_B^B \quad (A.3) \quad \Rightarrow$$

$$\left\{ {}^N \alpha_B^B \right\} = \left\{ \hat{b} \right\}^T \left\{ \begin{array}{c} -\dot{\psi} \dot{\theta} c \theta + \ddot{\phi} - \ddot{\psi} s \theta \\ \dot{\phi} \dot{\theta} s \phi + \dot{\psi} (-\dot{\theta} s \phi s \theta + \dot{\phi} c \phi c \theta) + \ddot{\theta} c \phi + \ddot{\psi} s \phi c \theta \\ -\dot{\phi} \dot{\theta} c \phi + \dot{\psi} (-\dot{\theta} c \phi s \theta - \dot{\phi} s \phi c \theta) + \ddot{\psi} c \phi c \theta \end{array} \right\} + ({}^N \omega_B^B \times \left\{ \hat{b} \right\})^T M_B^B {}^N \Omega_B^B$$

Calculation of the last term in the above formula gives:

$${}^N \omega_B^B \times \left\{ \hat{b} \right\} = \begin{bmatrix} 0 & \dot{\psi} c \theta s \phi - \dot{\theta} c \phi & -(\dot{\psi} c \theta s \phi + \dot{\theta} c \phi) \\ -(\dot{\psi} c \theta s \phi - \dot{\theta} c \phi) & 0 & -(-\dot{\psi} s \theta + \dot{\phi}) \\ \dot{\psi} c \theta s \phi + \dot{\theta} c \phi & -\dot{\psi} s \theta + \dot{\phi} & 0 \end{bmatrix} \left\{ \hat{b} \right\}$$

Rigid Body 3

The general motion of the right wing fixed on the body of our insect model at point R is given by the following kinematical sequence:

$$\hat{b} \xrightarrow[\hat{b}_3]{90^\circ} \hat{b}'_r \xrightarrow[\hat{b}'_{r1}]{90^\circ} \hat{b}''_r \xrightarrow[\hat{b}''_{r1}]{\beta_3} \hat{b}'''_r \xrightarrow[3-2-1]{} \hat{r}$$

Angle β_3 describes the stroke plane variance with respect to the \hat{b}''_{r1} axis.

The corresponding transformation matrices are:

$$T_{B'_r B} = \begin{bmatrix} 0 & 1 & 0 \\ -1 & 0 & 0 \\ 0 & 0 & 1 \end{bmatrix}, T_{B''_r B'_r} = \begin{bmatrix} 1 & 0 & 0 \\ 0 & 0 & 1 \\ 0 & -1 & 0 \end{bmatrix}, T_{B'''_r B''_r} = \begin{bmatrix} 1 & 0 & 0 \\ 0 & c\beta_3 & s\beta_3 \\ 0 & -s\beta_3 & c\beta_3 \end{bmatrix},$$

$$T_{3-2-1} = \begin{bmatrix} c\theta_3 c\psi_3 & c\theta_3 s\psi_3 & -s\theta_3 \\ -s\phi_3 s\theta_3 c\psi_3 - c\phi_3 s\psi_3 & s\phi_3 s\theta_3 s\psi_3 + c\phi_3 c\psi_3 & s\phi_3 c\theta_3 \\ c\phi_3 s\theta_3 c\psi_3 + s\phi_3 s\psi_3 & c\phi_3 s\theta_3 s\psi_3 - s\phi_3 c\psi_3 & c\phi_3 c\theta_3 \end{bmatrix}.$$

The transformation matrix describing the whole 6 rotational sequence is:

$$T_{BR} = \begin{bmatrix} c\theta_3 s\psi_3 s\beta_3 - s\theta_3 c\beta_3 & c\theta_3 c\psi_3 & c\theta_3 s\psi_3 c\beta_3 + s\theta_3 s\beta_3 \\ (s\phi_3 s\theta_3 s\psi_3 + c\phi_3 c\psi_3) s\beta_3 + s\phi_3 c\theta_3 c\beta_3 & s\phi_3 s\theta_3 c\psi_3 - c\phi_3 s\psi_3 & (s\phi_3 s\theta_3 s\psi_3 + c\phi_3 c\psi_3) c\beta_3 - s\phi_3 c\theta_3 s\beta_3 \\ (c\phi_3 s\theta_3 s\psi_3 - s\phi_3 c\psi_3) s\beta_3 + c\phi_3 c\theta_3 c\beta_3 & c\phi_3 s\theta_3 c\psi_3 + s\phi_3 s\psi_3 & (c\phi_3 s\theta_3 s\psi_3 - s\phi_3 c\psi_3) c\beta_3 - c\phi_3 c\theta_3 s\beta_3 \end{bmatrix} \quad (A.4)$$

The angular velocity can be written as:

$${}^R\omega^B = \dot{\psi}_3 \hat{b}_{r_3}^m + \dot{\theta}_3 \hat{b}_{r_2}^{IV} + \dot{\phi}_3 \hat{b}_{r_1}^V$$

Same as above:

$$\left\{ {}^B\omega_B^R \right\}^T = \left\{ \hat{b} \right\}^T \cdot \begin{bmatrix} 0 & -s\psi_3 & c\theta_3 c\psi_3 \\ 0 & c\psi_3 & c\theta_3 s\psi_3 \\ 1 & 0 & -s\theta_3 \end{bmatrix} \cdot \begin{Bmatrix} \dot{\psi}_3 \\ \dot{\theta}_3 \\ \dot{\phi}_3 \end{Bmatrix} \quad (A.5)$$

$$\text{We set } {}^B M_B^R(\psi_3(t), \theta_3(t), \phi_3(t)) = \begin{bmatrix} 0 & -s\psi_3 & c\theta_3 c\psi_3 \\ 0 & c\psi_3 & c\theta_3 s\psi_3 \\ 1 & 0 & -s\theta_3 \end{bmatrix} \text{ and } {}^B\Omega_B^R = \begin{Bmatrix} \dot{\psi}_3 \\ \dot{\theta}_3 \\ \dot{\phi}_3 \end{Bmatrix}$$

By its definition angular acceleration is given by: ${}^N\alpha_B^R = \frac{d}{dt} {}^B\omega_B^R$. We emphasize

once more that according to our notation this is the derivative of the angular velocity of right wing with respect to the thorax, while the differentiation takes place in the inertial frame N and it is expressed in terms of the B frame. By application of the definition of differentiation we get:

$${}^N B \underline{\alpha}_B^R = \frac{d {}^B \underline{\omega}_B^R}{dt} = \{\hat{b}\}^T \left(\frac{d {}^B M_B^R}{dt} {}^B \Omega_B^R + \frac{d {}^B \Omega_B^R}{dt} {}^B M_B^R \right) + \left(\frac{d \{\hat{b}\}}{dt} \right)^T {}^B M_B^R \Omega_B^R \Rightarrow$$

$${}^N B \underline{\alpha}_B^R = \{\hat{b}\}^T \left({}^B \dot{M}_B^R \Omega_B^R + {}^B \dot{\Omega}_B^R M_B^R \right) + \left(\frac{d \{\hat{b}\}}{dt} \right)^T {}^B M_B^R \Omega_B^R + {}^N \underline{\omega}_B^B \times \{\hat{b}\}^T {}^B M_B^R \Omega_B^R$$

Equivalently, we can employ directly the transport theorem for the differentiation of angular velocity:

$${}^N B \underline{\alpha}_B^R = \frac{d {}^B \underline{\omega}_B^R}{dt} = \frac{d {}^B \underline{\omega}_B^R}{dt} + {}^N \underline{\omega}_B^B \times {}^B \underline{\omega}_B^R \Rightarrow$$

$${}^N B \underline{\alpha}_B^R = \{\hat{b}\}^T \left({}^B \dot{M}_B^R \Omega_B^R + {}^B \dot{\Omega}_B^R M_B^R \right) + {}^N \underline{\omega}_B^B \times {}^B \underline{\omega}_B^R \quad (A.6) \quad \Rightarrow$$

$$\left\{ {}^N B \underline{\alpha}_B^R \right\} = \left\{ \begin{array}{l} -s\psi_3 (\dot{\phi}_3 \dot{\psi}_3 c\theta_3 + \ddot{\theta}_3) - c\psi_3 [\dot{\theta}_3 (\dot{\phi}_3 s\theta_3 + \dot{\psi}_3) - \ddot{\phi}_3 c\theta_3] \\ c\psi_3 (\dot{\phi}_3 \dot{\psi}_3 c\theta_3 + \ddot{\theta}_3) - s\psi_3 [\dot{\theta}_3 (\dot{\phi}_3 s\theta_3 + \dot{\psi}_3) - \ddot{\phi}_3 c\theta_3] \\ -\dot{\phi}_3 \dot{\theta}_3 c\phi_3 + \ddot{\psi}_3 - \ddot{\phi}_3 s\theta_3 \end{array} \right\} \left\{ \hat{b} \right\} + {}^N \underline{\omega}_B^B \times {}^B \underline{\omega}_B^R$$

Rigid Body 4

The general motion of the right wing fixed on the body of our insect model at point L is given by the following kinematical sequence:

$$\hat{b} \xrightarrow[-\hat{b}_3]{-90^\circ} \hat{b}'_l \xrightarrow[-\hat{b}'_1]{-90^\circ} \hat{b}''_l \xrightarrow[-\hat{b}''_1]{\beta_4} \hat{b}'''_l \xrightarrow[3-2-1]{} \hat{l}$$

Angle β_4 describes the stroke plane variance with respect to the \hat{b}_1'' axis. To make sure that the two wings beat in the same stroke plane we have to impose:

$$\beta_4 = -\beta_3 \quad (A.7).$$

Symmetry in flapping is ensured by the following connection between the Euler sequence angles of the two wings:

$$\psi_4(t) = -\psi_3(t) \quad (A.8)$$

$$\theta_4(t) = \theta_3(t) \quad (A.9)$$

$$\phi_4(t) = -\phi_3(t) \quad (A.10)$$

The corresponding transformation matrices for the left wing are:

$$T_{B_1'B} = \begin{bmatrix} 0 & -1 & 0 \\ 1 & 0 & 0 \\ 0 & 0 & 1 \end{bmatrix}, T_{B_1''B_1'} = \begin{bmatrix} 1 & 0 & 0 \\ 0 & 0 & -1 \\ 0 & 1 & 0 \end{bmatrix}, T_{B_r''B_r'} = \begin{bmatrix} 1 & 0 & 0 \\ 0 & c\beta_4 & s\beta_4 \\ 0 & -s\beta_4 & c\beta_4 \end{bmatrix},$$

$$T_{3 \rightarrow 2 \rightarrow 1} = \begin{bmatrix} c\theta_4 c\psi_4 & c\theta_4 s\psi_4 & -s\theta_4 \\ -s\phi_4 s\theta_4 c\psi_4 - c\phi_4 s\psi_4 & s\phi_4 s\theta_4 s\psi_4 + c\phi_4 c\psi_4 & s\phi_4 c\theta_4 \\ c\phi_4 s\theta_4 c\psi_4 + s\phi_4 s\psi_4 & c\phi_4 s\theta_4 s\psi_4 - s\phi_4 c\psi_4 & c\phi_4 c\theta_4 \end{bmatrix}$$

The transformation matrix describing the whole 6 rotational sequence is:

$$T_{BL} = \begin{bmatrix} c\theta_4 s\psi_4 s\beta_4 - s\theta_4 c\beta_4 & -c\theta_4 c\psi_4 & -c\theta_4 s\psi_4 c\beta_4 - s\theta_4 s\beta_4 \\ (s\phi_4 s\theta_4 s\psi_4 + c\phi_4 c\psi_4)s\beta_4 + s\phi_4 c\theta_4 c\beta_4 & -s\phi_4 s\theta_4 c\psi_4 + c\phi_4 s\psi_4 & -(s\phi_4 s\theta_4 s\psi_4 + c\phi_4 c\psi_4)c\beta_4 + s\phi_4 c\theta_4 s\beta_4 \\ (c\phi_4 s\theta_4 s\psi_4 - s\phi_4 c\psi_4)s\beta_4 + c\phi_4 c\theta_4 c\beta_4 & -c\phi_4 s\theta_4 c\psi_4 - s\phi_4 s\psi_4 & -(c\phi_4 s\theta_4 s\psi_4 - s\phi_4 c\psi_4)c\beta_4 + c\phi_4 c\theta_4 s\beta_4 \end{bmatrix} \quad (A.11)$$

Angular velocity

$${}^B\omega^L = \dot{\psi}_4 \hat{b}_{l_3}^m + \dot{\theta}_4 \hat{b}_{l_2}^{IV} + \dot{\phi}_4 \hat{b}_{l_1}^V$$

Same as before:

$$\left\{ {}^R\omega_B^L \right\}^T = \left\{ \hat{b} \right\}^T \cdot \begin{bmatrix} 0 & -s\psi_4 & c\theta_4 c\psi_4 \\ 0 & c\psi_4 & c\theta_4 s\psi_4 \\ 1 & 0 & -s\theta_4 \end{bmatrix} \cdot \begin{Bmatrix} \dot{\psi}_4 \\ \dot{\theta}_4 \\ \dot{\phi}_4 \end{Bmatrix} \quad (A.12)$$

$$\text{We set } {}^B M_B^L(\psi_4(t), \theta_4(t), \phi_4(t)) = \begin{bmatrix} 0 & -s\psi_4 & c\theta_4 c\psi_4 \\ 0 & c\psi_4 & c\theta_4 s\psi_4 \\ 1 & 0 & -s\theta_4 \end{bmatrix} \text{ and } {}^B \Omega_B^L = \begin{Bmatrix} \dot{\psi}_4 \\ \dot{\theta}_4 \\ \dot{\phi}_4 \end{Bmatrix}$$

Angular acceleration

By its definition angular acceleration is given by: ${}^N \alpha_B^L = \frac{d}{dt} {}^N \omega_B^L$. We emphasize

once more that in according to our notation this is the derivative of the angular velocity of right wing with respect to the thorax, while the differentiation takes place in the inertial frame N and it is expressed in terms of the B frame. By application of the definition of differentiation we get:

$${}^N \alpha_B^L = \frac{d}{dt} {}^N \omega_B^L = \left\{ \hat{b} \right\}^T \left(\frac{d}{dt} {}^B M_B^L {}^B \Omega_B^L + \frac{d}{dt} {}^B \Omega_B^L {}^B M_B^L \right) + \left(\frac{d}{dt} \left\{ \hat{b} \right\} \right)^T {}^B M_B^L {}^B \Omega_B^L \Rightarrow$$

$${}^N \alpha_B^L = \left\{ \hat{b} \right\}^T \left({}^B \dot{M}_B^L {}^B \Omega_B^L + {}^B \dot{\Omega}_B^L {}^B M_B^L \right) + \left(\frac{d}{dt} \left\{ \hat{b} \right\} \right)^T + {}^N \omega_B^B \times \left\{ \hat{b} \right\} \right)^T {}^B M_B^L {}^B \Omega_B^L$$

Again, calculating alternatively the derivative of the angular velocity:

$${}^N B \underline{\alpha}_B^L = \frac{d^N {}^B \underline{\omega}_B^L}{dt} = \frac{d^B {}^B \underline{\omega}_B^L}{dt} + {}^N \underline{\omega}_B^B \times {}^B \underline{\omega}_B^L \Rightarrow$$

$${}^N B \underline{\alpha}_B^L = \left\{ \hat{b} \right\}^T ({}^B \dot{M}_B^L \Omega_B^L + {}^B \dot{\Omega}_B^L M_B^L) + {}^N \underline{\omega}_B^L \times {}^B \underline{\omega}_B^L \quad (A.13) \quad \Rightarrow$$

$$\left\{ {}^N B \underline{\alpha}_B^L \right\} = \left\{ \begin{array}{l} -s\psi_4 (\dot{\phi}_4 \dot{\psi}_4 c\theta_4 + \ddot{\theta}_4) - c\psi_4 [\dot{\theta}_4 (\dot{\phi}_4 s\theta_4 + \dot{\psi}_4) - \ddot{\phi}_4 c\theta_4] \\ c\psi_4 (\dot{\phi}_4 \dot{\psi}_4 c\theta_4 + \ddot{\theta}_4) - s\psi_4 [\dot{\theta}_4 (\dot{\phi}_4 s\theta_4 + \dot{\psi}_4) - \ddot{\phi}_4 c\theta_4] \\ -\dot{\phi}_4 \dot{\theta}_4 c\phi_4 + \ddot{\psi}_4 - \ddot{\phi}_4 s\theta_4 \end{array} \right\} \left\{ \hat{b} \right\} + {}^N \underline{\omega}_B^B \times {}^B \underline{\omega}_B^L$$

With the angular velocities and accelerations in our possession, we can move further on to calculate the indispensable for the computing of forces on our model linear velocities and accelerations of each body, starting from the description of the position vector of a random point P on each body with respect to the stated each time frame and corresponding coordinate system, expressed in the inertial frame N. According to our notation for example, $r_{\underline{N}}^{P/B}$ declares a point P on body RB1 with respect to the origin of frame B expressed in the coordinates of the N frame. Applying the proper transformations we get the following expressions for the position vectors on RB1, RB3 and RB4 respectively:

$$r_{\underline{N}}^{P/N} = r_{\underline{N}}^{B/N} + r_{\underline{N}}^{P/B} = r_{\underline{N}}^{B/N} + T_{NB} r_{\underline{B}}^{P/B}$$

$$r_{\underline{N}}^{P/N} = r_{\underline{N}}^{B/N} + r_{\underline{N}}^{R/B} + r_{\underline{N}}^{P/R} = r_{\underline{N}}^{B/N} + T_{NB} r_{\underline{B}}^{R/B} + T_{NR} r_{\underline{R}}^{P/R}$$

$$r_{\underline{N}}^{P/N} = r_{\underline{N}}^{B/N} + r_{\underline{N}}^{L/B} + r_{\underline{N}}^{P/L} = r_{\underline{N}}^{B/N} + T_{NB} r_{\underline{B}}^{L/B} + T_{NL} r_{\underline{L}}^{P/L}$$

The linear velocities emerge from differentiation in N of the above expressions, namely:

Rigid Body 1

$$\underline{v}^{P/N} = \underline{v}^{B/N} + {}^N \underline{\omega}^B \times \underline{r}^{P/B} \quad (A.14)$$

$$\underline{a}^{P/N} = \underline{a}^{B/N} + {}^N \underline{\alpha}^B \times \underline{r}^{P/B} + {}^N \underline{\omega}^B \times ({}^N \underline{\omega}^B \times \underline{r}^{P/B}) \quad (A.15)$$

Rigid Body 3

$$\underline{v}^{P/N} = \underline{v}^{B/N} + {}^N \underline{\omega}^B \times \underline{r}^{R/B} + {}^N \underline{\omega}^R \times \underline{r}^{P/R} \quad (A.16)$$

$$\underline{a}^{P/N} = \underline{a}^{B/N} + {}^N \underline{\alpha}^B \times \underline{r}^{P/B} + {}^N \underline{\omega}^B \times ({}^N \underline{\omega}^B \times \underline{r}^{R/B}) + {}^N \underline{\alpha}^R \times \underline{r}^{P/R} + {}^N \underline{\omega}^R \times ({}^N \underline{\omega}^R \times \underline{r}^{P/R}) \quad (A.17)$$

Rigid Body 4

$$\underline{v}^{P/N} = \underline{v}^{B/N} + {}^N \underline{\omega}^B \times \underline{r}^{L/B} + {}^N \underline{\omega}^R \times \underline{r}^L \quad (A.18)$$

$$\underline{a}^{P/N} = \underline{a}^{B/N} + {}^N \underline{\alpha}^B \times \underline{r}^{P/B} + {}^N \underline{\omega}^B \times ({}^N \underline{\omega}^B \times \underline{r}^{R/B}) + {}^N \underline{\alpha}^L \times \underline{r}^{P/L} + {}^N \underline{\omega}^L \times ({}^N \underline{\omega}^L \times \underline{r}^{P/L}) \quad (A.19)$$

According to Dynamics' addition theorems:

$${}^N \underline{\omega}^R = {}^N \underline{\omega}^B + {}^B \underline{\omega}^R \quad (A.20),$$

$${}^N \underline{\omega}^L = {}^N \underline{\omega}^B + {}^B \underline{\omega}^L \quad (A.21),$$

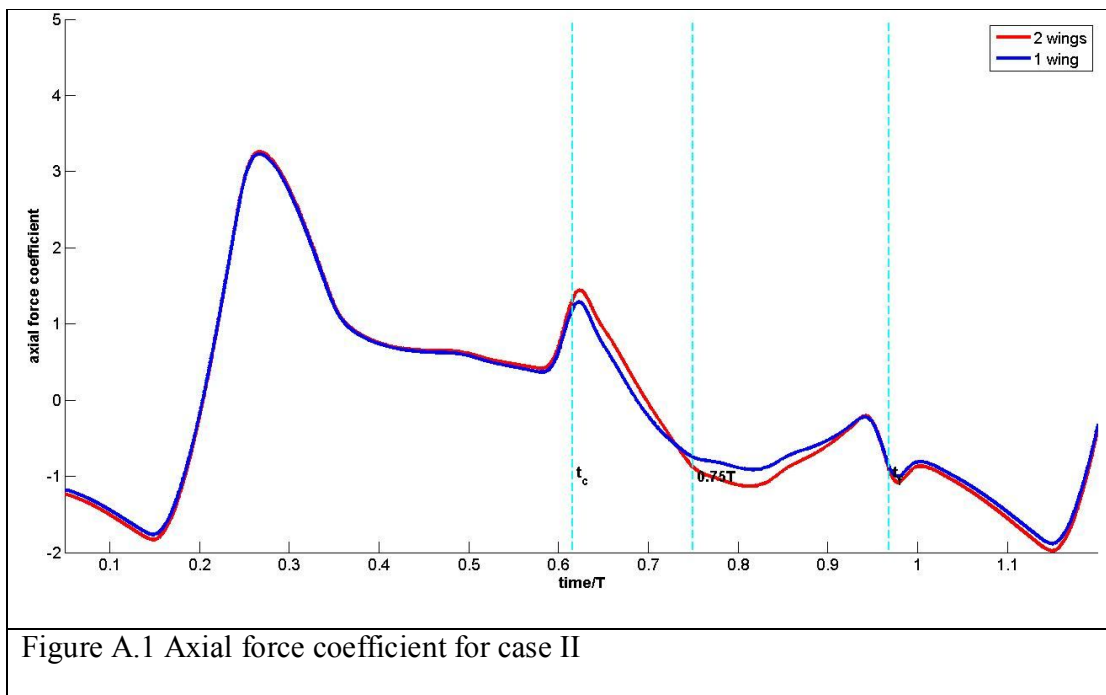
$${}^N \underline{\alpha}^R = {}^N \underline{\alpha}^B + {}^B \underline{\alpha}^R + {}^N \underline{\omega}^B \times {}^B \underline{\alpha}^R \quad (A.22),$$

$${}^N \underline{\alpha}^L = {}^N \underline{\alpha}^B + {}^B \underline{\alpha}^L + {}^N \underline{\omega}^B \times {}^B \underline{\alpha}^L \quad (A.23).$$

Appendix B

In this Appendix we give for completeness, additional figures with results for all cases and setups not presented in the main text of the thesis.

Forces



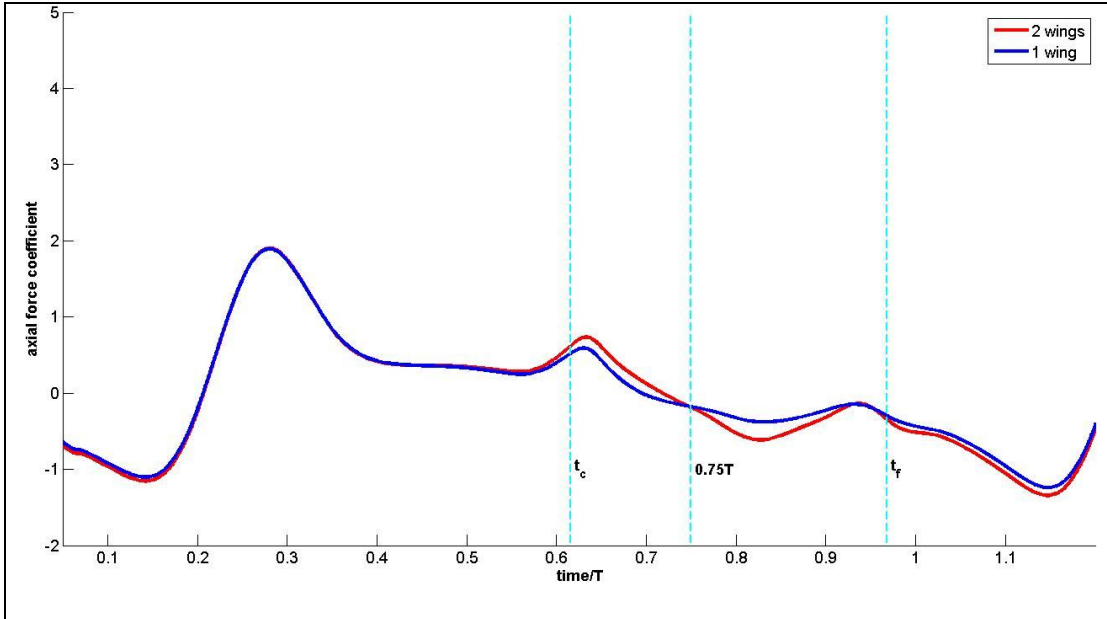


Figure A.2 Axial coefficient for case III

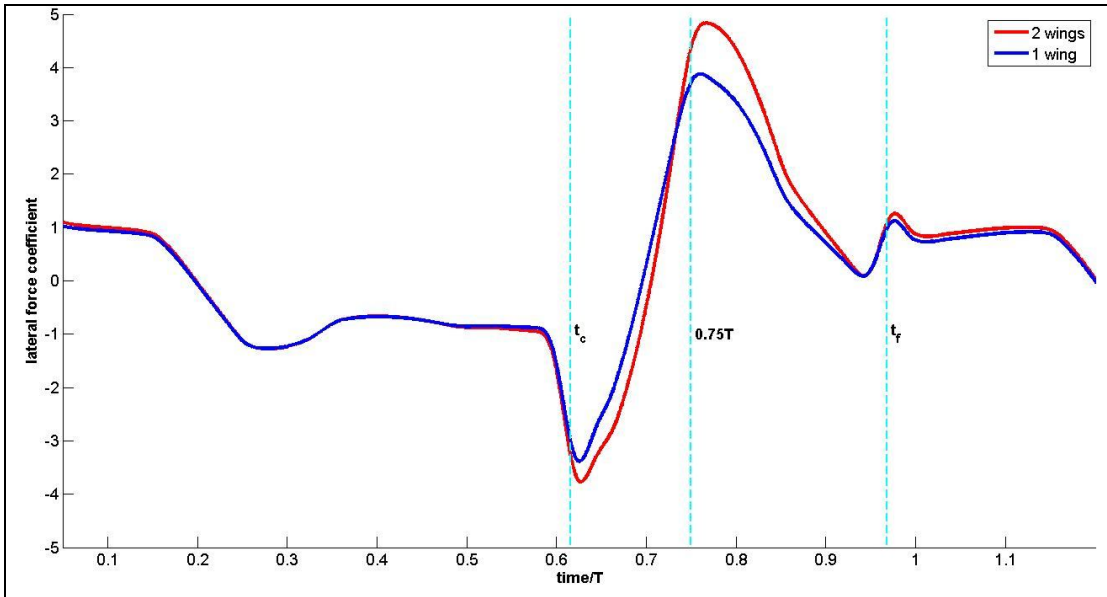


Figure A.3 Lateral force coefficient case II

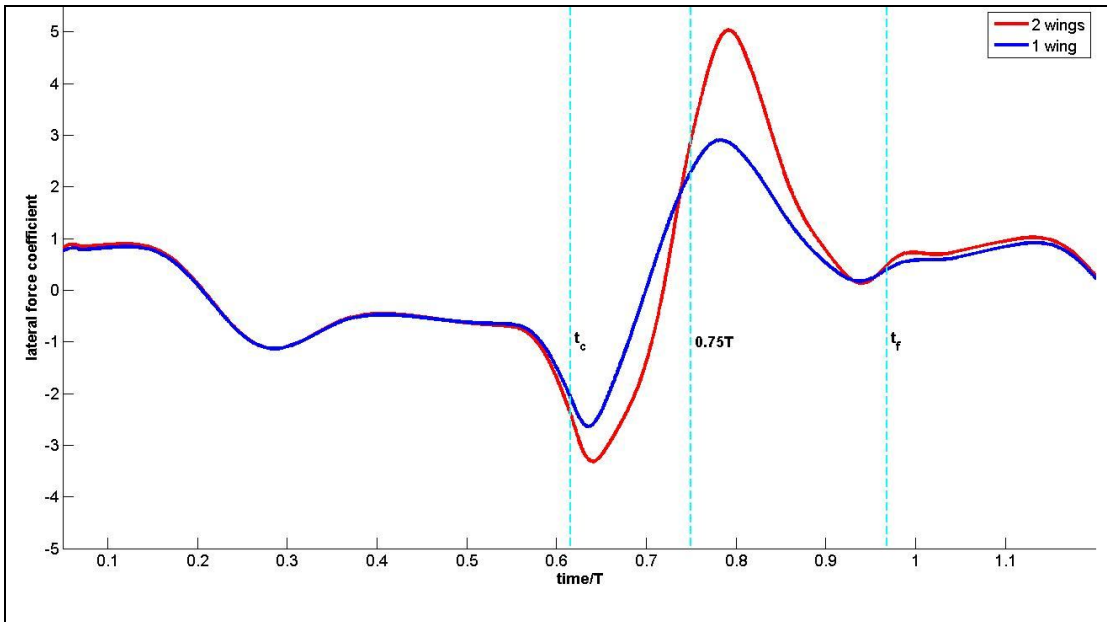


Figure A.4. Lateral force coefficient for case III

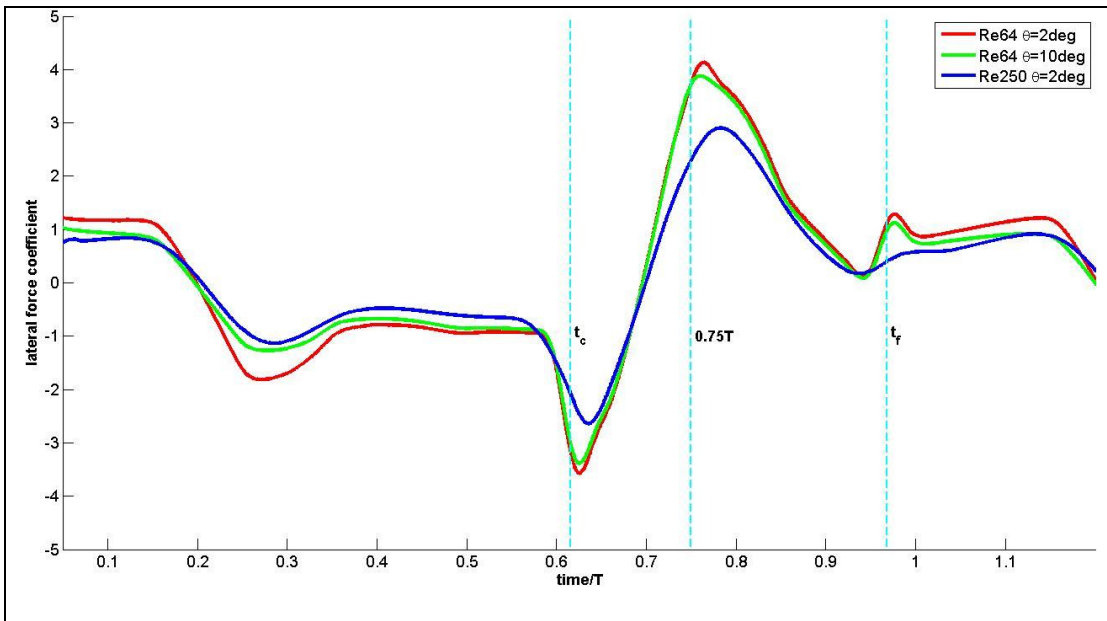


Figure A.5. Lateral force coefficient with Reynolds number and separation angle as parameters for setup II.

Flow field

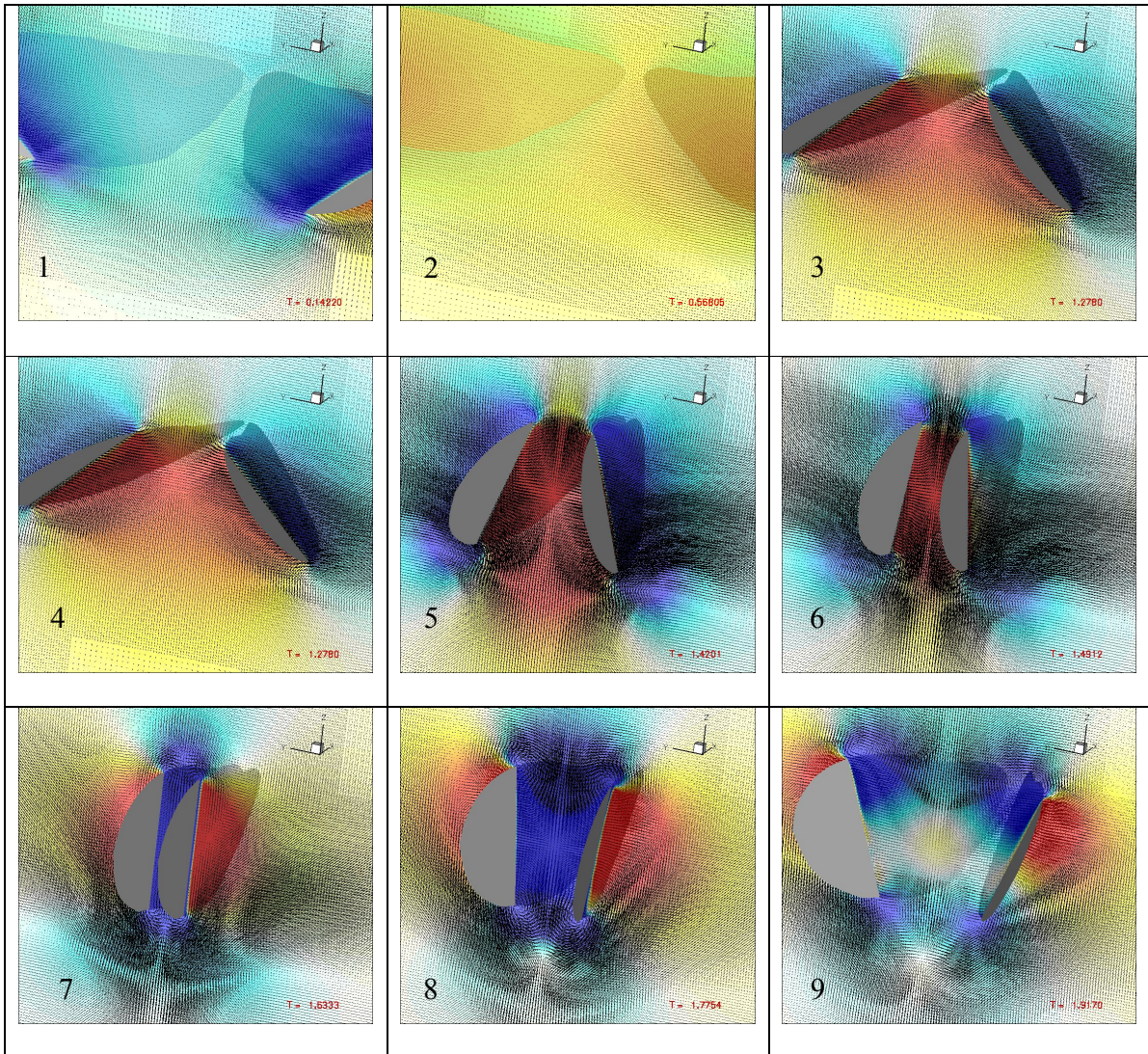


Figure A.6. Pressure contours for case I setup I at different instances within the first period for a slice vertical to the stroke plane at 65% of wing's length. Blue to red for lower to higher values from 0.5 to 0.5 and 61 contour levels. Three dimensional velocity vectors are also plotted. The 9 instances shown correspond from left to right in each row to: 1. right after the start of the motion. 2. $0.25T$ 3. right before the start of clap 4-5 within clap 6-9 within fling. On each graph on the lower right the instant at which the frame corresponds is indicated. $T=2.1384$

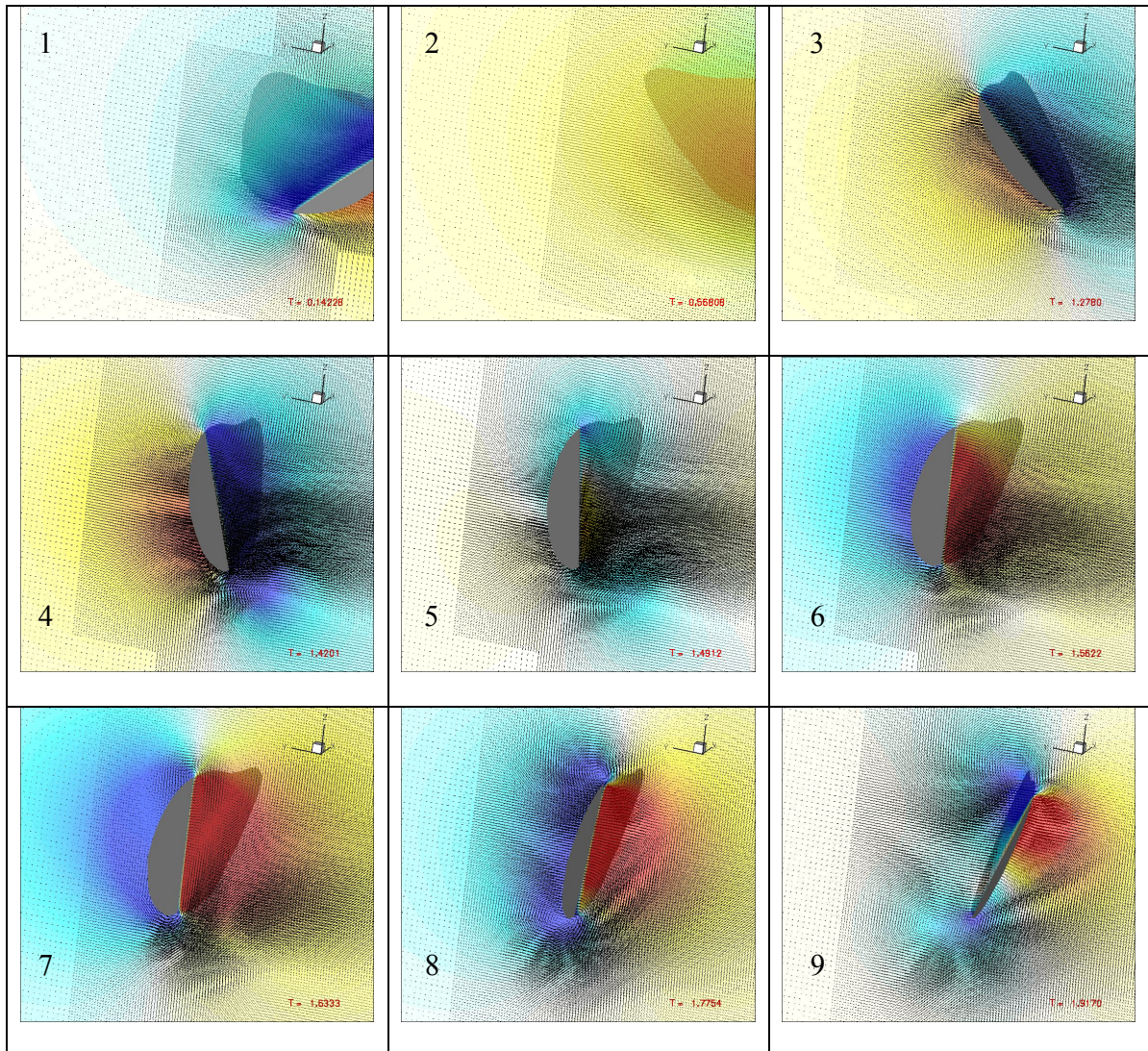


Figure A.7. Pressure contours for case I setup II at different instances within the first period for a slice vertical to the stroke plane at 65% of wing's length. Blue to red for lower to higher values from 0.5 to 0.5 and 61 contour levels. Three dimensional velocity vectors are also plotted. The 9 instances shown correspond from left to right in each row to: 1. right after the start of the motion. 2. $0.25T$ 3. Right before the start of clap 4-5 within clap 6-9 within fling. On each graph on the lower right the instant at which the frame corresponds is indicated. $T=2.1384$

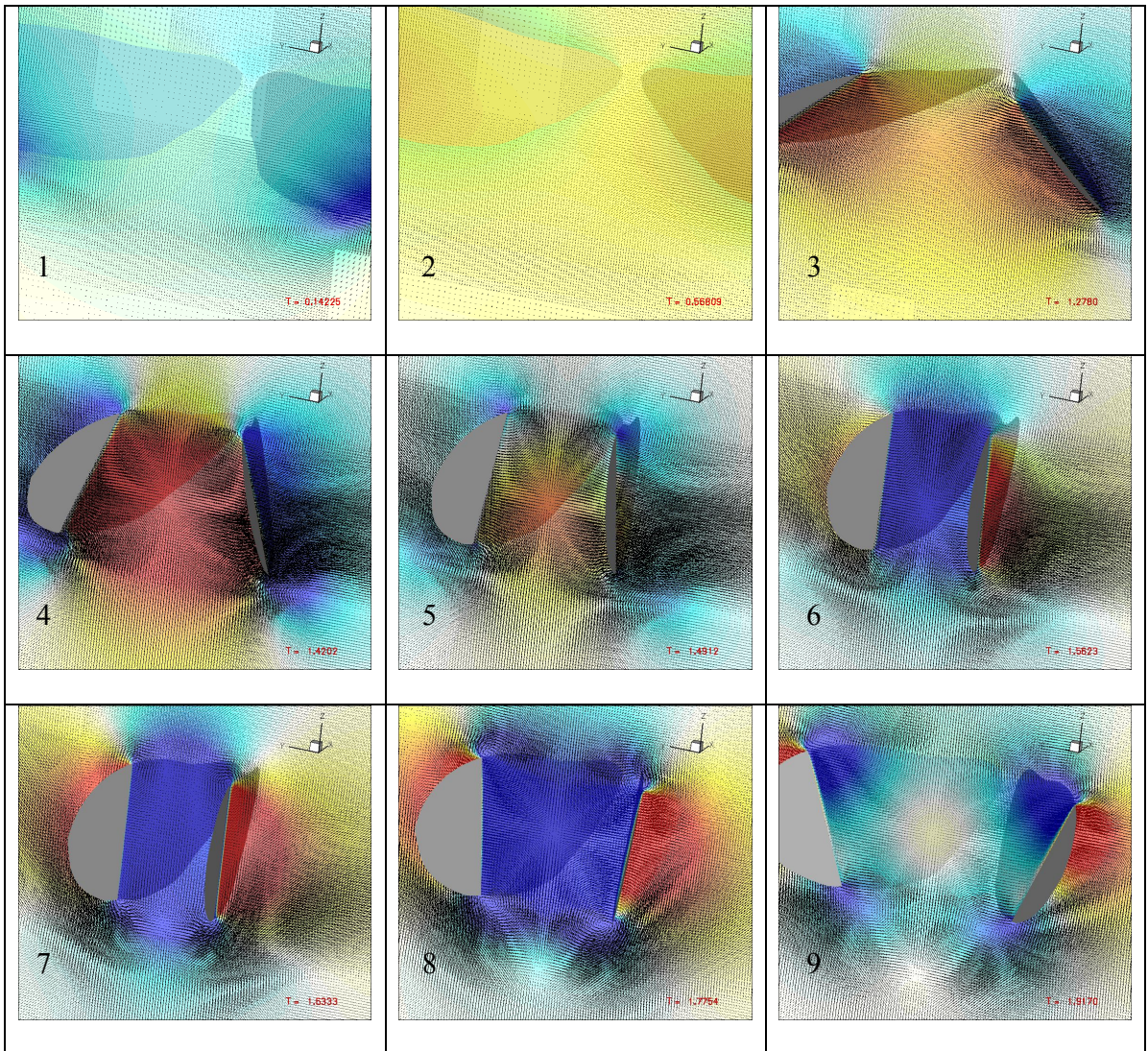


Figure A.8. Pressure contours for case II setup I at different instances within the first period for a slice vertical to the stroke plane at 65% of wing's length. Blue to red for lower to higher values from -0.5 to 0.5 and 61 contour levels. Three dimensional velocity vectors are also plotted. The 9 instances shown correspond from left to right in each row to: 1. right after the start of the motion. 2. $0.25T$ 3. right before the start of clap 4-5 within clap 6-9 within fling. On each graph on the lower right the instant at which the frame corresponds is indicated. $T=2.1384$

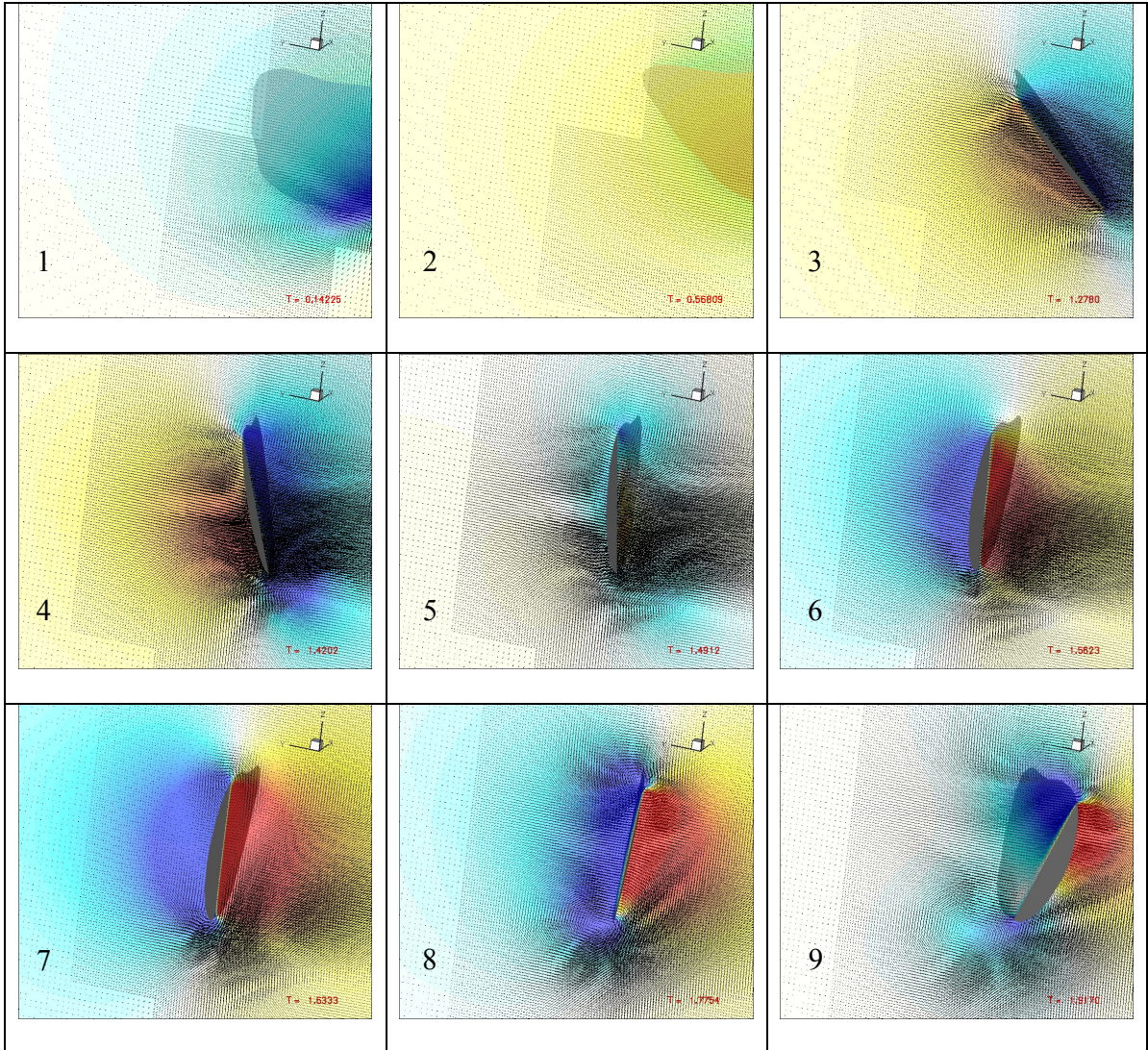


Figure A.9. Pressure contours for case II setup II at different instances within the first period for a slice vertical to the stroke plane at 65% of wing's length. Blue to red for lower to higher values from -0.5 to 0.5 and 61 contour levels. Three dimensional velocity vectors are also plotted. The 9 instances shown correspond from left to right in each row to: 1. right after the start of the motion. 2. $0.25T$ 3. right before the start of clap 4-5 within clap 6-9 within fling. On each graph on the lower right the instant at which the frame corresponds is indicated. $T=2.1384$

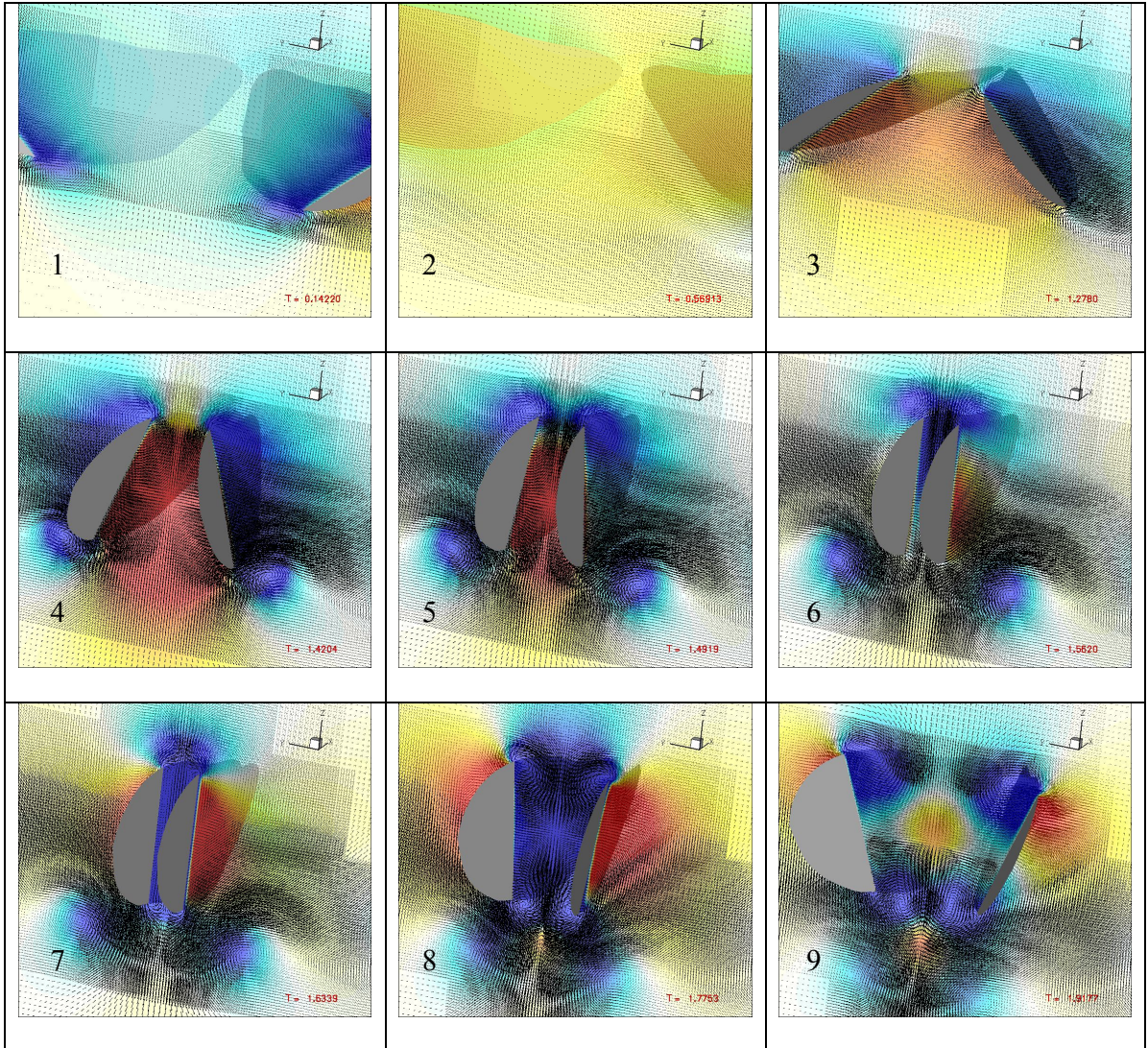


Figure A.10. Pressure contours for case III setup I at different instances within the first period for a slice vertical to the stroke plane at 65% of wing's length. Blue to red for lower to higher values from 0.5 to 0.5 and 61 contour levels. Three dimensional velocity vectors are also plotted. The 9 instances shown correspond from left to right in each row to: 1. right after the start of the motion. 2. $0.25T$ 3. right before the start of clap 4-5 within clap 6-9 within fling. On each graph on the lower right the instant at which the frame corresponds is indicated. $T=2.1384$

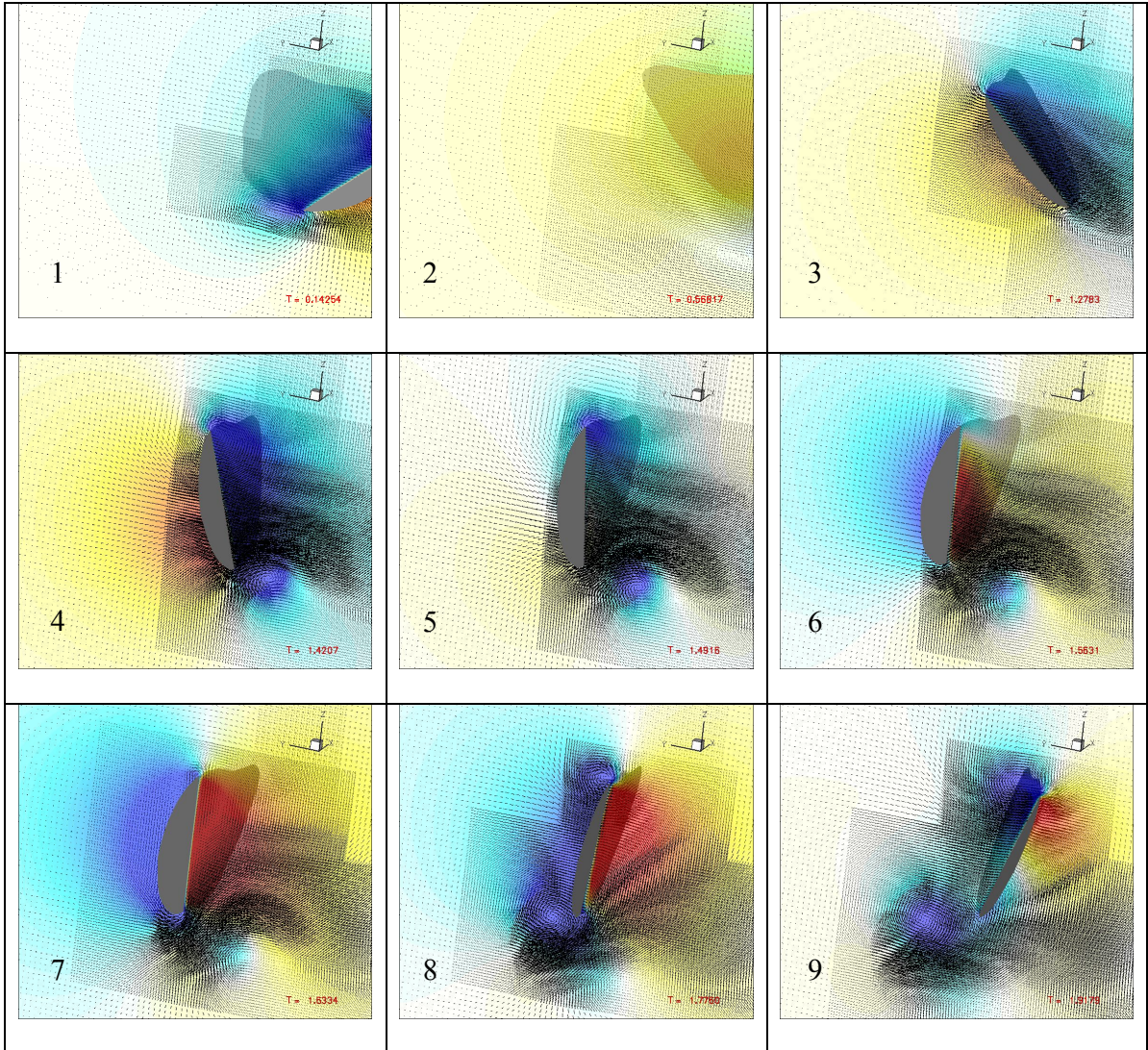


Figure A.11. Pressure contours for case III setup II at different instances within the first period for a slice vertical to the stroke plane at 65% of wing's length. Blue to red for lower to higher values from 0.5 to 0.5 and 61 contour levels. Three dimensional velocity vectors are also plotted. The 9 instances shown correspond from left to right in each row to: 1. right after the start of the motion. 2. $0.25T$ 3. right before the start of clap 4-5 within clap 6-9 within fling. On each graph on the lower right the instant at which the frame corresponds is indicated. $T=2.1384$

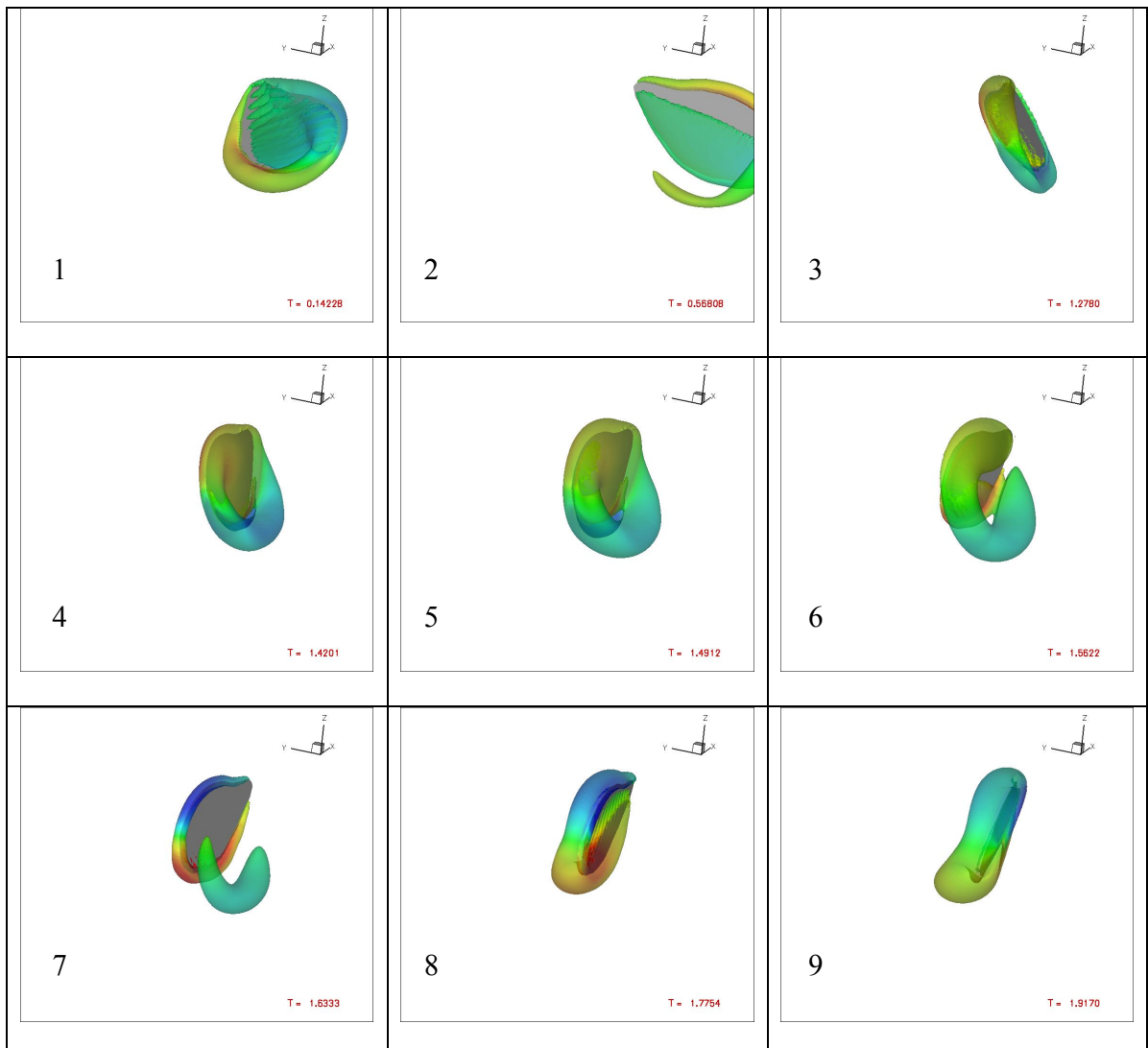


Figure A.13. $Q=5$ iso-surface colored by vorticity in x for case I setup II at different instances within the first period. Blue to red for lower to higher values from 12 to 12 and 55 contour levels. The 9 instances shown correspond from left to right in each row to: 1. right after the start of the motion. 2. $0.25T$ 3. right before the start of clap 4-5 within clap 6-9 within fling. On each graph on the lower right the instant at which the frame corresponds is indicated. $T=2.1384$

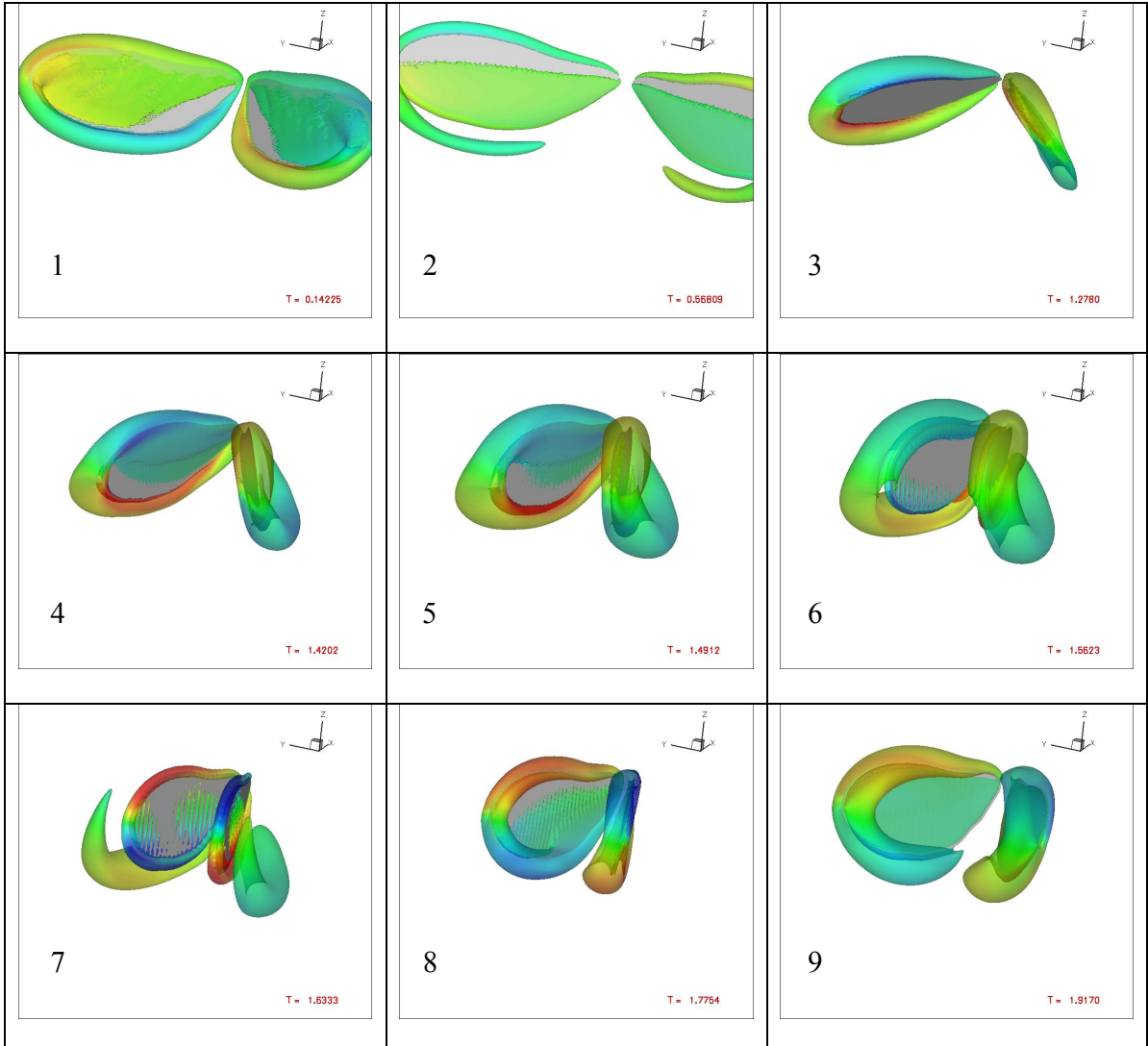


Figure A.14. $Q=5$ iso-surface colored by vorticity in x for case II setup I at different instances within the first period. Blue to red for lower to higher values from 12 to 12 and 55 contour levels. The 9 instances shown correspond from left to right in each row to: 1. right after the start of the motion. 2. $0.25T$ 3. right before the start of clap 4-5 within clap 6-9 within fling. On each graph on the lower right the instant at which the frame corresponds is indicated. $T=2.1384$

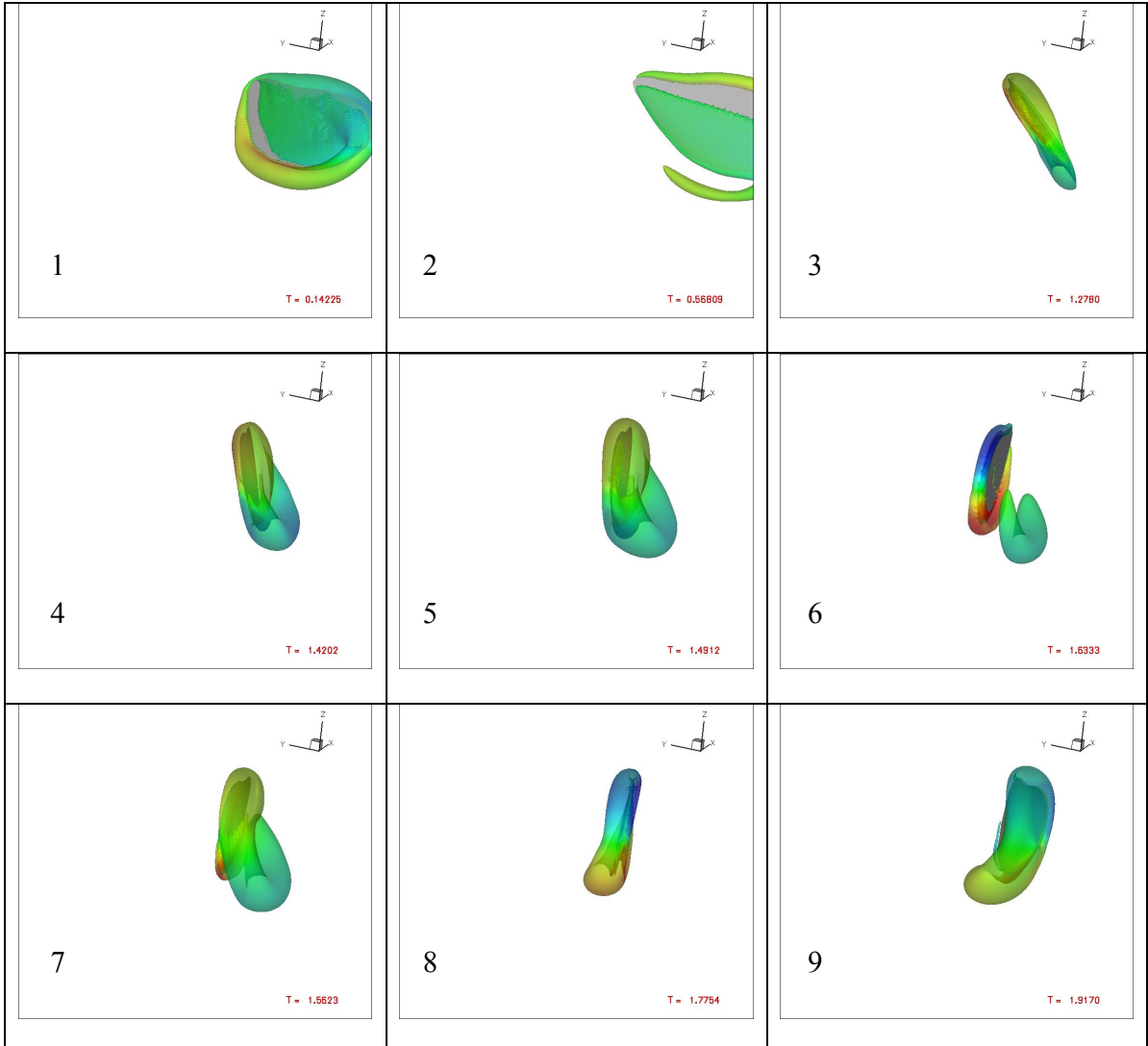


Figure A.15. $Q=5$ isosurface colored by vorticity in x for case II setup II at different instances within the first period. Blue to red for lower to higher values from 12 to 12 and 55 contour levels. The 9 instances shown correspond from left to right in each row to: 1. right after the start of the motion. 2. $0.25T$ 3. right before the start of clap 4-5 within clap 6-9 within fling. On each graph on the lower right the instant at which the frame corresponds is indicated. $T=2.1384$

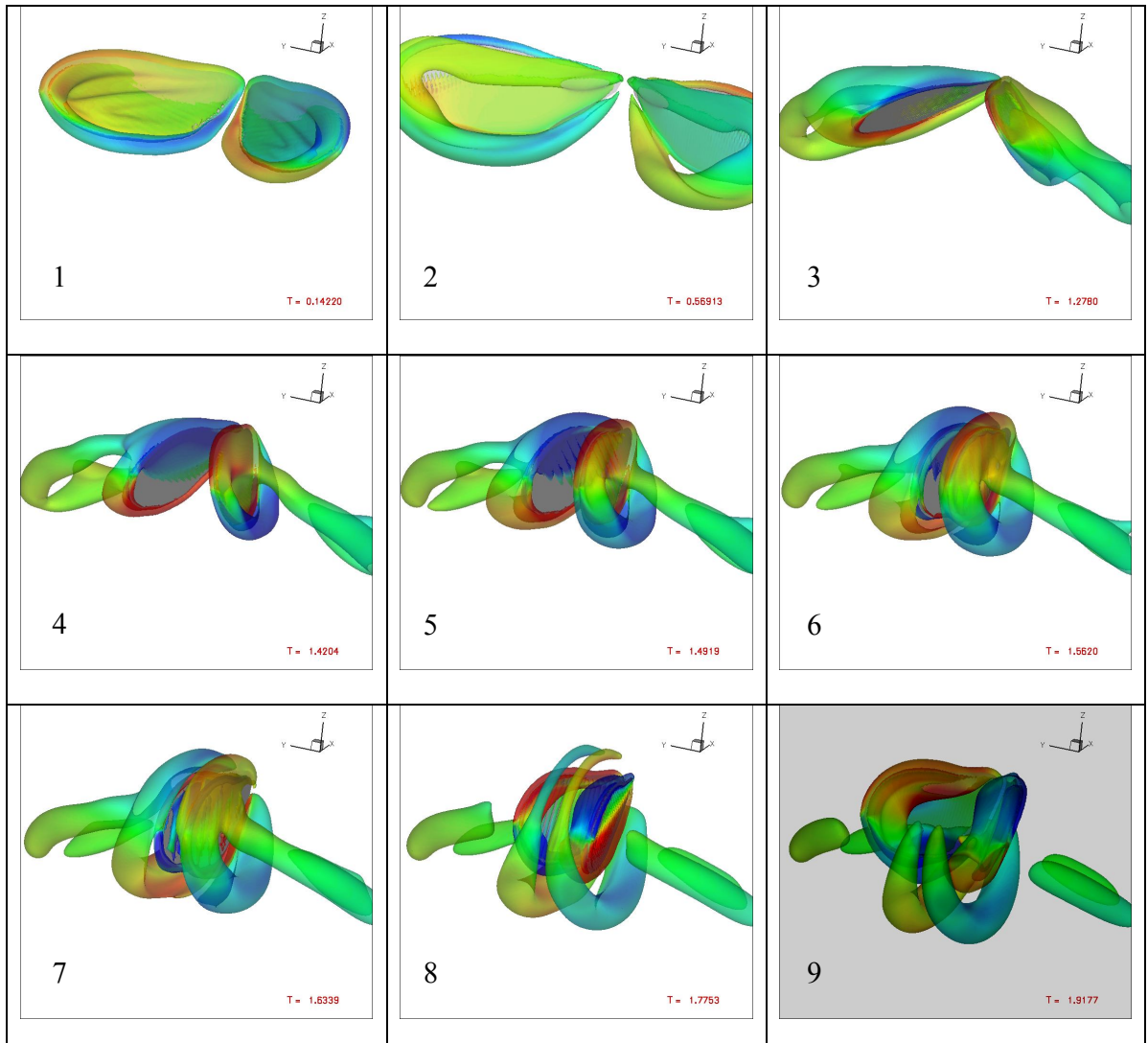


Figure A.16. $Q=5$ iso-surface colored by vorticity in x for case III setup I at different instances within the first period. Blue to red for lower to higher values from 12 to 12 and 55 contour levels. The 9 instances shown correspond from left to right in each row to: 1. right after the start of the motion. 2. $0.25T$ 3. right before the start of clap 4-5 within clap 6-9 within fling. On each graph on the lower right the instant at which the frame corresponds is indicated. $T=2.1384$

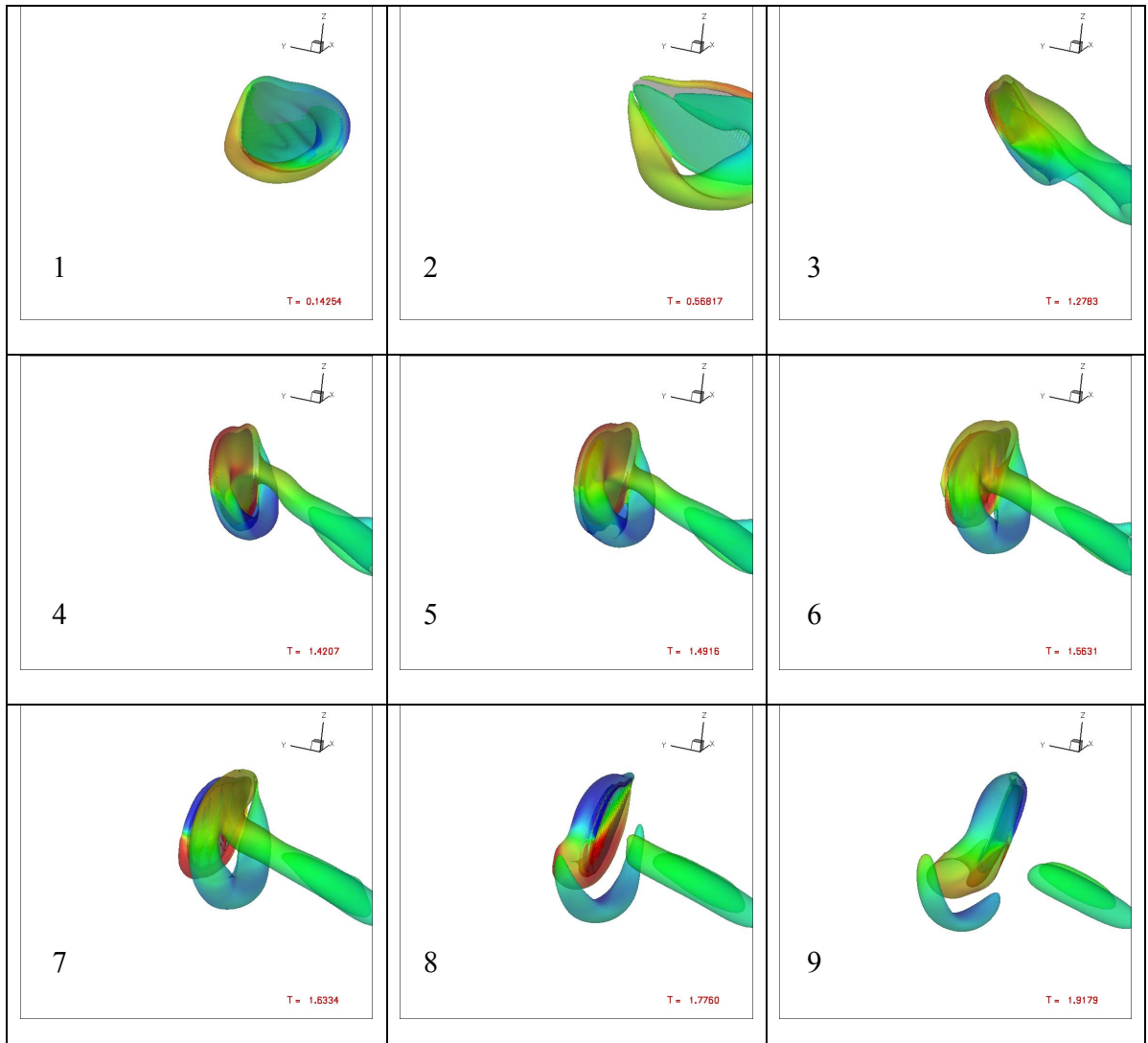


Figure A.17. $Q=5$ iso-surface colored by vorticity in x for case III setup II at different instances within the first period. Blue to red for lower to higher values from 12 to 12 and 55 contour levels. The 9 instances shown correspond from left to right in each row to: 1. right after the start of the motion. 2. $0.25T$ 3. right before the start of clap 4-5 within clap 6-9 within fling. On each graph on the lower right the instant at which the frame corresponds is indicated. $T=2.1384$

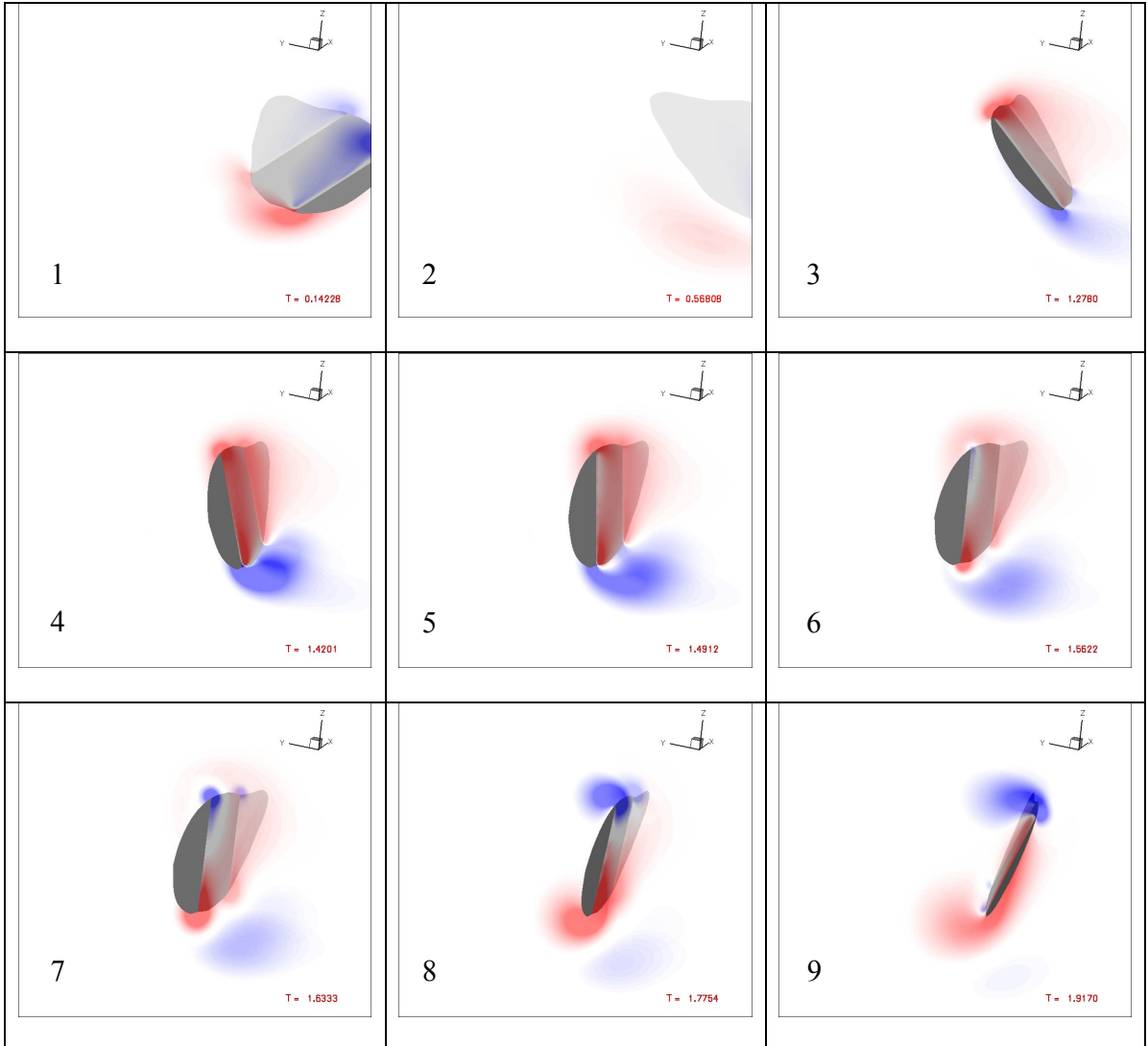


Figure A.18. ω_x contours for case I setup II at different instances within the first period for two vertical to the stroke plane slices at 30% and 65% of wing's length. Blue to red for lower to higher values from -12 to 12 and 55 contour levels. The 9 instances shown correspond from left to right in each row to: 1. right after the start of the motion. 2. $0.25T$ 3. right before the start of clap 4-5 within clap 6-9 within fling. On each graph on the lower right the instant at which the frame corresponds is indicated. $T=2.1384$

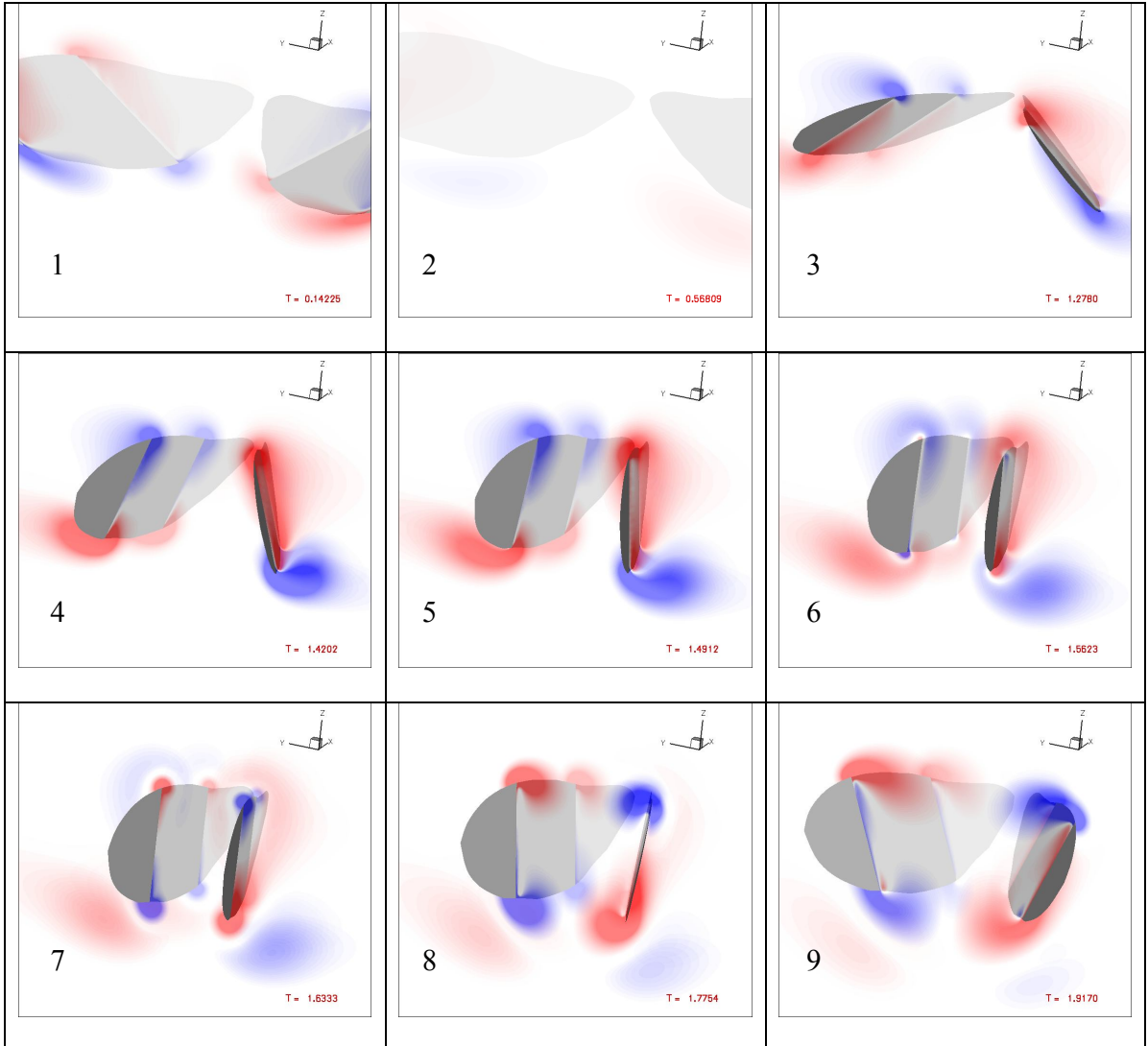


Figure A.19. ω_x contours for case II setup I at different instances within the first period for two vertical to the stroke plane slices at 30% and 65% of wing's length. Blue to red for lower to higher values from -12 to 12 and 55 contour levels. The 9 instances shown correspond from left to right in each row to: 1. right after the start of the motion. 2. $0.25T$ 3. right before the start of clap 4-5 within clap 6-9 within fling. On each graph on the lower right the instant at which the frame corresponds is indicated. $T=2.1384$

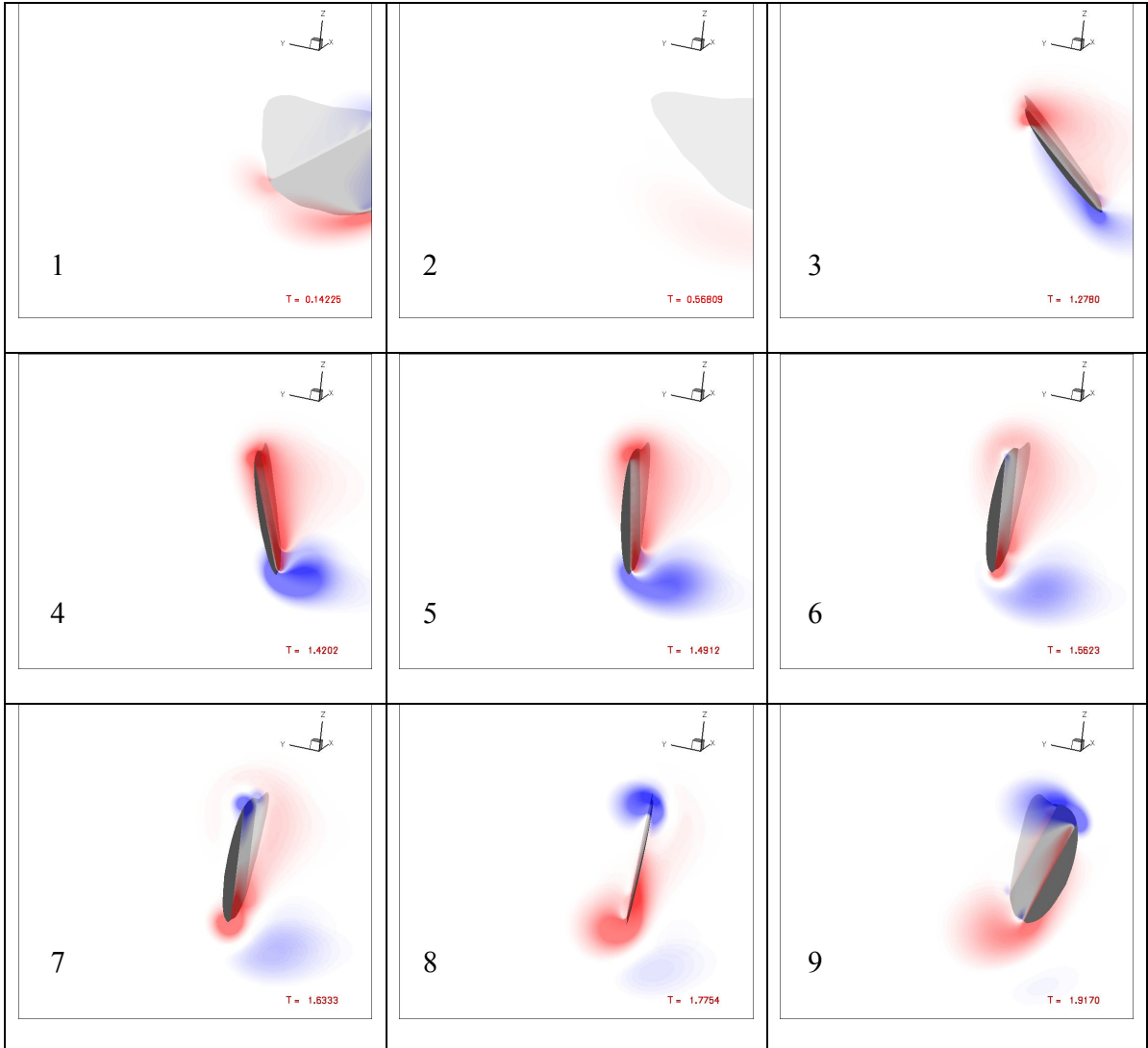


Figure A.20. ω_x contours for case II setup Ii at different instances within the first period for two vertical to the stroke plane slices at 30% and 65% of wing's length. Blue to red for lower to higher values from -12 to 12 and 55 contour levels. The 9 instances shown correspond from left to right in each row to: 1. right after the start of the motion. 2. $0.25T$ 3. right before the start of clap 4-5 within clap 6-9 within fling. On each graph on the lower right the instant at which the frame corresponds is indicated. $T=2.1384$

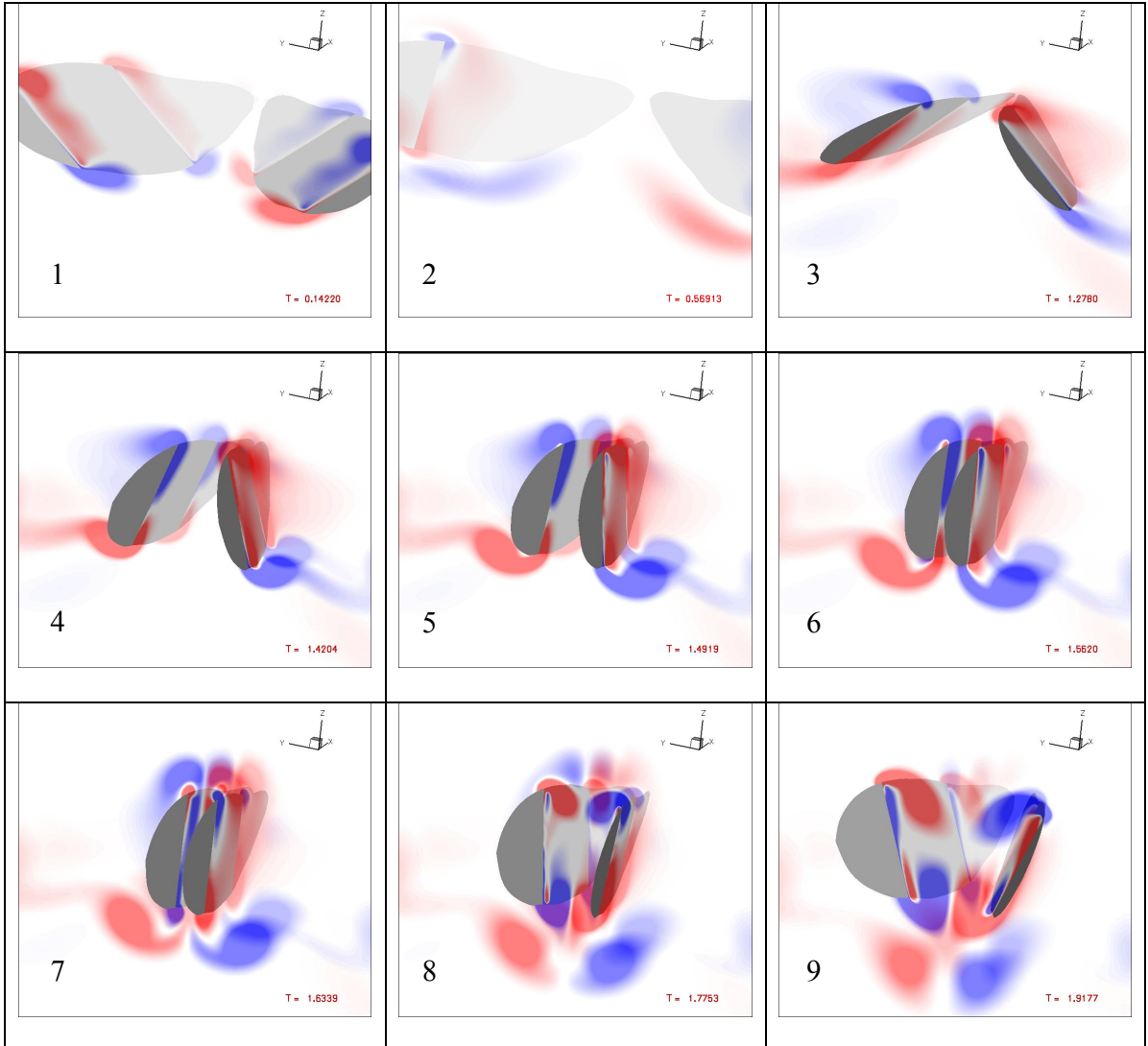


Figure A.21. ω_x contours for case III setup I at different instances within the first period for two vertical to the stroke plane slices at 30% and 65% of wing's length. Blue to red for lower to higher values from -12 to 12 and 55 contour levels. The 9 instances shown correspond from left to right in each row to: 1. right after the start of the motion. 2. $0.25T$ 3. right before the start of clap 4-5 within clap 6-9 within fling. On each graph on the lower right the instant at which the frame corresponds is indicated. $T=2.1384$

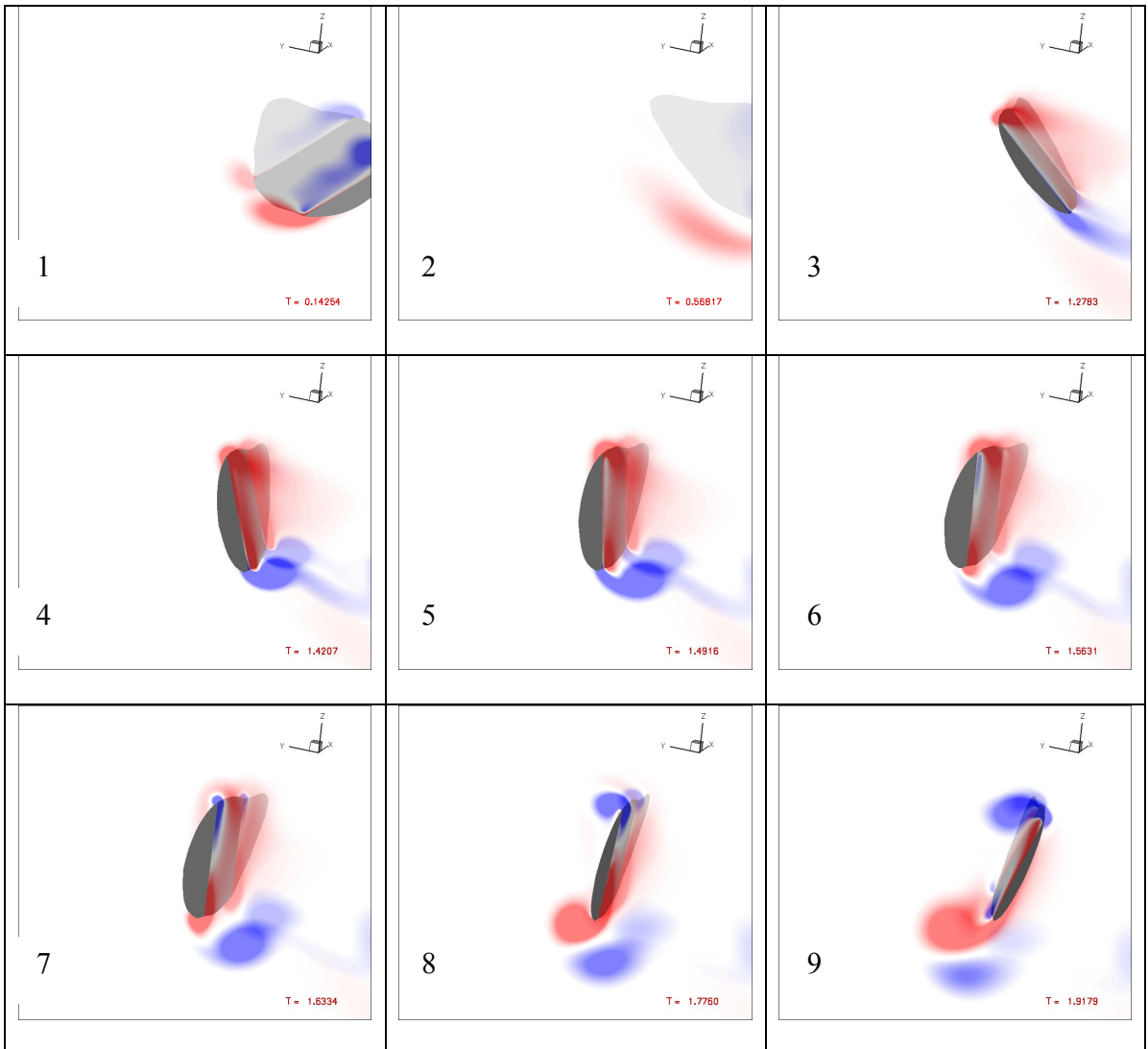


Figure A.22. ω_x contours for case III setup II at different instances within the first period for two vertical to the stroke plane slices at 30% and 65% of wing's length. Blue to red for lower to higher values from -12 to 12 and 55 contour levels. The 9 instances shown correspond from left to right in each row to: 1. right after the start of the motion. 2. 0.25T 3. right before the start of clap 4-5 within clap 6-9 within fling. On each graph on the lower right the instant at which the frame corresponds is indicated. T=2.1384

Bibliography

- [1] ANDERSON, J. D. Fundamental of Aerodynamics. McGraw-Hill Inc., Fourth Edition (2005).
- [2] BALARAS, E. Modeling complex boundaries using an external force field on fixed Cartesian grids in large-eddy simulations. *Computers & Fluids* 33 (2004), 375–404.
- [3] BARUH, H. Analytical Dynamics, McGraw-Hill Inc. (1999).
- [4] BATCHELOR, G.K. An introduction to fluid dynamics. Cambridge University Press, (2000)
- [5] BENNETT, L. Clap and fling aerodynamics – an experimental evaluation. *Journal of Experimental Biology* 69 (1977), 261-272.
- [6] BIRCH, J. M. AND DICKINSON, M. H. The influence of wing–wake interactions on the production of aerodynamic forces in flapping flight. *Journal of Experimental Biology* 206 (2003), 2257-2272.
- [7] BRACKENBURY, J. Wing movements in the bush cricket *Tettigonia viridissima* and the mantis *Ameles spallanziana* during natural leaping. *J. Zool. Lond.* 220 (1990), 593-602.
- [8] BRACKENBURY, J. Kinematics of take-off and climbing flight in butterflies. *J. Zool. Lond.* 224 (1991a), 251-270.
- [9] BRACKENBURY, J. Wing kinematics during natural leaping in the mantids *Mantis religiosa* and *Iris oratoria*. *J. Zool. Lond.* 223 (1991b), 341-356.
- [10] BRODSKY, A. K. Vortex formation in the tethered flight of the peacock butterfly *Inachis io* L. (Lepidoptera, Nymphalidae) and some aspects of insect flight evolution. *Journal of Experimental Biology* 161 (1991), 77-95.
- [11] CHAI, P., AND DUDLEY, R. Limits to vertebrate locomotor energetics suggested by hummingbirds hovering in heliox. *Nature*(1995), 377:722-725
- [12] COOTER, R. J. AND BAKER, P. S. Weis-Fogh clap and fling mechanism in *Locusta*. *Nature* 269 (1977), 53-54.
- [13] DALTON, S. Borne On The Wind. New York: Reader’s Digest Press (1975).

- [14] DICKINSON, M. H. The effects of wing rotation on unsteady aerodynamic performance at low Reynolds numbers. *Journal of Experimental Biology* 192 (1994), 179-206.
- [15] DICKINSON, M. H. AND GOTZ, K. G. Unsteady aerodynamic performance of model wings at low Reynolds numbers. *Journal of Experimental Biology* 174 (1993), 45-64.
- [16] DICKINSON, M. H., LEHMANN, F.-O. AND GOTZ, K. G. The active control of wing rotation by *Drosophila*. *Journal of Experimental Biology* 182 (1993), 173-189.
- [17] DICKINSON, M. H., LEHMANN, F.-O. AND SANE, S. P. Wing rotation and the aerodynamic basis of insect flight. *Science* 284 (1999), 1954-1960.
- [18] DUDLEY, R. *The biomechanics of insect flight*. Princeton University Press (2002).
- [19] EDWARDS R. H. AND CHENG, H. K. The Separation Vortex in the Weis-Fogh Circulation-Generation Mechanism. *Journal of Fluid Mechanics* 120 (1982), 463-473.
- [20] ELLINGTON, C. P. Non-steady-state aerodynamics of the flight of *Encarsia formosa*. *Symposium on Swimming and Flying. Nature* (ed. T. Y. Wu), pp. 729-762. Pasadena: California (1975).
- [21] ELLINGTON, C. P. The aerodynamics of normal hovering flight: three approaches. In *Comparative Physiology: Water, Irons and Fluid Mechanics* (1978). Ed. Schmidt-Nielsen, K., Bolis, L. And Maddrell, S. Cambridge University Press, pp. 327-345.
- [22] ELLINGTON, C. P. Vortices and hovering flight. In *Instationare Effekte an schwingended Fluegeln* (1980). Ed. Nachtigall, W. Weisbaden: Steiner, F., pp.64-101.
- [23] ELLINGTON, C. P. The novel aerodynamics of insect flight: applications to micro – air vehicles. *Journal of Experimental Biology* 202 (1999), 3439-3448.
- [24] ELLINGTON, C. P., VAN DEN BERG, C., WILLMOTT, A. P. AND THOMAS, A. L. R. Leading-edge vortices in insect flight. *Nature* 384 (1996), 626-630.
- [25] ELLINGTON, C. P. The aerodynamics of hovering insect flight. I. The quasi-steady analysis. *Phil. Trans. R. Soc. Lond. B* 305 (1984a), 1-15.

- [26] ELLINGTON, C. P. The aerodynamics of hovering insect flight. II. Morphological parameters. *Phil. Trans. R. Soc. Lond. B* 305 (1984b), 17-40.
- [27] ELLINGTON, C. P. The aerodynamics of hovering insect flight. III. Kinematics. *Phil. Trans. R. Soc. Lond. B* 305 (1984c), 41-78.
- [28] ELLINGTON, C. P. The aerodynamics of hovering insect flight. IV. Aerodynamic mechanisms. *Phil. Trans. R. Soc. Lond. B* 305 (1984d), 79-113.
- [29] ELLINGTON, C. P. The aerodynamics of hovering insect flight. V. A vortex theory. *Phil. Trans. R. Soc. Lond. B* 305 (1984e), 115-144.
- [30] ELLINGTON, C. P. The aerodynamics of hovering insect flight. VI. Lift and power requirements. *Phil. Trans. R. Soc. Lond. B* 305 (1984f), 145-181.
- [31] ENNOS, A. R. The kinematics and aerodynamics of the free flight of some Diptera. *Journal of Experimental Biology* 142 (1989b), 49-85.
- [32] FADLUN, E. A., VERZICCO, R. ORLANDI, P. AND MOHD-YUSOF, J. Combined immersed - boundary finite - difference methods for three-dimensional complex flow simulations. *Journal of Computational Physics* 61 (2000), 35-60.
- [33] FERZIGER, J. H. AND PERIC, M. *Computational Methods for Fluid Dynamics*. Springer-Verlag, Third Edition (2002).
- [34] FRY, S. N., SAYAMAN, R. AND DICKINSON, M. H. The aerodynamics of free-flight maneuvers in *Drosophila*. *Science* 300 (2003), 495-498.
- [35] GOTZ, K. Course-Control, Metabolism and Wing Interference During Ultralong Tethered Flight in *Drosophila Melanogaster*. *Journal of Experimental Biology* 128 (1987), 35-46.
- [36] KIM, J. AND MOIN, P. Application of a fractional-step method to incompressible Navier-Stokes equations. *Journal of Computational Physics*, 59 (1985), 308-323.
- [37] LAMB, H. *Hydrodynamics*. New York: Dover Publications (1945).
- [38] LEHMANN, F.-O. When wings touch wakes: understanding locomotor force control by wake-wing interference in insect wings. Review, *Journal of Experimental Biology* 211 (2008), 224-233.
- [39] LEHMANN, F.-O. Aerodynamische, kinematische und electrophysiologische Aspekte der Flugkraftherzeugung und Flugkraftsteuerung bei der Tauflye

- Drosophila melanogaster*. PhD thesis, University of Tübingen, Germany (1994).
- [40] LEHMANN, F.-O. The constraints of body size on aerodynamics and energetics in flying fruit flies: an integrative view. *Zoology* 105 (2002), 287-295.
- [41] LEHMANN, F.-O. The mechanisms of lift enhancement in insect flight. *Naturwissenschaften* 91 (2004), 101-122.
- [42] LEHMANN, F. -O. AND DICKINSON, M. H. The changes in power requirements and muscle efficiency during elevated force production in the fruit fly *Drosophila melanogaster*. *Journal of Experimental Biology* 200 (1997), 1133-1143.
- [43] LEHMANN, F.-O., SANE S. P. AND DICKINSON M. The aerodynamic effects of wing-wing interaction in flapping insect wings. *Journal of Experimental Biology* 208 (2005), 3075-3092.
- [44] LIGHTHILL, M. J. Mathematical biofluidynamics. In *Regional Conference Series in Applied Mathematics*, vol. 17. Philadelphia: Society for Industrial and Applied Mathematics (1975).
- [45] LIGHTHILL, M. J. On the Weis-Fogh Mechanism of Lift Generation. *Journal of Fluid Mechanics* 60 (1973), 1-17.
- [46] MAC NEISE, P., OLSON K. M., MOBARRY, C., DE FAINCHTEIN, R. AND PACKER, C. Paramesh: a parallel adaptive mesh refinement community toolkit. *Computer. Physics. Communications.*, 126 (2000), 330-354.
- [47] MARDEN J. H. Maximum Lift Production During Takeoff in Flying Animals. *Journal of Experimental Biology* 130 (1987), 235-258.
- [48] MAXWORTHY, T. Experiments on the Weis-Fogh Mechanism of Lift Generation by Insects in Hovering Flight, Part 1 Dynamics of the 'Fling'. *Journal of Fluid Mechanics* 93 (1979), 47-63.
- [49] MAYBURY, W. J. AND LEHMANN, F.-O. The fluid dynamics of flight control by kinematic phase lag variation between two robotic insect wings. *J. Exp. Biol.* 207 (2004), 4707-4726.
- [50] MILLER, L. A. AND PESKIN, C. S. When vortices stick: an aerodynamic transition in tiny insect flight. *Journal of Experimental Biology* 207 (2004), 3073-3088.

- [51] MILLER, L. A. AND PESKIN, C. S. A computational fluid dynamics of ‘clap and fling’ in the smallest insects. *Journal of Experimental Biology* 208 (2005), 195-212.
- [52] MILNE-THOMSON, L. M. *Theoretical Aerodynamics*. London, New York: Macmillan, St Martin’s press (1966).
- [53] NOCA, F., SHIELS, D. AND JEON, D. A comparison of methods for evaluating time-dependent fluid dynamic forces on bodies, using only velocity fields and their derivatives. *J. Fluids Struct.* 13 (1999), 551-578.
- [54] PANTON, R. L. *Incompressible Flow*. John Wiley and Sons, Second Edition (1996).
- [55] POLHAMUS, E. Predictions of vortex-lift characteristics by a leading edge suction analogy. *Journal of Aircraft* 8 (1971), 193-199.
- [56] RAMAMURTI, R. AND SANDBERG, W. C. A three-dimensional computational study of the aerodynamic mechanisms of insect flight. *Journal of Experimental Biology* 205 (2002), 1507-1518.
- [57] RAMAMURTI, R. AND SANDBERG, W. C. Computational study of 3-D, flapping foil, flows. *AIAA-2001*, 605 (2001).
- [58] SANE, S. The aerodynamics of insect flight. *Journal of Experimental Biology* 206 (2003), 4191-4208.
- [59] SANE, S. P. AND DICKINSON, M. H. The control of flight force by a flapping wing: lift and drag production. *Journal of Experimental Biology* 204 (2001), 2607-2626.
- [60] SANE, S. P. AND DICKINSON, M. H. The aerodynamic effects of wing rotation and a revised quasi-steady model of flapping flight. *Journal of Experimental Biology* 205 (2002), 1087-1096.
- [61] SHYY, W., LIAN, Y., TANG J. AND VIHERU D., *Aerodynamics of low Reynolds Number Flyers*, Cambridge Aerospace Series (2008)
- [62] SOHN, M. H. AND CHANG, J. W. Flow Visualization and Aerodynamic Load Calculation of Three Types of Clap-Fling in a Weis-Fogh Mechanism. *Science Direct, Aerospace Science and Technology* 11 (2007), 119-129.
- [63] SPEDDING, G. R. Comparing fluid mechanics models with experimental data. *Phil. Trans. R. Soc. Lond. B* 358 (2003), 1567-1576.

- [64] SPEDDING, G. R. AND MAXWORTHY, T. The Generation of Circulation and Lift in a Rigid Two-Dimensional Fling. *Journal of Fluid Mechanics* 165 (1986), 247-272.
- [65] SPEDDING, G. R., HEDENSTROM, A. AND ROSEN, M. W. Quantitative studies of the wakes of freely flying birds in a low-turbulence wind tunnel. *Experiments in Fluids* 34 (2003a), 291-303.
- [66] SPEDDING, G. R., ROSEN, M. W. AND HEDENSTROM, A. A family of vortex wakes generated by a thrush nightingale in free flight in a wind tunnel over its entire natural range of flight speeds. *Journal of Experimental Biology* 206 (2003b), 2313-2344.
- [67] SRYGLEY, R. B. AND THOMAS, A. L. R. Unconventional lift-generating mechanisms in free-flying butterflies. *Nature* 420 (2002), 660-6604.
- [68] SUN, M. AND YU, X. Flows around two airfoils performing fling and subsequent translation and translation and subsequent clap. *Acta Mechanica Sinica* 19, No 2 (2003), 103-117.
- [69] SUNADA, S., KAWACHI, K., WATANABE, I. AND AZUMA, A. Fundamental Analysis of Three-Dimensional ‘Near Fling’. *Journal of Experimental Biology* 183 (1993), 217-248.
- [70] UHLMANN, M. An immersed boundary method with direct forcing for the simulation of particulate flows. *Journal of Computational Physics*, Vol. 209 (2005), 448-476.
- [71] USHERWOOD, J. R. AND ELLINGTON, C. P. The aerodynamics of revolving wings – I. Model hawkmoth wings. *Journal of Experimental Biology* 205 (2002a), 1547-1564.
- [72] USHERWOOD, J. R. AND ELLINGTON, C. P. The aerodynamics of revolving wings – II. Propeller force coefficients from mayfly to quail. *Journal of Experimental Biology* 205 (2002b), 1565-1576.
- [73] VANELLA, M. A fluid structure interaction strategy applied to low Reynolds numbers flapping flight. Doctor of Philosophy Dissertation Proposal, UMCP, April 2008
- [74] VANELLA, M. AND BALARAS, E. A moving-least-squares reconstruction for embedded-boundary formulations. *Journal of Computational Physics* 228 (2009), 6617–6628.
- [75] VANELLA, M., RABENOLD P. AND BALARAS, E. An embedded boundary approach with adaptive mesh refinement for fluid-structure

interactions in viscous incompressible flows. Proceedings of Computational Methods for Coupled Problems in Science and Engineering 2007, ECCOMAS, Santa Eulalia, Ibiza, Spain.

- [76] VOGEL, S. Life in Moving Fluids. Princeton, NJ: Princeton University Press (1994).
- [77] VOGEL, S. Flight in *Drosophila*. I. Flight performance of tethered flies. Journal of Experimental Biology 44 (1966), 567-578.
- [78] WAKELING, J. M. AND ELLINGTON, C. P. Dragonfly flight. II. Velocities, accelerations, and kinematics of flapping flight. Journal of Experimental Biology 200 (1997), 557-582.
- [79] WALKER, P. B. Experiments on the growth of circulation about a wing and an apparatus for measuring fluid motion. Rep. Memo. Aeronaut. Res. (Great Britain) No 1402 (1931).
- [80] WANG, Z. J. Two dimensional mechanism for insect hovering. Phys. Rev. Lett. 85 (2000), 2216-2219.
- [81] WANG, Z., BIRCH, J., M. AND DICKINSON M.H., Unsteady forces and flows in low Reynolds number hovering flight: two-dimensional computations vs robotic wing experiments. Journal of Experimental Biology 207 (2004), 449-460.
- [82] WAGNER, H. Über die Entstehung des dynamischen Auftriebes von Tragflügeln. Z. Angew. Math. Mech. 5 (1925), 17-35.
- [83] WEIS-FOGH, T. Quick Estimates of Flight Fitness in Hovering Animals, Including Novel Mechanisms for Lift Production. Journal of Experimental Biology 59 (1973), 169-230.
- [84] WEIS-FOGH, T. Swimming and Flying in Nature, vol. 2 (ed. Y. T. Wu, C. J. Brokaw and C. Brennen), pp. 729-762. New York: Plenum Press (1974)
- [85] WHITE, F. M. Viscous Fluid Flow. McGraw-Hill Inc., Second Edition (1991)
- [86] WILLMOTT, A. AND ELLINGTON, C. P. The mechanics of flight in the hawkmoth *Manduca sexta*. 2. Aerodynamic consequences of kinematic and morphological variation. Journal of Experimental Biology 200 (1997a), 2723-2745.
- [87] WILLMOTT, A. P. AND ELLINGTON, C. P. Measuring the angle of attack of beating insect wings: robust three-dimensional reconstruction from two-

dimensional images. *Journal of Experimental Biology* 200 (1997b), 2693-2704.

- [88] WU, J. C. AND HU-CHEN, H. Unsteady aerodynamics of articulate lifting bodies. AIAA Paper no. 2184 (1984)
- [89] WU, J. Z., VAKILI, A. D. AND WU, J. M. Review of the physics of enhancing vortex lift by unsteady excitation. *Prog. Aerosp. Sci.* 28 (1991), 73-131.
- [90] YANG, J. AND BALARAS, E. An embedded-boundary formulation for large-eddy simulation of turbulent flows interacting with moving boundaries. *Journal of Computational Physics*, Vol. 215 (2006), 12-40.
- [91] ZANKER, J. M. The wing beat of *Drosophila melanogaster*. I. Kinematics. *Phil. Trans. R. Soc. Lond. B* 327 (1990), 1-18.
- [92] ZANKER, J. M. AND GOTZ, K. G. The wing beat of *Drosophila melanogaster* II. Dynamics. *Phil. Trans. R. Soc. Lond. B* 327 (1990), 19-44.
- [93] ZANKER, J. M. The wing beat of *Drosophila melanogaster*. III. Control. *Phil. Trans. R. Soc. Lond. B* 327 (1990), 45-64.